UNIVERSITÀ
DEGLI STUDI
DI PADOVA

Head Office: Università degli Studi di Padova

Department of Civil, Environmental and Architectural Engineering

Ph.D. COURSE IN:
Sciences of Civil, Environmental and Architectural Engineering
CURRICULUM:
Materials, Structures and complex systems
SERIES:
XXXVI

SEISMIC RELIABILITY AND RISK ASSESSMENT AND TARGETING OF CODE-COMPLIANT REINFORCED CONCRETE BUILDINGS

Coordinator: Prof. Massimiliano Ferronato
Supervisor: Dr. Mariano Angelo Zanini

Ph.D. student: Gianantonio Feltrin

ABSTRACT

Structural safety is one of the most challenging tasks in civil engineering, as its evaluation implies considering all the sources of uncertainty appropriate to a probabilistic context. One of the main objectives of a building code is to provide practitioners with a series of rules capable of ensuring an adequate and uniform safety margin and implicitly managing this inherent uncertainty. As a consequence, the present study focusses on assessing the seismic safety of newly designed code-compliant buildings using the well-known reliability analysis. In this way, it would be possible to assess the effectiveness of the current Italian Building Code on seismic safety in Italy. In the first part, a framework capable of carrying out seismic reliability analysis of reinforced concrete buildings will be developed. The models will be characterised by a resisting scheme composed of shear walls or frame elements, considering both bare and infilled conditions. This implies the implementation of a procedure to parametric design these prototype buildings for all the possible levels of seismic intensity, and the execution of several nonlinear dynamic analyses for assessing their vulnerability. Finally, fragilities are combined with seismic hazard curves to assess the seismic safety of all 7901 Italian municipalities. Second, a hands-on reliability-targeted approach will be proposed to overcome the *hazard-dependent* reliability outcomes of the current code-conforming design philosophy. Specifically, a new behaviour factor explicitly calibrated with a pre-defined target level of safety will be evaluated for the previous building archetypes. The last part of the work will focus on including the risk term in the assessment of code-compliant structures. Therefore, a procedure to convolute the failure rates with a loss metric will be established. Thus, this framework will be applied to the investigated archetypes. Seismic risk maps in terms of expected annual loss will be presented and compared with failure rate maps. In this way, it will be possible to evaluate how non-uniform reliability affects the risk.

TABLE OF CONTENTS

1 INTRODUCTION 1

1.1 Seismic Reliability Analysis: An Overview 2

1.2 Code-compliant seismic design approach 4

1.3 Risk-targeted design methods...5

1.4 Objectives of the study 8

1.5 Outline of the thesis 10

2 SEISMIC RELIABILITY OF CODE-CONFORMING RC BARE FRAME BUILDINGS 11

2.1 Case-study Buildings 11

2.2 Seismic design procedure 13

2.3 Seismic vulnerability assessment 19

2.4 Seismic reliability maps..33

3 SEISMIC RELIABILITY OF CODE-CONFORMING RC INFILLED FRAME BUILDINGS 44

3.1 Case-study Buildings 44

3.2 Seismic design procedure 46

3.3 Seismic vulnerability assessment 47

3.4 Seismic reliability maps..57

4 SEISMIC RELIABILITY OF CODE-CONFORMING RC SHEAR WALL BUILDINGS 64

4.1 Case-study Buildings 64

4.2 Seismic design procedure 66

4.3 Seismic vulnerability assessment 68

4.4 Seismic reliability maps 74

5 RELIABILITY-TARGETED BEHAVIOUR FACTOR 81

5.1 Methodology 81

5.2 Reliability-targeted behaviour factor for bare frames 85

5.3 Reliability-targeted behaviour factor for infilled frames 96

5.4 Reliability-targeted behaviour factor for shear walls 103

5.5 Cost-effectiveness analysis of RC frames 109

6 SEISMIC RISK OF CODE-CONFORMING RC BUILDINGS 117

6.1 Methodology 117

6.2 Seismic risk maps of bare frames 119

6.3 Seismic risk maps of infilled frames 124

6.4 Seismic risk maps of shear walls 128

7 CONCLUSIONS 134

7.1 Future studies 137

8 REFERENCES 138

LIST OF FIGURES

Figure 2-1 Planar and frontal views of the archetype frame building 13

Figure 2-2 Flowchart for the seismic design of frames 18

Figure 2-3 Nonlinear modelling of RC bare frames 19

Figure 2-4 Flowchart of the vulnerability assessment 20

Figure 2-5 Pushover curves of code-compliant bare frames - 3 storeys 22

Figure 2-6 Pushover curves of code-compliant bare frames - 6 storeys 22

Figure 2-7 Pushover curves of code-compliant bare frames - 9 storeys 23

Figure 2-8 Backbone and Hysteretic Behaviour of SDOF – Bare Frames 24

Figure 2-9 Example of the cloud of points – 6 storeys frame – ds=NC 26

Figure 2-10 Ground motions: E-W in black and N-S in blue - Part I 27

Figure 2-11 Ground motions: E-W in black and N-S in blue - Part II 28

Figure 2-12 a) Dataset of the selected events, b) Elastic spectra of the 200 ground motions 29

Figure 2-13 Correlation between the median parameter θ and the spectral acceleration S_{ae} 30

Figure 2-14 Fragility curves code-compliant bare frames - 3 storeys - NC 31

Figure 2-15 Fragility curves code-compliant bare frames - 6 storeys - NC 32

Figure 2-16 Fragility curves code-compliant bare frames – 9 storeys - NC 32

Figure 2-17 Sketch of the workflow for the code-compliant seismic reliability calculation 33

Figure 2-18 Seismic hazard maps and main soil category 34

Figure 2-19 Seismic failure rates boxplot – bare frames 35

Figure 2-20 Reliability Maps- Bare Frames - SD 38

Figure 2-21 Reliability Maps - Bare Frames - MD 39

Figure 2-22 Reliability Maps- Bare Frames - NC 39

Figure 2-23 Reliability Maps – Bare Frames - C 40

Figure 2-24 Comparison of normalized seismic hazard (on the left) and reliability maps (on the right) 41

Figure 2-25 Regression laws for failure rates estimation – Bare Frames 42

Figure 3-1 Bare and Infilled Archetypes 45

Figure 3-2 Nonlinear modelling techniques of infilled frames 49

Figure 3-3 Pushover curves of code-compliant infilled frames - 3storeys 50

Figure 3-4 Pushover curves of code-compliant infilled frames – 6 storeys 50

Figure 3-5 Pushover curves of code-compliant infilled frames – 9 storeys 51

Figure 3-6 Backbone and Hysteretic Behaviour of SDOF – Infilled Frames 53

Figure 3-7 Correlation between the median parameter θ and the spectral acceleration S_{ae} 54

Figure 3-8 Fragility curves code-compliant infilled frames – 3 storeys - NC..54
Figure 3-9 Fragility curves code-compliant infilled frames – 6 storeys - NC..55
Figure 3-10 Fragility curves code-compliant infilled frames – 9 storeys - NC......................................55
Figure 3-11 Fragility Curves NC: Bare vs Infilled...56
Figure 3-12 Seismic failure rates boxplot – Infilled frames..57
Figure 3-13 Reliability Maps - Infilled Frames – SD..60
Figure 3-14 Reliability Maps - Infilled Frames – MD 60
Figure 3-15 Reliability Maps - Infilled Frames – NC 61
Figure 3-16 Reliability Maps - Infilled Frames – C 61
Figure 3-17 Regression laws for failure rates estimation – Infilled Frames...62
Figure 4-1 Layouts of the archetype SW buildings...65
Figure 4-2 Flowchart for the seismic design of shear walls...67
Figure 4-3 Nonlinear model of Shear Wall element..70
Figure 4-4 Correlation between the median θ and the spectral acceleration S_{ae}....................................71
Figure 4-5 Fragility curves code-compliant SWs buildings – 2 storeys - NC..72
Figure 4-6 Fragility curves code-compliant SWs buildings – 4 storeys - NC..73
Figure 4-7 Fragility curves code-compliant SWs buildings – 6 storeys – NC 73
Figure 4-8 Seismic failure rates boxplot – Shear Walls..74
Figure 4-9 Reliability Maps - Shear Walls - SD..76
Figure 4-10 Reliability Maps - Shear Walls - MD 77
Figure 4-11 Reliability Maps - Shear Walls - NC 77
Figure 4-12 Reliability Maps - Shear Walls – C..78
Figure 4-13 Correlation PGA-λ_{DS} - Shear Walls 79
Figure 5-1 Framework for deriving q_{RT} factors...82
Figure 5-2 Fragility curves for reliability-targeted design 83
Figure 5-3 Histogram of reliability-targeted q_{RT} - Bare Frames...85
Figure 5-4 Italian maps of reliability-targeted factors q_{RT} – Bare Frames..87
Figure 5-5 Bar chart of q_{RT} - Bare Frames 89
Figure 5-6 Comparison of failure rates: code-compliant vs. reliability-target - Bare Frames................90
Figure 5-7 Reliability-targeted behavior factor q_{RT} curves - RC bare frames 91
Figure 5-8 Comparison of design otucomes: Code-compliant and reliability-targeted..........................96
Figure 5-9 Histogram of reliability-targeted q_{RT} - Infilled Frames...97
Figure 5-10 Italian maps of reliability-targeted factors q_{RT} – Infilled Frames 99
Figure 5-11 Bar chart of q_{RT} - Infilled Frames 100
Figure 5-12 Comparison of failure rates: code-compliant vs. reliability-target - Infilled Frames........101

Figure 5-13 Reliability-targeted behaviour factor q_{RT} curves - RC Infilled frames 102
Figure 5-14 Boxplot of q_{RT} – Shear Walls 103
Figure 5-15 Italian maps of reliability-targeted factors q_{RT} – Shear Walls 105
Figure 5-16 Bar chart of q_{RT} – Shear Walls 106
Figure 5-17 Italian Maps q_{RT} – comparison – 6-storey DCM 106
Figure 5-18 Failure rates comparison: code-compliant vs. reliability-target – Shear Walls.................107
Figure 5-19 Curves q_{RT}-B_{RT} – Shear Walls...108
Figure 5-20 Cost variation of code-conforming frames 110
Figure 5-21 Total cost maps for code-conforming frames 111
Figure 5-22 Cost-effectiveness maps for code-conforming frames...112
Figure 5-23 Reliability targeted cost curves for specific sites - frames...113
Figure 5-24 Italian cost maps for frames: code-compliant vs reliability-targeted...............................114
Figure 5-25 Reliability-targeted maps of cost for frames...116
Figure 6-1 Methodology for risk assessment 118
Figure 6-2 EAL curves - Bare frames 120
Figure 6-3 Correlation PGA-EAL – Bare Frames..121
Figure 6-4 EAL ranges - Bare Frames...122
Figure 6-5 Seismic risk maps of code-conforming Bare Frames 123
Figure 6-6 EAL ranking - Bare Frames..123
Figure 6-7 EAL curves - Infilled Frames 124
Figure 6-8 Correlation PGA-EAL – Infilled Frames..125
Figure 6-9 EAL ranges – Infilled Frames..126
Figure 6-10 Seismic risk maps of code-conforming Infilled Frames 127
Figure 6-11 EAL ranking - Infilled Frames..128
Figure 6-12 EAL curves – Shear Walls 129
Figure 6-13 Correlation PGA-EAL – Shear Walls 130
Figure 6-14 EAL ranges - Shear Walls..131
Figure 6-15 Seismic risk of code-conforming shear walls...132
Figure 6-16 EAL ranking - Shear Walls 132

LIST OF TABLES

Table 2-1 Mechanical properties of concrete C25/30 ... 12
Table 2-2 Mechanical properties of reinforcing steel B450C ... 12
Table 2-3 Summary of failure rates – Bare Frames ... 36
Table 2-4 Regression parameters – Bare Frames ... 43
Table 3-1 Mechanical properties of concrete C25/30 ... 45
Table 3-2 Mechanical properties of reinforcing steel B450C ... 46
Table 3-3 Mechanical properties of masonry infills ... 46
Table 3-4 Summary of failure rates – Infilled Frames ... 58
Table 3-5 Regression parameters – Infilled Frames ... 63
Table 4-1 Mechanical properties of concrete C30/37 ... 65
Table 4-2 Mechanical properties of reinforcing steel B450C ... 66
Table 4-3 Summary of failure rates – Shear Walls ... 75
Table 4-4 Regression parameters – Shear Walls ... 80
Table 5-1 Summary of q_{RT} - Bare Frames ... 88
Table 5-2 Municipalities for curves B_{RT}-q_{RT} ... 91
Table 5-3 Comparison of reliability-targeted behaviour factor ... 93
Table 5-4 Comparison of reliability-targeted failure rates ... 93
Table 5-5 Features of the case-study ... 95
Table 5-6 Summary of q_{RT} - Infilled Frames ... 98
Table 5-7 Summary of q_{RT} – Shear Walls ... 104
Table 5-8 Reliability-targeted cost for frames ... 115
Table 6-1 EAL values - Bare frames ... 120
Table 6-2 EAL extreme values – Bare Frames ... 121
Table 6-3 EAL values – Infilled Frames ... 124
Table 6-4 EAL extreme values – Infilled Frames ... 126
Table 6-5 EAL values – Shear Walls ... 129
Table 6-6 EAL extreme values - Shear Walls ... 131

1 INTRODUCTION

The evaluation of structural safety plays a crucial role in the design process, as failure of a system is directly related to unacceptable behaviour of the structure, which significantly endangers human lives and leads to economic losses or harming the environment. Furthermore, structural safety has to be guaranteed towards stochastic actions, such as earthquake events, and this spreads up the complexity of the problem. For this reason, the quantification of a desirable performance level has to be stated in terms of probability, to properly deal with the uncertain nature of the various parameters involved both on the system side and on applied loads. In this context, reliability analysis represents the main tool capable of assessing the probability of exceeding a pre-defined limit state in a specified reference period and considering all the different sources of uncertainty. Therefore, the probability of failure could be expressed by describing the failure event in terms of a function formulation, which is called the *limit state function g(x)*, and leads to the subsequent integral [1]:

$$P_f = P[g(x) \leq 0] = \int_{g(x)\leq 0} f_X(x)dx \tag{1.1}$$

where $f_X(x)$ represents the joint probability density function of the random variables $X=[X_1, \ldots, X_n]$, given n the number of uncertain parameters of the problem. The solution of this integral could be a nontrivial task due to demanding integration domains. As a consequence, the classical numerical methods could not efficiently compute the solution, thus different appropriate approaches have been developed in the literature. The feasibility and related computational burden of these methods strongly depend on the functional form of the *g(x)* limit state function; which is described through the comparison of two measurable quantities, the demand *D* and the capacitance *C* of the structure. The former expresses the response of the system in a specific state, whereas the second reveals the maximum demand that could hold the structure before exceeding a defined level of performance. However, this fully probabilistic approach could be difficult to perform during the ordinary design process, thus most current building codes [2] [3] address the reliability theory through the so-called *'semi-probabilistic method'*, which is based on the design format of the load and resistance factor [4]. This approach accounts for the uncertainties inherent in the nominal strength of the materials and for the variation of the load effects by employing a coefficient γ_R to decrease resistance and another one γ_R to increase the acting loads:

$$R_d = \frac{R_d}{\gamma_R} \leq S_d = \gamma_S S_k \tag{1.2}$$

These safety coefficients must be calibrated to lead the design process to satisfy the reliability requirements implicitly. For example, in many codes, the nominal value of safety factors is set to a percentile of 5% and 95% for resistance and load, respectively.

1.1 SEISMIC RELIABILITY ANALYSIS: AN OVERVIEW

The most widely used methodology for assessing seismic reliability is that developed by the *Pacific Earthquake Engineering Research Centre* (PEER) [5], which is based on the *performance-based earthquake engineering (PBEE) principle* [6]. This probabilistic method provides a performance metric in terms of the rate of exceedance of a specific decision variable (*dv*), and it allows for managing all the uncertainties involved in the seismic assessment of structures. More in detail, it could be subdivided into four principal steps: hazard analysis, structural analysis, damage analysis, and loss analysis. These stages are mathematically resumed by the subsequent triple integral:

$$\lambda(dv) = \int_{dm}\int_{edp}\int_{im} G(dv|dm)|dG(dm|edp)||dG(edp|im)||d\lambda(im)| \tag{1.3}$$

Therefore, the complete implementation of this process provides risk metrics that could be particularly interesting to stakeholders. On the other hand, by focusing on the first two steps of this methodology, it is possible to express the seismic performance of a structure in terms of the mean annual frequency of exceedance of a specific limit state λ_{LS} (MAFE), which leads to the simplified formulation:

$$\lambda_{LS} = \int_{0}^{+\infty} P[f|im] \cdot |dH(im)| \tag{1.4}$$

The term $|dH(im)|$ is the absolute derivative of the hazard curve, which is the main output of the *probabilistic seismic hazard analysis (PSHA)* [7]. Specifically, this step aims at quantifying the mean annual rate exceeding a certain level of the intensity measure *im*, commonly expressed in terms of *peak ground acceleration (PGA)* or the first mode *spectral acceleration* ($S_{ae}(T_1)$)*.* This analysis attempts to include all the uncertainties associated with the seismic hazard, for example, the inability to predict the actual position of the earthquake.

The term $P[f|im]$ expresses the probability of reaching or exceeding a certain damage threshold, conditioned on a given intensity measure *im,* and it is called the *fragility function [8].* This is the main output of the *structural analysis* stage and aims to characterise the seismic response of the structure by monitoring some useful quantities, called *engineering demand parameters (EDP).* Thus, the capture of the uncertainties proper of the seismic structural behaviour is carried out from nonlinear dynamic analysis procedures. The most popular ones are the *Cloud Analysis [9],* the *Incremental Dynamic Analysis (IDA) [10]*, and the *Multi-stripes Analysis [11].* Consequently, the seismic failure rate, referred to as a specific level of performance (i.e. *state of damage DS)* is obtained by coupling these two functions into the integral (1.4).

1.2 CODE-COMPLIANT SEISMIC DESIGN APPROACH

The framework aforementioned has been applied mainly to academic research to assess the seismic performance of existing structures rather than designing new ones. Moreover, it struggles to enter into the design process provided by the seismic codes, due to its inherent probabilistic nature, which is too computationally demanding for practitioners.

As a consequence, current codes typically follow the so-called *force-based design* approach (FBD), where building performance is evaluated through the application of a system of equivalent lateral elastic forces or by means of response spectrum analysis (RSA) [12]. Therefore, the seismic intensity is derived from a uniform hazard spectrum (UHS) with a specific T_R return period at the site of interest. For example, in the case of ordinary residential buildings, a return period of 475 years is adopted for the *life-safety limit state* and a value of 50 years for the *serviceability* one. Furthermore, the inelastic properties of the structure are addressed only implicitly by employing a force reduction factor q. In this context, a structural engineer strictly follows the qualitative and quantitative code prescriptions in order to guarantee the conforming of the sized buildings. This procedure consists of evaluating the comparison between demand and capacity in the structural component of the element, as highlighted in Equation (1.2).

However, this simplification of the performance-based engineering philosophy implies a series of drawbacks in the actual performance achieved by code-compliant structures [13]. First, there is no clear link between the safety check at the element level and the global performance of the structures. Furthermore, the design process is not capable of providing direct information on the seismic performance of the designed buildings, that is, the physical way the structural system performs against earthquake-induced actions [14].

Moreover, some studies contested the use of force-based methodology for evaluating a dynamic response, in particular for adopting a constant reduction coefficient to account for the inelastic behaviour of elements. Therefore, they proposed the adoption of a method based on the direct assessment of the displacement demand induced by seismic action [15]. Thus, the design workflow must be developed to strictly couple the compliance of requirements with the seismic performance of the structures. For this reason, in recent years, several studies have investigated the performance of code-compliant buildings in terms of collapse safety and losses [16-19]. For example, detailed research on the quantification of seismic reliability and risk classes for various code-conforming buildings has been collected in the FEMA P58-5 guideline [20]. A recent Italian research project has quantified the seismic failure rates of some code-compliant buildings for three sites characterised by increasing seismic hazard, and it pointed out that these structures did not exhibit the same level of collapse safety [21].

1.3 RISK-TARGETED DESIGN METHODS

The previous Section has highlighted how the semi-probabilistic approach currently adopted for designing new code-compliant buildings fails in ensuring a risk-consistent outcome. This issue could be explained through the simplified equation for deriving the mean annual frequency of exceedance [22], as indicated in [23]:

$$\lambda_f \approx H(im_c)e^{\frac{1}{2}k^2\beta^2} = k_0 \cdot im_c^{-k} \cdot e^{\frac{1}{2}k^2\beta^2} \tag{1.5}$$

where both the slope k of the linearized hazard function $H(im)$ and the dispersion β of the fragility for the selected damage state constitute an amplification factor of the seismic failure rate. Hence, non-uniform level of seismic reliability is produced if code prescriptions could not be capable of adequately mitigating this magnification factor. For this reason, it is necessary to change the design paradigm in order to consider MAFE as an explicit objective of the sizing procedure, rather than starting from a spectral acceleration computed only for a single hazard rate of exceedance. This could be achieved by implementing a methodology based on iterative design processes using extensive nonlinear dynamic analyses, which are performed until a pre-defined MAFE $\lambda_{c,a}$ is achieved [24, 25]. Hence, the Equation (1.4) of the PBEE framework could be expressed as follows:

$$\lambda_c = \int_0^{+\infty} P[D \geq C|im] \cdot |dH(im)| \leq \lambda_{c,a} \tag{1.6}$$

This paradigm would ensure uniform values of the failure rate throughout an entire country [26], thus some researchers developed some alternative improved design methodologies capable of explicitly managing the seismic risk of structures [27-29]. However, the excessive computational burden and the requirement of further expertise make the application of the aforementioned method by structural designers a challenging task. To address this issue, recent literature studies focused on developing alternative procedures capable of including reliability-targeted philosophy as part of current force-based design practice. For instance, Gkimprixis et al. [30] grouped these approaches into three main categories: the first one deals with the development of risk-targeted spectra (RTS) [31], the second one proposes the formulation of risk-targeted behaviour factor (RTBF) [32], and the third one is based on direct estimation of inelastic ground motion models [33].

Firstly, Luco et al. [31] proposed a procedure for redefining the design spectra switching from a uniform-hazard formulation to a uniform-risk one. In this way, he modified the seismic design maps of US building codes [34] by introducing an intensity of ground motion that yields to a constant failure rate throughout the entire American territory. These risk-targeted spectral accelerations are obtained through an iterative procedure, which consists of convolving the site's hazard curve and lognormal distributed generic fragility curves with an assumed constant dispersion (β=0.6). In detail, the initial mean of fragility is set equal to the one provided by uniform-hazard map, and the ratio between this value and the spectral acceleration ensuring a MAFE of 2% in 50 years is the so-called Risk-Coefficient (RC).

In the same way, Douglas et al. [35] applied the risk-targeted map method in Europe, specifically for the territory of France. In this case, the desirable mean annual frequency was set to $1 \cdot 10^{-5}$ in order to minimize the gap with the target value proposed by the France provisions. Consequently, the so-defined risk-targeted maps approach gathered an ever-increasing interest and other proposals have been developed for different countries [30, 36-38].

On the other hand, further researchers focused on the formulation of a proper reliability-targeted force reduction factor, which could be directly embraced in the standard code-compliant design-path of the force-based method [25, 39, 40]. In particular, starting from the precursive work of Kennedy and Short [41] and Cornell [22], Žižmond and Dolšek [32] developed two alternative formulations to derive a reliability-targeted spectral acceleration $S_{EeD,a}$. This approach directly accounts for the effective fragility of the buildings as opposed to the RTS methods.

$$r_{NC} = \left(\frac{\mu_{NC}}{C_1}\right) \cdot \left(\frac{F_Y}{F_{D,a}}\right) = r_{\mu NC} \cdot r_s \tag{1.7}$$

As highlighted in the equation, this method provides the definition of a response reduction factor r_{NC}, which considers the yielding strength F_Y, the inelastic deformation ratio C_1, the available ductility of the structure μ_{NC} and the risk-targeted design base shear $F_{D,a}$. It should be emphasized that the new generation of Eurocode 8 included the reliability-targeted approach in an informative annex [42]. The approaches aforementioned focused on setting a target mean annual frequency for collapse or near collapse damage state. However, in recent seismic events most of the buildings experienced slight structural damages and ruptures to non-structural elements, that led to considerable economic losses. For this reason, another step in the targeted design approach consists of including risk metrics (i.e. *risk-targeted design*), such as fatality risks [43, 44], by means of the so-called loss functions, which reworks the Equation (1.6):

$$\lambda_R = \int_0^{+\infty} P[LS|im] \cdot |dH(im)| \cdot P[E|LS] \leq \lambda_{R,t} \tag{1.8}$$

where $P[E|LS]$ represents the loss function for the risk metric adopted. To this end, Shahnazaryan and O'Reilly [45] suggested a design framework that aims at ensuring both a desirable mean annual frequency of collapse and a targeted level of expected annual loss (EAL), based on the conceptual guideline proposed by O'Reilly and Calvi [46]. In this way, the first quantity enables to manage the structural performance in terms of reliability, while the second one restricts the economic losses within an acceptable value.

1.4 OBJECTIVES OF THE STUDY

On the basis of the state of the art described in the previous sections, the present study focuses on the evaluation of the seismic performances of newly designed buildings. Therefore, the main novelty aspects could be briefly summarized as follows:

- Assessment of the seismic reliability of reinforced concrete frames and shear-walls structures designed according to the current provisions of the Italian Code;
- A numerical approach for the evaluation of a reliability-targeted behaviour factor (RTBF), which could be embedded in the actual force-based design approach;
- Enquiring the effects of the code-conforming sizing process also in terms of seismic risk by adding the loss term in the assessment paradigm;

As outlined in Section 1.2, the current Italian regulation is based on a uniform-hazard design philosophy, and this does not allow to directly control the effective seismic safety of buildings when observing all the mandatory requirements. Therefore, it is of interest to verify whether the code-conforming design process is capable of ensuring an adequate level of safety throughout the entire seismic hazard conditions. To this end, some of the aforementioned studies [21] have assessed the actual seismic reliability of new constructions in Italy. However, that project focused on analysing the effect of prescriptions for different structural resisting systems [47-50], while considering the variation of seismic hazard only for a limited number of sites. Hence, the present study aims to contribute to the evaluation of the seismic reliability of Italian code-conforming structures by investigating the effective spatial distribution of seismic failure rates along the entire Italian territory. To this end, an extensive numerical campaign has been implemented to provide seismic reliability maps of Italy with respect to bare and infilled RC frames and RC shear walls.

Moreover, Section 1.3 has emphasised the ever-increasing interest of the scientific literature in proposing design approaches to replace the force-based one of the Code [51]. In this context, the present study attempts to supply a series of maps containing a suitable reliability-targeted force reduction factor, taking advantage of the outcomes of the previous extensive numerical campaign. This proposal could yield a simplified design tool directly associated with the current approach that could be used by structural designers in common practice, avoiding a drastic increase in computational burden as required by the closed-form frameworks mentioned above.

Furthermore, the loss term represents a key factor in evaluating the seismic performance of structures. For example, it plays a crucial role in the allocation of stakeholders' resources or in the development of government risk reduction plans. However, the actual seismic risk of Italian code-conforming buildings has not been widely investigated [52]. As a consequence, the conclusive aim of this work lies in characterising the effects of current code prescriptions in terms of expected annual loss (EAL) by deriving a series of seismic risk maps of Italy.

1.5 OUTLINE OF THE THESIS

A brief description of the organisation of the thesis is presented herein.

- **Chapter 2** reports on the seismic reliability assessment of code-compliant reinforced concrete bare frames. In particular, the developed framework for parametrically designing and assessing the prototypes will be precisely described, and at the end, the resulting seismic reliability maps will be presented;
- **Chapter 3** evaluates the seismic performance of code-compliant RC infilled frames with the aim of investigating the stiffening effect of infill panels on their seismic performance. The main workflow of the previous chapter will be followed to show the results;
- **Chapter 4** derives the seismic reliability maps for code-conforming RC shear wall buildings. In detail, a parametric framework for design and assessment will be presented;
- **Chapter 5** develops a hands-on approach to derive the reliability-targeted behaviour factor q_{RT}. These coefficients will be evaluated for each of the three structural typologies analysed;
- **Chapter 6** assesses the seismic risk of code-conforming Italian buildings. Therefore, the expected annual loss (EAL) will be calculated for all Italian municipalities to provide seismic risk maps of newly designed buildings.

2 SEISMIC RELIABILITY OF CODE-CONFORMING RC BARE FRAME BUILDINGS

This chapter proposes a framework to assess the seismic reliability of bare reinforced concrete frames that comply with the current Italian Building Code. As discussed in the previous section, the target level of reliability is not explicitly set during the process provided by the Code; thus, the underlying relationship between seismic design intensity and the related performance is further evaluated through an extensive numerical campaign, and it leads to compute a series of Italian seismic reliability maps of the analysed archetypes.

2.1 CASE-STUDY BUILDINGS

The first step of the adopted framework consists of the definition of the main characteristics of the prototype buildings.

In detail, the reference archetype considered herein is typical of a residential building, both in terms of geometrical configuration and acting loads. Thus, the prototype layout consists of a rectangular shape in plan, which comprises five spans in one horizontal direction and three in the other, and each of these bays is five metres long. Three different elevation arrangements have been examined to capture the effect of height in terms of vulnerability. Specifically, the three, six and nine-story layouts are adopted and a constant floor height of three metres is considered. The frames are designed according to the high-ductility class (DCH) and medium-ductility class (DCM) provided in the Code and aimed at ensuring the fulfilment of the *capacity design* principles.

The typical values of floor loads for residential buildings have been considered, in particular values of about 5.5kN/m^2 and 0.5kN/m^2 have been applied to the roof for the dead load and the live load, respectively. The other floors have been loaded with a dead load of 6.5 kN/m^2 and a live load of 2.0 kN/m^2. It should be noted that these floor loads are representative of the one-way slab typology.

A concrete belonging to class C25/30 has been adopted, while the common steel B450C has been used for reinforcement. The main mechanical properties of these structural materials have been reported in subsequent tables.

Table 2-1 Mechanical properties of concrete C25/30

f_{ck} [MPa]	R_{ck} [MPa]	E_{cm} [MPa]	f_{cd} [MPa]
25.00	30.00	31475.81	14.17

Table 2-2 Mechanical properties of reinforcing steel B450C

f_{yk} [MPa]	E_s [MPa]	f_{yd} [MPa]
450.00	206000.00	391.30

Furthermore, the presence of the staircase has not been considered in the evaluation of the overall behaviour of the structure, and the infill panels have only been treated in terms of distributed loads along the perimeter of the building. The frames have been treated as fully restrained at the base, i.e. fixed condition, neglecting the explicit modelling of the foundation elements, and the beam-column joints have been assumed to be fully rigid (i.e. no panel zone effect has been considered). Moreover, a beam aspect ratio (i.e. height h over width b) higher than one is assumed because the Italian Code provisions do not allow the use of flat beams for DCH structures, and it would not be possible to compare the seismic performance between medium- and high-ductility frames. The columns present a square section, starting from the minimum dimension of 25 cm set out in the Code.

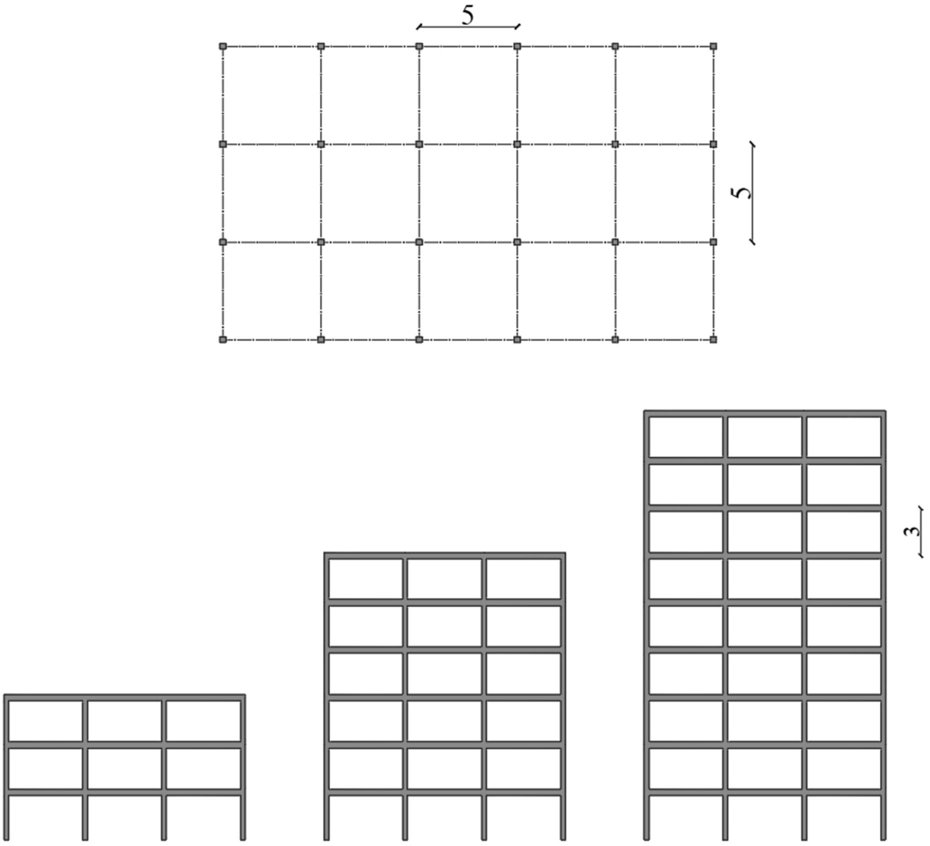

Figure 2-1 Planar and frontal views of the archetype frame building

2.2 SEISMIC DESIGN PROCEDURE

The definition of the global characteristics of the structural archetypes is followed by the seismic sizing process that complies with the code, which has been carried out according to the provisions of the current Italian building Code [3]. In this regard, a prototype seismic design tool capable of performing code-conforming sizing for all the possible levels of seismic intensity has been developed to assess the seismic failure rates of RC frames throughout the Italian territory. For this reason, a routine-based tool has been developed that links the Matlab [53] environment with OpenSees [54], as a way to perform a parametric design. Matlab has been adopted to implement the safety check conditions and meet all the qualitative prescriptions provided by the Code for the design workflow. On the other hand, OpenSees has been employed to build up the finite-element model of the structure to define all the forces acting on the structure. This is fundamental to allow for fast data interchange since the sections could be increased frequently due to the iterative nature of the design procedure.

The frames were analysed using a linear elastic analysis method. This choice has been made to present the typical approach to the design process of practitioners. Moreover, prototype structures meet the regularity conditions both in the plan and in the elevation, so it is possible to ignore the three-dimensional effects and only analyse them by means of a planar elastic analysis, without loss of generality [55]. Therefore, the seismic action is applied to the structure with a series of horizontal forces F_i, distributed along the height of the building, as reported in subsequent equations.

$$F_i = F_h \cdot \frac{z_i \cdot W_i}{\sum_j z_j \cdot W_j} \tag{2.1}$$

$$F_h = S_{ad}(T_1) W \lambda / g \tag{2.2}$$

In this approach, the nonlinear resources of the structure, both in terms of geometry and material, are captured by adopting a force reduction coefficient, which is called the behaviour factor q. This coefficient is different for the two ductility classes, namely, it takes a value of 3.9 and 5.85 for the DCM and DCH, respectively. In addition, the cracked condition of seismic-resisting structural elements has been considered by adopting a proper reduction of their lateral stiffness, as suggested by the Code.

Therefore, the use of this reduction coefficient leads to the computation of the design spectral acceleration S_{ad} starting from the elastic spectral acceleration S_{ae}. The latter is derived from the Uniform Hazard Spectrum (UHS) with a probability of exceedance of 10% over 50 years, and it is calculated in the period T_1 of the first fundamental vibration mode of the structure. This quantity is evaluated by means of a simplified formulation reported in the Operative Instructions of the Italian Code:

$$T_1 = C_1 \cdot H^{3/4} \tag{2.3}$$

where H is the total height of the structure and C_1 is a coefficient dependent on the structural resisting scheme, which in the case of RC frames takes a value of 0.075. A different range of $S_{ae}(T_1)$ has been considered for each elevation configuration, in order to catch the maximum spectral acceleration admissible in the Italian context. More in-depth, the three-storey frames are enclosed in an interval that spans between *0.1g-1.0g*, while the six- and nine-storey frames are included in the ranges of *0.1g-0.75g* and *0.1-0.5g*, respectively, and the design procedure has been performed with a spacing of *0.05g*.

The developed tool must be capable of optimising the design of structural elements without leading to oversizing, in order to fulfil the evaluation of the correlation between code-conforming solutions and their resulting vulnerability. Seismic performance could be significantly affected by solutions with gross element sections. Additionally, oversized solutions could lead to increased construction costs, which is not feasible in practical applications. Therefore, the workflow is highlighted in detail in Figure 2-2 and it is described in the following.

The first step of this process lies in the declaration of all relevant data, such as the number of floors and bays or the acting loads. At this point, the first tentative sections of the elements must also be stated; in particular, these have been set according to the minimum values prescribed in the Code; for example, a section of 25x25 cm has been assigned to the columns. Furthermore, the code-compliant sizing process of these types of structure is based on the so-called "*capacity design*" philosophy. Hence, this implies an initial declaration of the desirable ductility level by selecting one of the two classes provided by the Code, i.e. DCM or DCH, so that this choice will affect the value assumed by the behaviour factor q and also the qualitative provisions.

Given that, the flexural design of the beams is performed first by determining the acting bending moment M_{sb} and then evaluating the related required longitudinal reinforcement ratio ρ_{lb}. As part of an iterative loop, the most suitable combination in terms of diameter and number of bars is calculated only if the required reinforcement ratio ρ_{lb} is within the lower and upper bound limits ρ_{min} and ρ_{max}, respectively. Otherwise, in case ρ_{lb} exceeds the maximum admissible value, the beam section height is increased and the process is started again from the beginning until the flexural criterion is satisfied. At this point, the transverse reinforcement of the beams is determined by fulfilling the capacity design rule, in order to prevent brittle failures in favour of the flexural one. Namely, the design shear force V_{bsd} is computed by imposing the equilibrium of the beam with the application at the two ends of the predetermined bending resisting moments M_{bRd}, which are increased by a safety coefficient factor.

Moreover, the flexural capacity of the columns M_{cRd} has to be determined according to equilibrium constraints and capacity design principles because it is a function of the bending resisting moments of the beams M_{bRd}. Specifically, the acting bending moment of columns $\mathrm{M_{cRd}}$ is extracted from the analysis and multiplied by an incremental coefficient based on the resisting moments of the adjacent beams, in order to fulfil the principle of *'weak beam – strong column'*. After this, the effective number of longitudinal bars and their diameters are evaluated by means of an iterative loop similar to the one developed earlier for the beams. Therefore, if the reinforcement ratio ρ_{lc} exceeds the upper limit ρ_{cmax} the column section increases, and the process starts again from the beginning. In contrast, if ρ_{lc} stands within the lower and upper bound limits (ρ_{min}, ρ_{max}), the procedure allows the computation of the resisting moments of the columns M_{cRd} and subsequently the actual amount of longitudinal reinforcement. Consequently, the acting shear demand V_{csd} is determined by imposing equilibrium constraints by using the above-mentioned M_{cRd}. In addition, the section at the base of the columns needs to fulfil ductility detailing imposed by the code in order to guarantee an adequate capacity in terms of energy dissipation. The fulfilment of all the seismic prescriptions provided by the Code ensures the achievement of a global ductile behaviour of the designed buildings since they avoid the occurrence of soft-storey failures because of the overstrength factor against brittle failure mechanisms.

At the end of this procedure, all the design outputs, such as geometrical features of structural elements, as well as transverse and longitudinal reinforcement details, are stored in a series of matrices to use as the main inputs for the seismic fragility assessment framework.

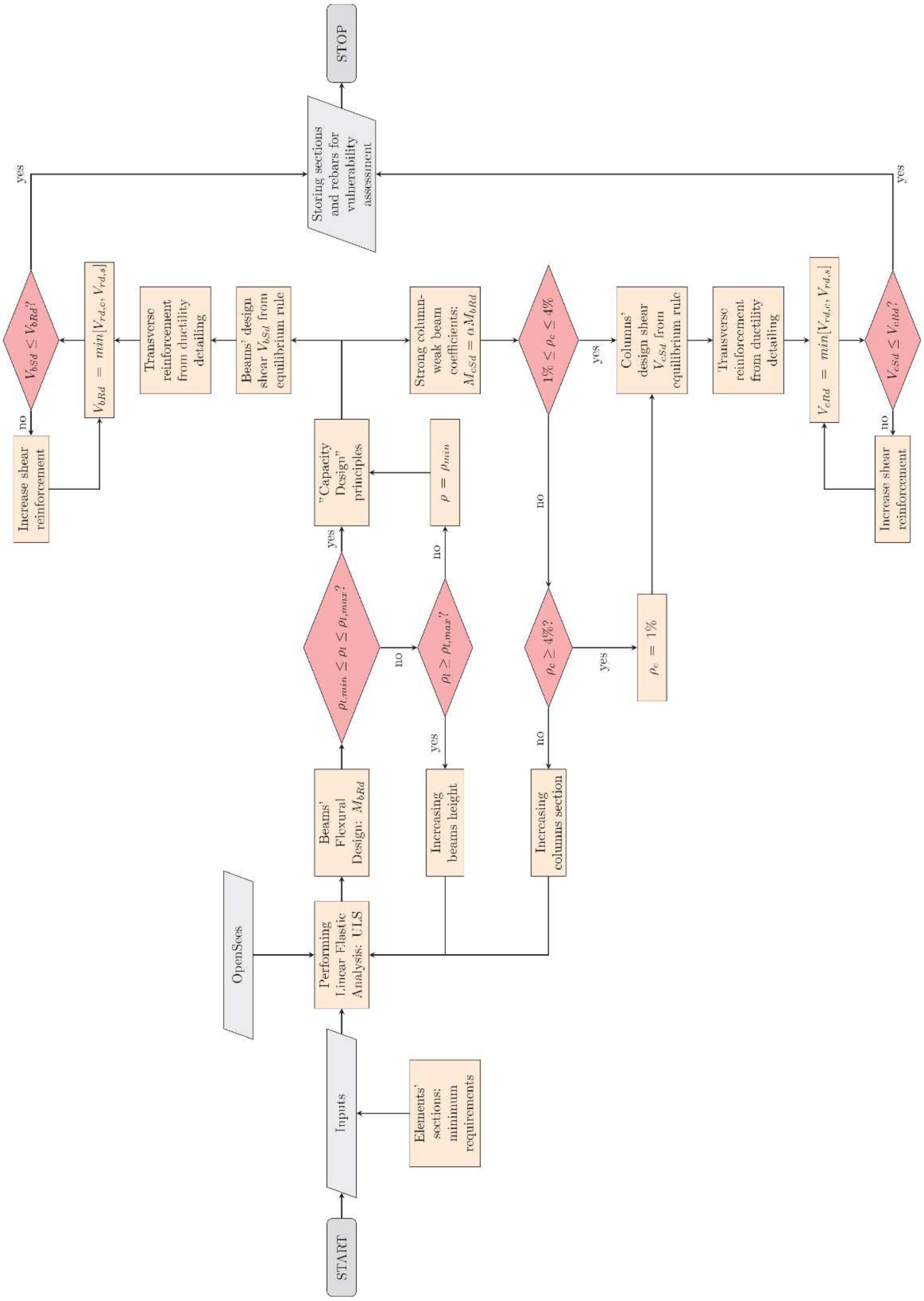

Figure 2-2 Flowchart for the seismic design of frames

2.3 SEISMIC VULNERABILITY ASSESSMENT

A tool capable of assessing the seismic response of the frames has been developed, starting from the results obtained at the end of the design process. This platform follows the same principle as the one realised for the design procedure. Namely, the interoperability between Matlab and OpenSees has been utilised, where the former was adopted for the pre- and post-processing phases, and the latter allowed the nonlinear modelling of the frames for performing both static and dynamic nonlinear analyses. Therefore, the main steps of the framework have been reported in Figure 2-4, and they are described in detail below.

The first step of the process lies on the creation of the nonlinear assemblies in the finite element environment to characterise the inelastic properties of frames.

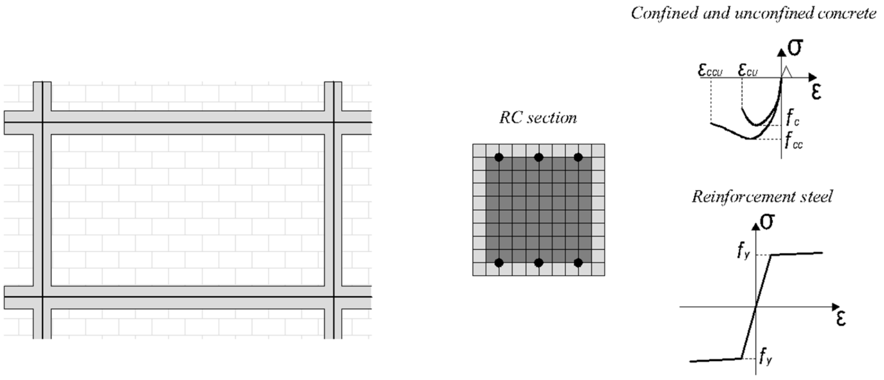

Figure 2-3 Nonlinear modelling of RC bare frames

At this aim, the fibre-cross-section discretization theory has been assigned to the mono-dimensional frame elements, so that it has been necessary to define a series of nonlinear stress-strain material laws, which have been calculated using the mean values of the resistance strength:

$$f_{cm} = f_{ck} + 8 \cdot [MPa] \tag{2.4}$$

$$f_{ym} = f_{yk} \cdot 1.15 \cdot [MPa] \tag{2.5}$$

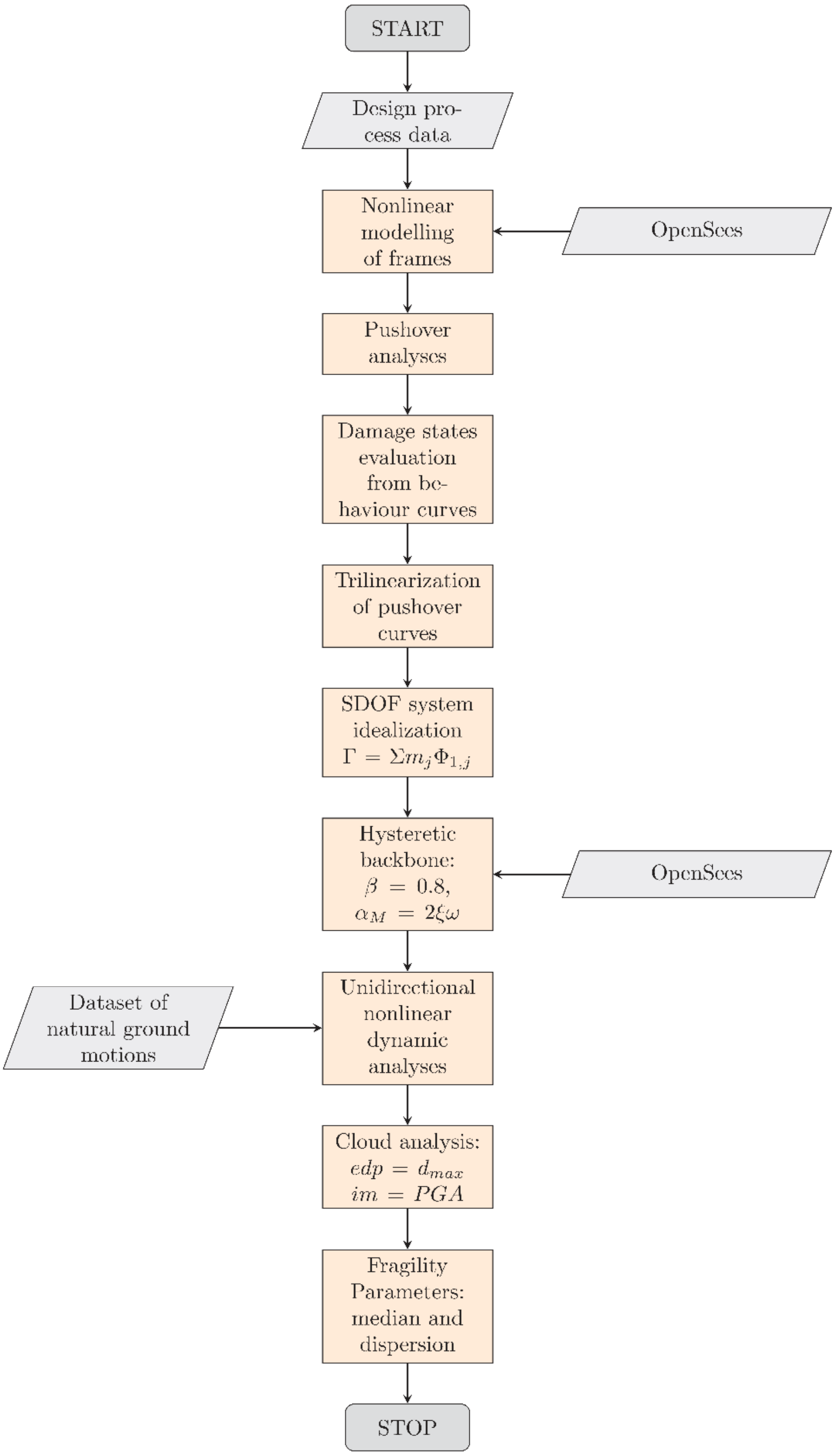

Figure 2-4 Flowchart of the vulnerability assessment

Two different laws have been assigned to concrete as a means of determining the effect of the confinement action exploited by transverse reinforcement. Hence, the cover concrete is modelled with *Concrete01* from the OpenSees library, while the core one is simulated with *Concrete04* material and the parameters of the two are calibrated to fit the Mander model [56]. On the other hand, the reinforcement steel of the longitudinal bars is modelled using the *Hysteretic* material, which has been calibrated to represent the Menegotto-Pinto model [57]. Fibre-based elements account only for the axial-bending interaction, so they are not able to directly consider the shear mechanism. However, since the main objective of the capacity design is to prevent shear brittle failure, it could be possible to focus only on the evaluation of the flexural response without loss of generality. After frame assembly, a series of nonlinear static analyses were performed to depict the behaviour curves of the frames (Figure 2-5 Figure 2-6 Figure 2-7). This step aims to characterise the behaviour curves of the frames so that it would be possible to calibrate the Single Degree of Freedom (SDOF) system, which would be adopted to carry out nonlinear dynamic analyses in order to reduce the computational burden of the framework.

The pushover curves show an increase in the base shear proportionally to the elastic spectral acceleration, which proves the goodness of the developed design procedure. Furthermore, the displacement corresponding to the *'yielding point'* decreases as the acceleration increases, and this could be ascribed to the greater dimension of the sections, which is related to a higher global stiffness. Moreover, there is no clear discrepancy in terms of the ultimate displacement capacity between the two classes of ductility, given the number of floors. On the contrary, the DCM frames reach a higher base shear than the DCH ones. This unexpected trend could be explained by the fact that when designing a building in DCM, a lower value of behaviour factor is assumed following design code prescriptions, thus leading to larger seismic design actions, and, as a consequence, is reflected in a more restrictive design if compared to the companion DCH layouts. In addition, with the varying floors is possible to observe a slight enhancement both in terms of ultimate displacement and maximum base shear.

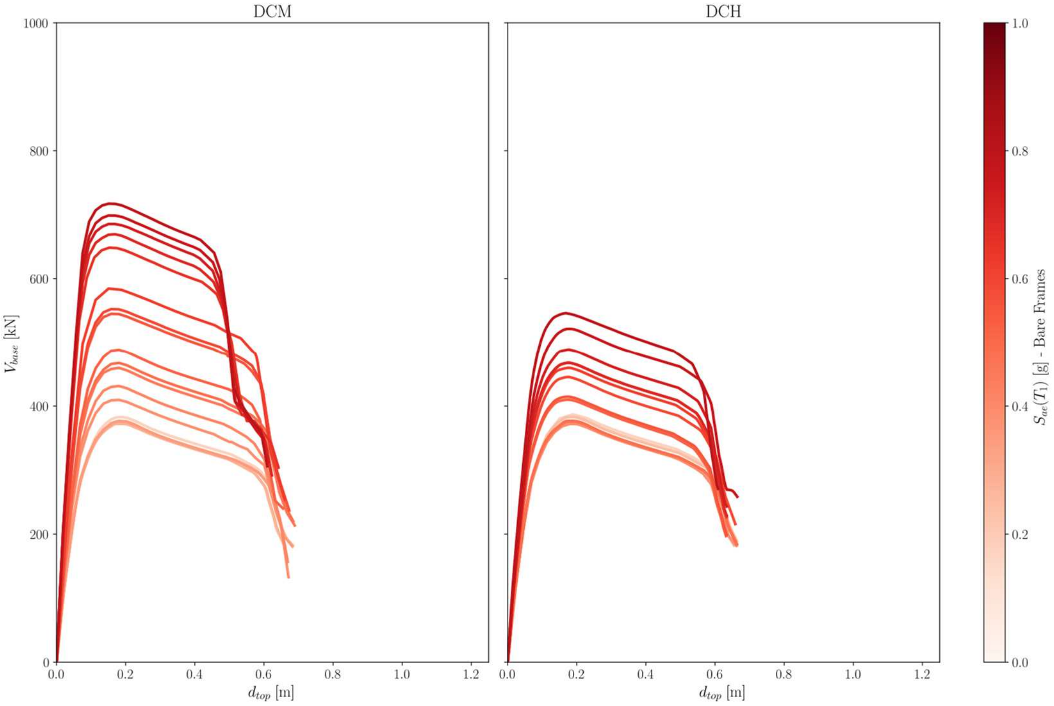

Figure 2-5 Pushover curves of code-compliant bare frames - 3 storeys

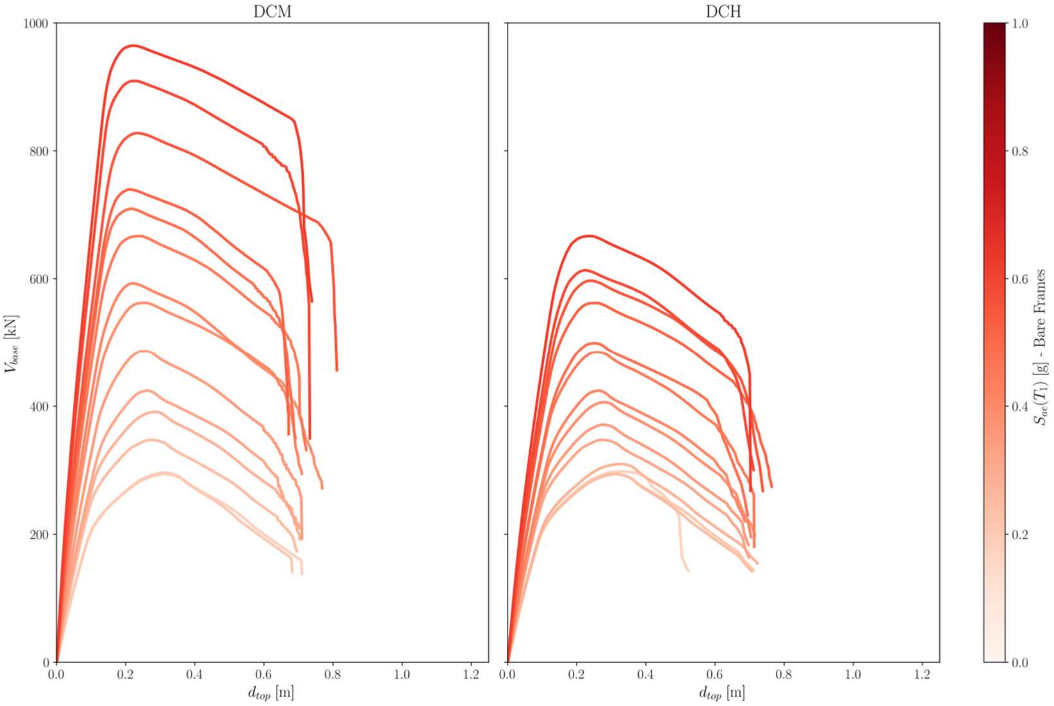

Figure 2-6 Pushover curves of code-compliant bare frames - 6 storeys

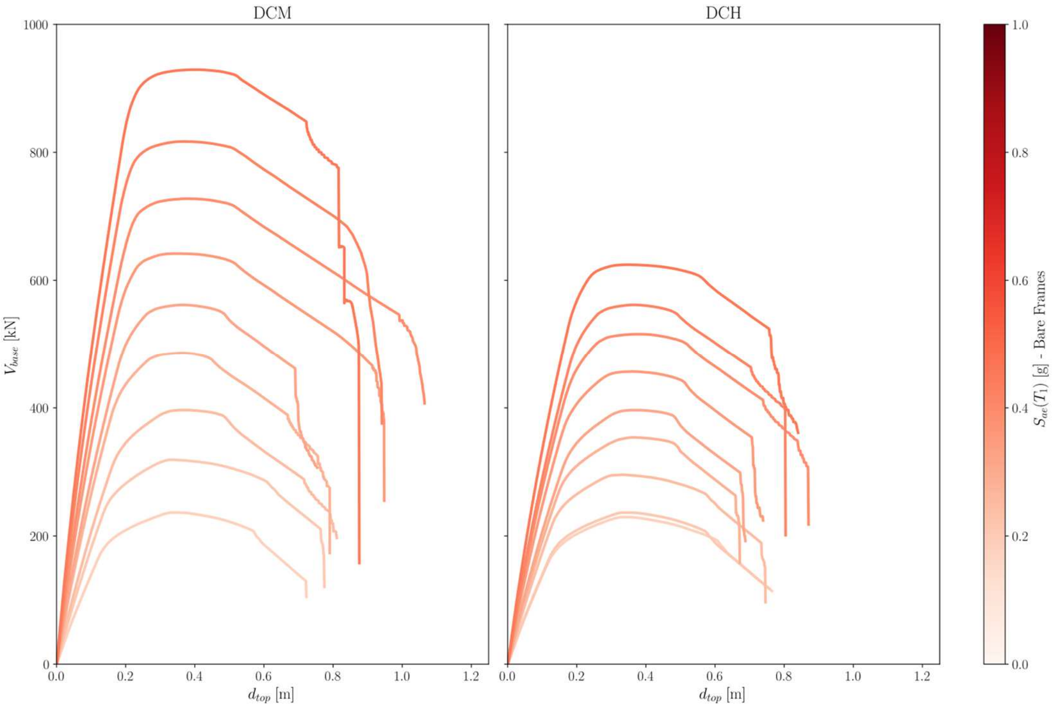

Figure 2-7 Pushover curves of code-compliant bare frames - 9 storeys

As mentioned above, these capacity curves have been enveloped to obtain the definition of an equivalent SDOF system, which would be adopted to carry out NLTHAs. This choice was possible due to the global configuration of the prototypes. They meet the regularity requirements both in plan and in elevation, so the torsional effects do not affect their seismic response. However, before describing the idealisation procedure, some considerations about this conceptualisation have to be made. First, it should be underlined that in the recent literature, there are an increasing number of studies that attempt to simplify the assessment of fragility using a hybrid approach, which consists of determining the capacity curve using pushover techniques and then evaluating the dynamic response using equivalent SDOFs [58-61]. More in-depth, a recent publication by Suzuki and Iervolino [59] revealed that the idealisation of the eSDOF system could quite often effectively address the seismic failure rate of the related MDOF building. Moreover, eSDOFs were shown to be less prone than 3D models to exhibit the problem of dynamic numerical instability, which is a phenomenon that detrimentally affects the statistical process of deriving fragility curves.

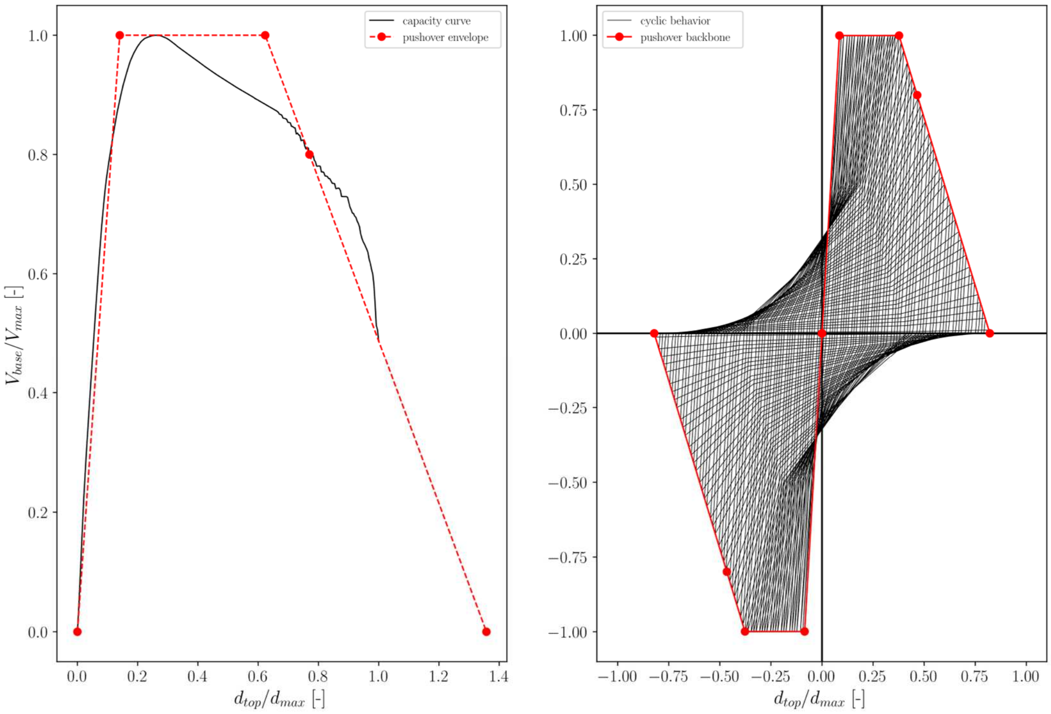

Figure 2-8 Backbone and Hysteretic Behaviour of SDOF – Bare Frames

Therefore, SDOF systems have been characterised by means of a tri-linearized backbone starting from the capacity curves of the frames. This strategy has already been widely adopted in the literature[62], in particular, it has followed the approach contained in [58]. Specifically, the force-displacement behaviour has a first elastic portion and a second perfectly plastic branch, which precedes the last linear descending phase. The relevant points have been calibrated using the principle of equal areas between the capacity curves and the idealised one, and then the first modal participation factor Γ has been used to switch from the MDOF system to the SDOF system. As noted in Figure 2-8, the force at the first and second points is fixed equal to the maximum base shear, while the '*yield displacement'* is derived by equalising the area from the initial point to the one mentioned. Therefore, the '*post-capping*' trend is determined in a similar way. Subsequently, the dynamic behaviour of the equivalent SDOF has been recreated through a hysteretic peak-orientated model without strength/stiffness degradation in the OpenSees environment, in order to be able to perform the vulnerability assessment of global structures [63]. Finally, it should be noted that, for simplicity, a damping ζ proportional to the mass matrix has been set.

The next step of the main framework consists in derive the fragility curves by means of techniques based on nonlinear dynamic analyses, and in particular the present study applies the so-called *Cloud Analysis* [9] because it showed the highest effectiveness and flexibility for such types of analysis. In this method, the system is subjected to a series of N_{GM} unscaled ground motion records, and the maximum response of a structural parameter *edp* is recorded during the analysis. In this way, the fragility curve of a specific damage state *DS* takes its origin from linear regression in the logarithmic space of the N_{GM} sample of ground motion intensities *im* and their respective *edp*. In this way, the term $P[f|im]$ representing the fragility in the seismic reliability integral (1.4) is stated with the following equation:

$$P[f|im] = P\left[EDP > \overline{edp}\middle|im\right] = 1 - \Phi\left[\frac{ln\left(\overline{edp}\right) - ln\,(\theta)}{\sigma}\right] \tag{2.6}$$

$$ln(\theta) = ln(a) + b \cdot ln(im) \qquad \sigma = \sqrt{\frac{\sum_{i=1}^{N_{GM}}[ln\,(edp_i) - ln\,(\theta)]^2}{N_{GM} - 2}} \tag{2.7}$$

where the operator Φ represents the normal cumulative density function, $\overline{edp}$ is the threshold of a specific damage state and θ and σ are the estimate of the median and the standard deviation of the logarithmic distribution [64], respectively. This last parameter σ embodies some uncertainties, such as the record-to-record variability and the modelling uncertainties. In the present study, the peak ground acceleration *PGA* has been picked as the intensity measure representative of each ground motion, while the displacement of the free node at the top of the equivalent SDOF system stands for the *edp* parameter.

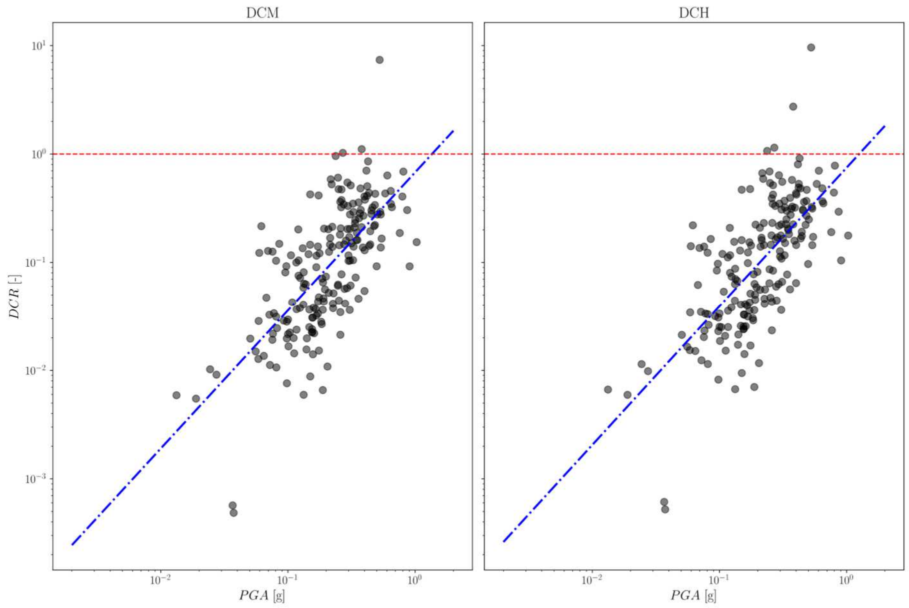

Figure 2-9 Example of the cloud of points – 6 storeys frame – ds=NC

As a consequence, it is necessary to specify the data set of the ground motion records and the desirable damage states to obtain the fragility curves. The former was assembled by collecting a group of 200 unscaled records that belong to the two horizontal components of 100 different seismic events. This dataset has been built with an M_w-R_{epi} criterium that is consistent with the seismic disaggregation process. Specifically, a range of variation for magnitude and epicentral distance has been fixed, and, for each step, a series of five events has been collected. However, it should be underlined that increasing the magnitude detrimentally decreases the number of events; thus, for high-intensity events, the selection changed from five to two. Hence, a sample of uniformly spatial events was obtained, as reported in Figure 2-12. In addition, Figure 2-10 and Figure 2-11 show the accelerograms for all the selected events.

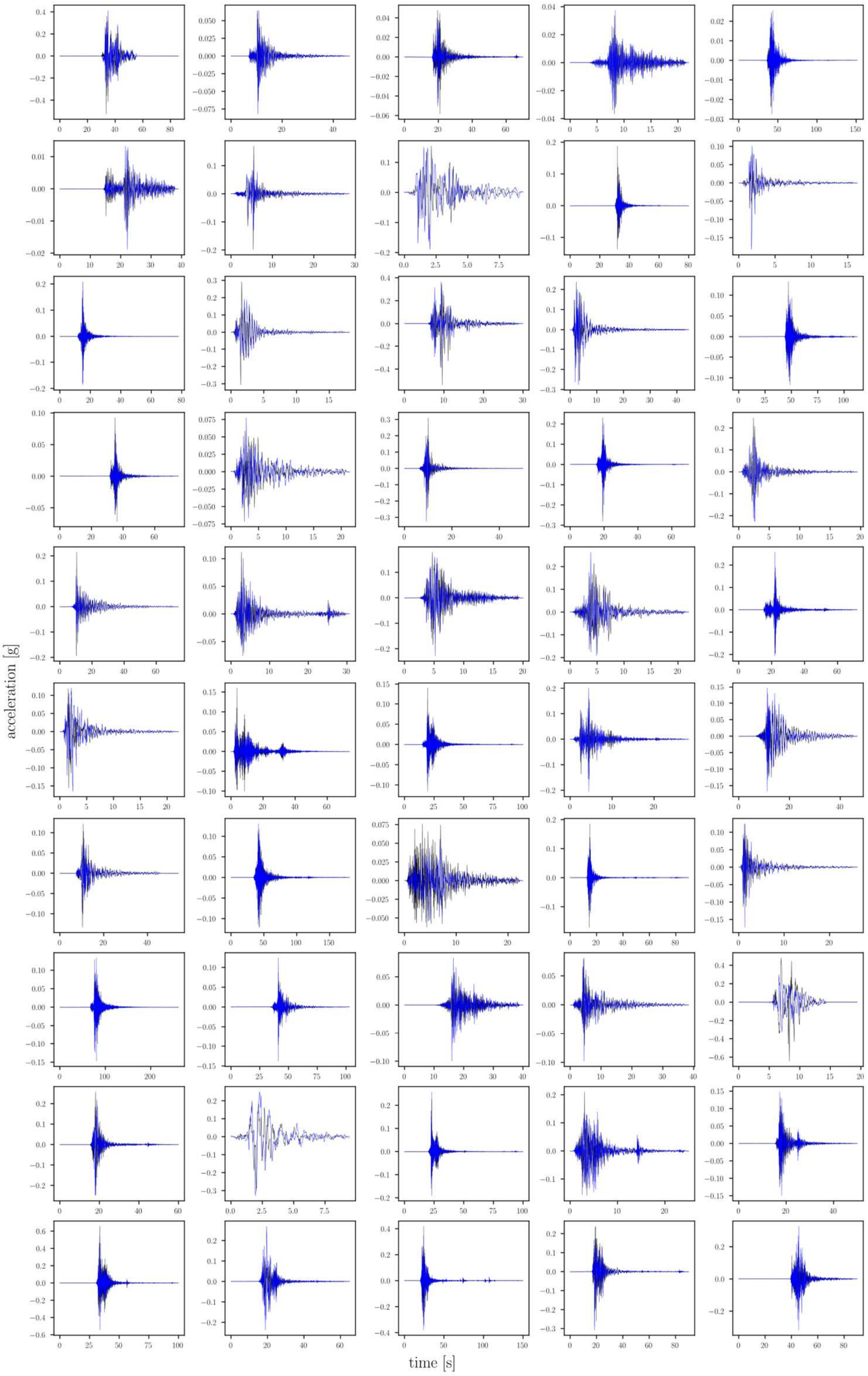

Figure 2-10 Ground motions: E-W in black and N-S in blue - Part I

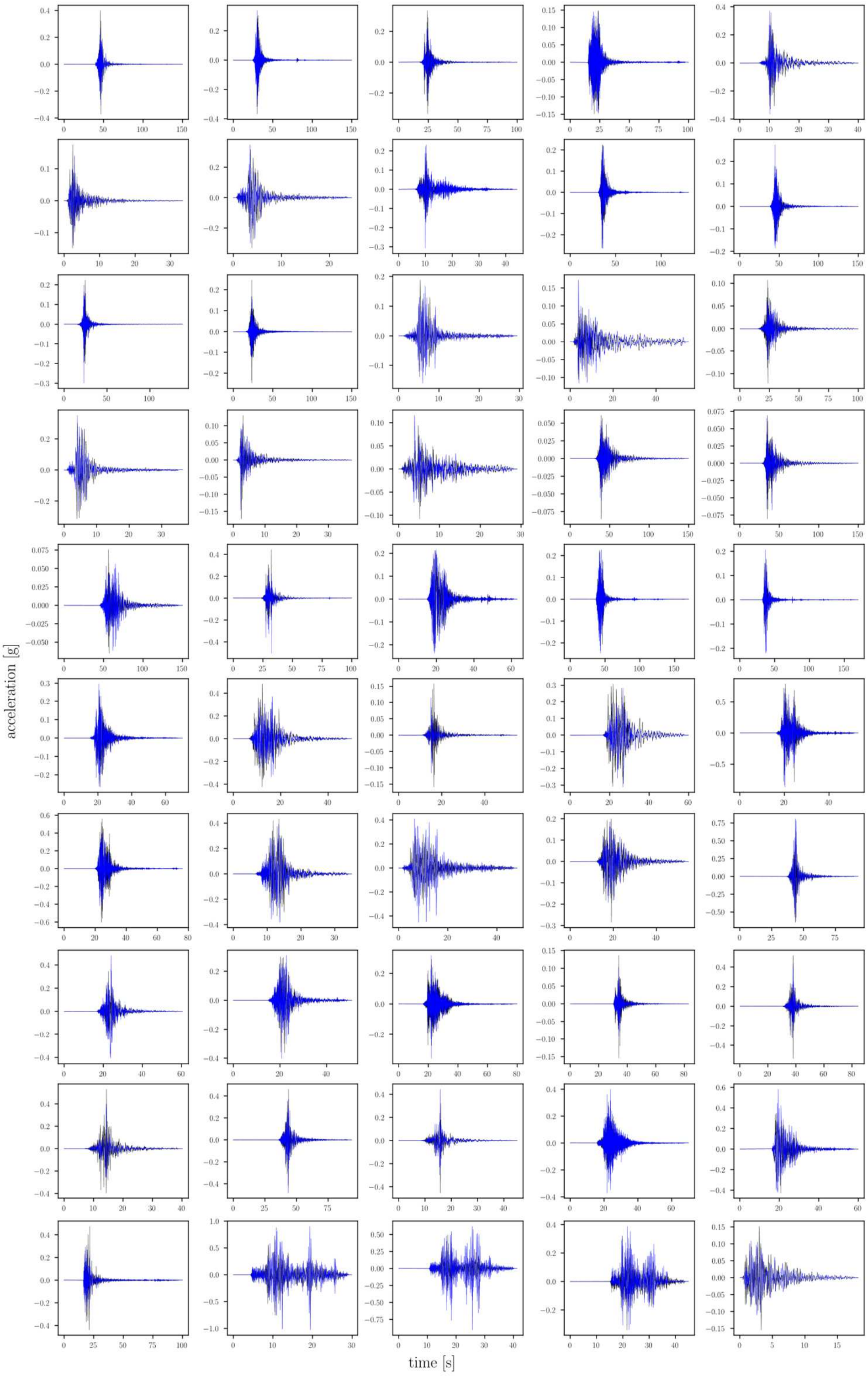

Figure 2-11 Ground motions: E-W in black and N-S in blue - Part II

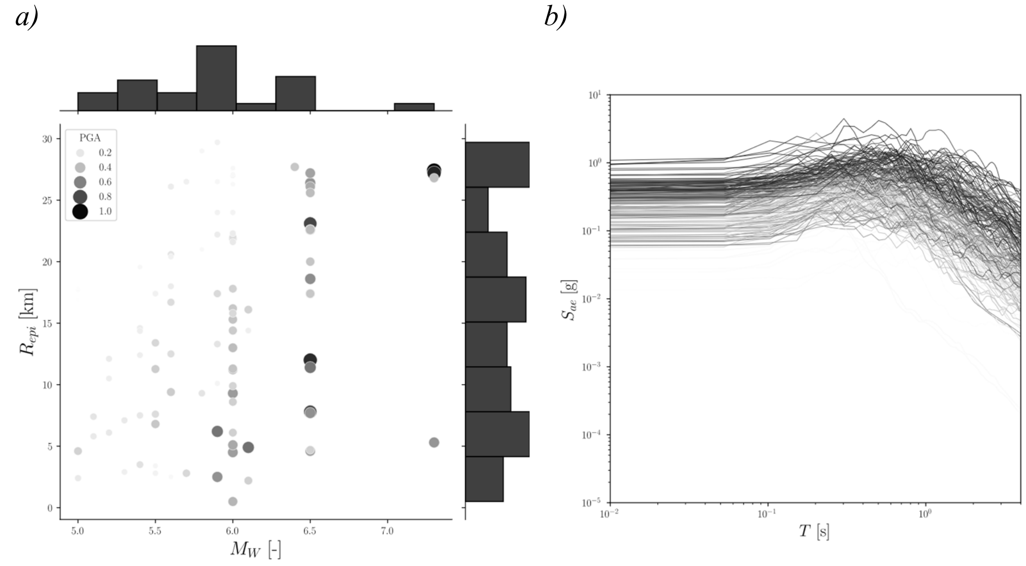

Figure 2-12 a) Dataset of the selected events, b) Elastic spectra of the 200 ground motions

The engineering demand parameter considered during the nonlinear dynamic analyses to capture the structural response of the equivalent systems has been set in terms of top displacement, since the objective is to account for the flexural behaviour of code-conforming frames designed with capacity-design rules. Therefore, four relevant damage states have been identified:

- *ds_1 = Slight Damage (SD),* which coincides with the displacement where the backbone of the SDOF reaches the elastoplastic branch, thus this state represents the *yield* of the system;
- *ds_2 = Moderate Damage (MD)* is reached with the onset of the *capping-point* displacement;
- *ds_3 = Near Collapse Damage (ND)* is located at 80% of the maximum base shear in the descending branch of the behaviour curve, in compliance with [58];
- *ds_4 = Collapse Damage (CD),* occurs at a top displacement corresponding to a base shear approximately 50% of the maximum;

Hence, all the nonlinear dynamic analyses could be performed for each elevation configuration, ductility class, and elastic spectral acceleration $S_{ae}(T_1)$, to obtain the fragility parameters θ and σ for each damage state previously defined. To this end, Figure 2-13 presents the correlation between the median of the vulnerability θ and the elastic spectral acceleration S_{ae}, which is the parameter that characterises the seismicity of the theoretical construction site.

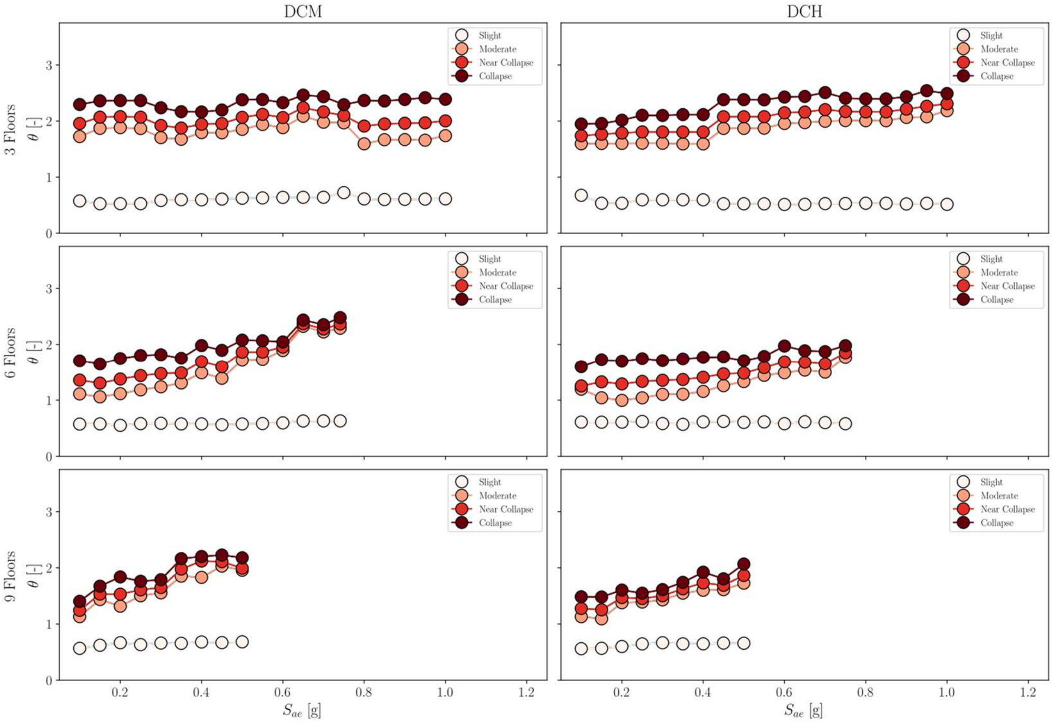

Figure 2-13 Correlation between the median parameter θ and the spectral acceleration S_{ae}

Firstly, Figure 2-13 indicates that the vulnerability of the frame decreases with increasing number of floors, given the damage state. The not-perfectly monotonic trend of the median fragility values could be a consequence of the design phase. More in-depth, this procedure has been developed to lead to safety checks as close as possible to unitary values, and at the same time, it tries to accurately recreate common practical design assumptions, for example with the adoption of discrete values for the number and diameters of rebars. Consequently, this may cause slightly overdesigned conditions when a change in section dimensions or reinforcement amount is required, which results in an irregular trend of fragility values.

Furthermore, the results do not show significant differences between the two classes of ductility, as the median values are quite similar for the same elevation configuration. On the contrary, there is a discrepancy in the global trend of the values referring to the variation of elastic spectral acceleration. More in depth, the three-storey frames display an almost steady trend for all the possible levels of seismic intensity, whereas the six- and nine- storey exhibit a behaviour proportional to the S_{ae}, except for the slight damage state.

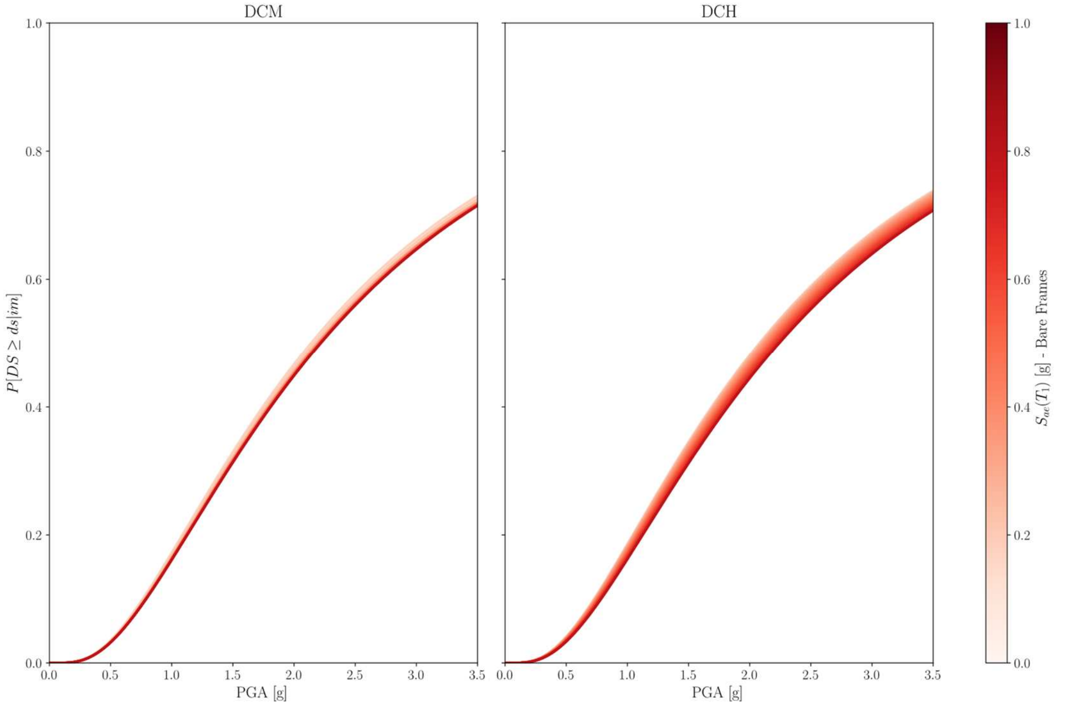

Figure 2-14 Fragility curves code-compliant bare frames - 3 storeys - NC

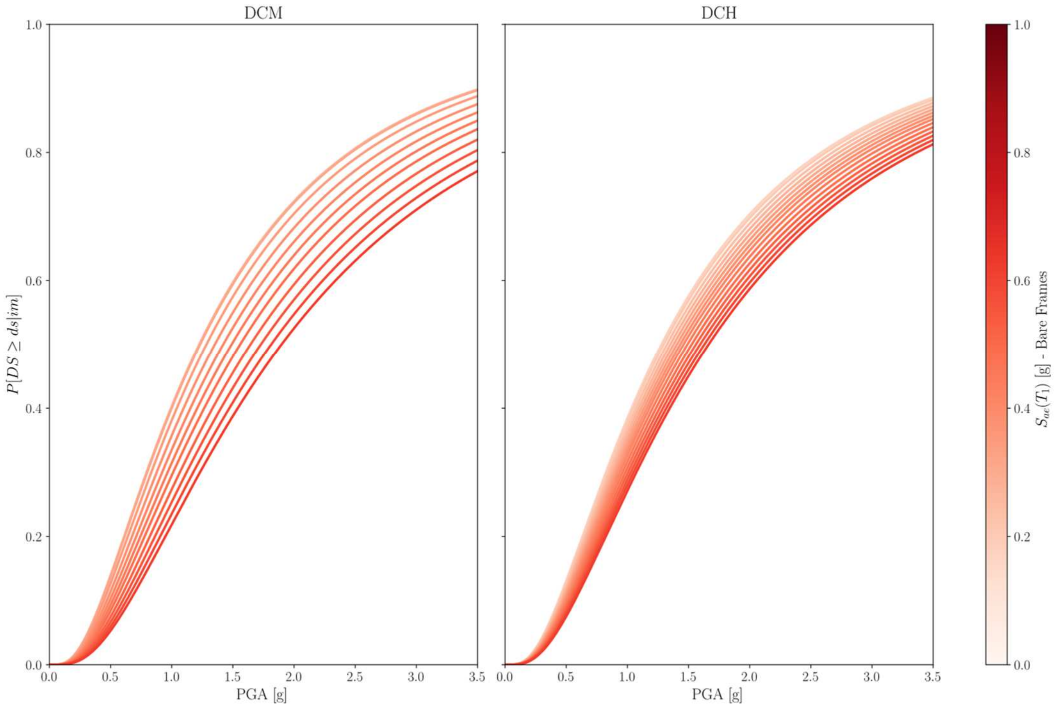

Figure 2-15 Fragility curves code-compliant bare frames - 6 storeys - NC

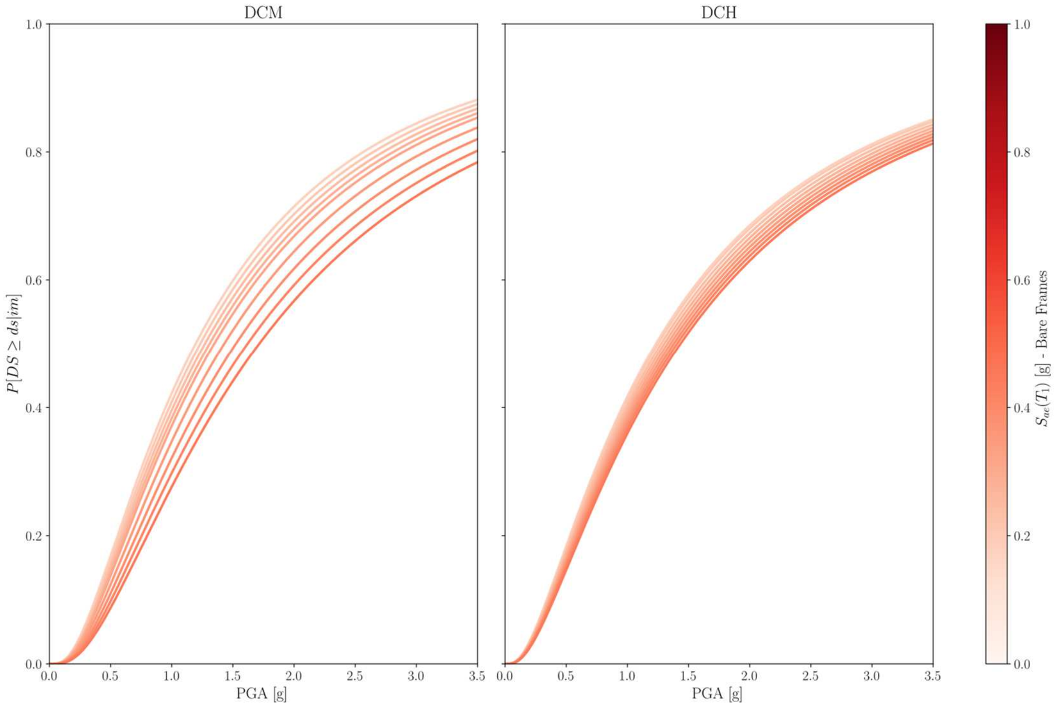

Figure 2-16 Fragility curves code-compliant bare frames – 9 storeys - NC

The fragility parameters could be combined to derive the fragility curves associated with each damage state. For instance, from Figure 2-14 to Figure 2-16 the near collapse cases have been reported, and they are consistent with what was pointed out in the previous paragraph.

2.4 SEISMIC RELIABILITY MAPS

The last step of this framework aims to evaluate seismic failure rates of code-compliant frames along Italian territory, and a sketch of the required workflow is outlined in Figure 2-17. Hence, a series of seismic reliability maps could be formed to outline the level of performance achieved with current design practice. To this end, the seismic reliability integral has to be solved for all over 7900 Italian municipalities; therefore, this calculation is performed by ideally matching the construction site with the centroid of each town. This assumption is consistent with the fact that most buildings are usually close to the urban centre rather than the border areas.

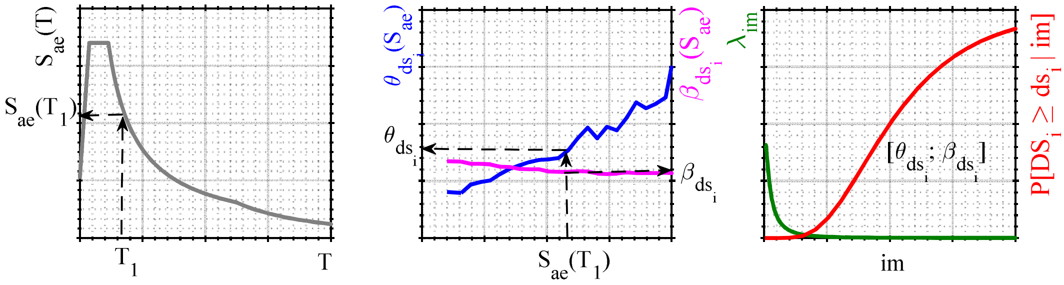

Figure 2-17 Sketch of the workflow for the code-compliant seismic reliability calculation

First, a link must be established between the results of the vulnerability assessment and the seismicity of each municipality. For this reason, the elastic spectral acceleration $S_{ae}(T_1)$ with a 10% 50-year exceedance probability was derived by computing the related uniform hazard spectrum starting from the effective Italian seismic hazard map. In this way, it was possible to establish the level of seismic intensity that would be adopted to design the prototype frames located at the site of interest. Consequently, the fragility parameters θ and σ were determined, in order to compute the fragility curves that would be convoluted with the seismic hazard ones to determine failure rates, for each damage state.

Second, it is necessary to evaluate the seismic hazard curves for all municipalities. These have to be represented with the same intensity measure *im* adopted during the fragility analysis, which is the peak ground acceleration *PGA*. This quantity could be expressed by multiplying the peak acceleration estimated at the bedrock *ag* by an amplification factor which depends on the soil condition of the site of interest. To this end, the soil map realised in the study by [65] leads to the identification of the soil class in each centroid. On the other hand, starting from the current Italian seismic hazard map, nine UHS, for return periods equal to 30, 50, 72, 101, 140, 201, 475, 975 and 2475 years, are computed considering a soil category of type A, which represents the rock-like geological formation. Therefore, these acceleration values are amplified by using the soil amplification factor provided by the Code [3].

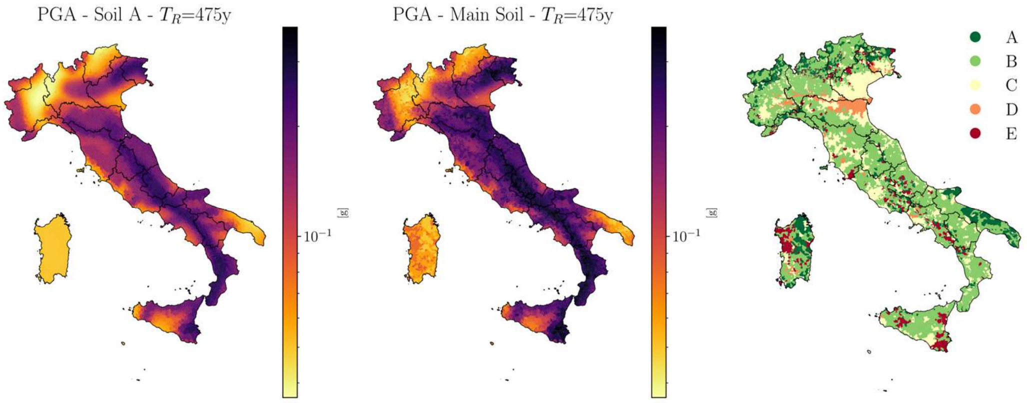

Figure 2-18 Seismic hazard maps and main soil category

Figure 2-18 plots both the seismic hazard map with a ground acceleration of 50-year exceedance probability computed at the bedrock and the one determined by assuming the effective soil condition at each site. Hence, this figure outlines the strong effect of considering the soil condition in the spatial distribution of the seismic hazard. For instance, the high amplification factor of soil categories C or D spreads the seismic hazard of the sites in the northeast of Italy, in a way that they reach values of intensity measure similar to those of the well-known locations in the centre of Italy.

However, the hazard curve is derived by fitting the nine amplified accelerations at different return periods. In the literature some solutions are proposed, such as the closed-form approach developed in [66], in the present study a quadratic function in the logarithmic space is followed, as suggested in [67] for Italy:

$$\lambda_{im}(im) = k_0 e^{[-k_1 ln(im) - k_2 ln^2(im)]} \tag{2.8}$$

The coefficients k_0, k_1, and k_2 are calculated by applying the minimisation of the interpolation error.

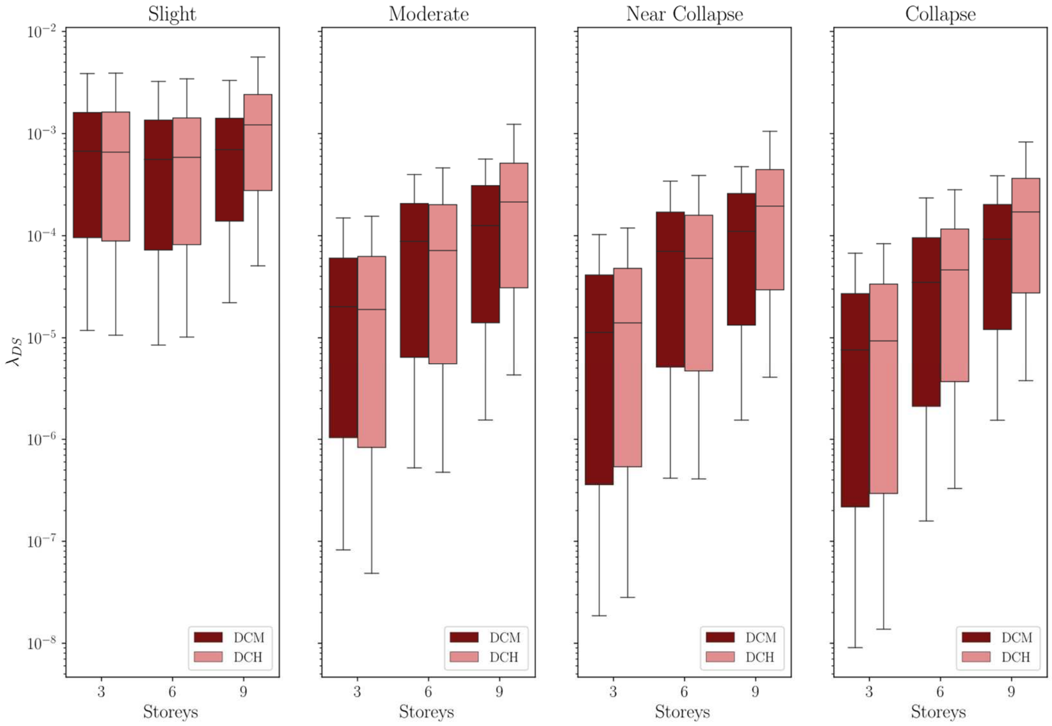

Figure 2-19 Seismic failure rates boxplot – bare frames

Finally, the seismic hazard curves that account for the actual soil condition of each municipality are coupled with the fragility curves referred to each bare frame archetype in order to numerically solve the integral (1.4) and thus obtain the code-compliant seismic failure rates for all damage states.

Table 2-3 Summary of failure rates – Bare Frames

Case	**Damage State**	λ_f		
		Min	***Max***	***Mean***
3 -DCH	*ds_1 (SD)*	1.06E-05	5.61E-03	9.70E-04
	ds_2 (MD)	4.85E-08	2.73E-04	3.74E-05
	ds_3 (NC)	2.82E-08	2.36E-04	2.92E-05
	ds_4 (C)	1.37E-08	1.89E-04	2.10E-05
3 -DCM	*ds_1 (SD)*	1.18E-05	5.65E-03	9.72E-04
	ds_2 (MD)	8.23E-08	2.94E-04	3.75E-05
	ds_3 (NC)	1.86E-08	2.28E-04	2.58E-05
	ds_4 (C)	9.07E-09	1.66E-04	1.72E-05
6 -DCH	*ds_1 (SD)*	1.02E-05	4.67E-03	8.47E-04
	ds_2 (MD)	4.76E-07	4.61E-04	1.13E-04
	ds_3 (NC)	4.09E-07	4.03E-04	9.06E-05
	ds_4 (C)	3.30E-07	3.36E-04	6.76E-05
6 -DCM	*ds_1 (SD)*	8.49E-06	3.89E-03	7.88E-04
	ds_2 (MD)	5.25E-07	3.97E-04	1.13E-04
	ds_3 (NC)	4.16E-07	3.42E-04	9.31E-05
	ds_4 (C)	1.58E-07	2.63E-04	5.38E-05
9 -DCH	*ds_1 (SD)*	5.07E-05	6.18E-03	1.43E-03
	ds_2 (MD)	4.28E-06	1.43E-03	3.02E-04
	ds_3 (NC)	4.06E-06	1.13E-03	2.60E-04
	ds_4 (C)	3.76E-06	8.28E-04	2.13E-04
9 -DCM	*ds_1 (SD)*	2.21E-05	4.04E-03	8.55E-04
	ds_2 (MD)	1.55E-06	5.63E-04	1.68E-04
	ds_3 (NC)	1.54E-06	4.74E-04	1.44E-04
	ds_4 (C)	1.54E-06	3.86E-04	1.16E-04

The results are presented graphically in Figure 2-19, which shows their ranges of variation, and by means of Table 2-3, where the minimum, maximum, and mean values are reported, respectively. There is no remarkable difference in failure rates between the two classes of ductility. The DCM leads to a slightly better performance only for the last two damage states (i.e. *NC* and *C)*, and this trend could be ascribed to the adoption of a higher behaviour factor in the design process, which seems to address better the seismic safety than the ductility provisions of DCH. Furthermore, seismic safety appears to be inversely proportional to the number of storeys of the buildings, since the 9-storey frames have a range of variation shifted above the one of the 6- and 3-storey ones.

The slight damage displays a different performance trend referring to the number of floors. Specifically, there is no significant discrepancy between the three cases in terms of mean and extreme values. For instance, the overall failure rates span from $1.06 \cdot 10^{-5}$ to $5.61 \cdot 10^{-3}$ for the DCH 3-storey cases, and range between $1.02 \cdot 10^{-5}$ and $4.67 \cdot 10^{-3}$ and between $5.07 \cdot 10^{-5}$ and $6.18 \cdot 10^{-3}$ for the DCH 6- and 9-storey ones, respectively. The same overall behaviour could be described for the medium-ductility class condition.

From the second damage state, i.e. *moderate damage*, there is a switch in the global tendency of the data. Namely, seismic failure rates increase according to the number of floors, and this is highlighted by the mean values in Table 2-3, which, for instance, range from a value of $3.75 \cdot 10^{-5}$ to $1.68 \cdot 10^{-4}$ for the DCM 3-storey and DCM 9-storey case, respectively. This trend could be ascribed to the results of the pushover analyses, which outlined a soft enhancement in maximum displacement with the increase of the floors and this could reflect in a lowering of the fragility performance. Furthermore, Figure 2-19 shows a wide dispersion of the failure rates for the three-storey frames. This trend appears to be directly related to the tendency of the median values of the fragility analyses. Figure 2-13 outlined an almost steady vulnerability performance of the 3-storey frames when correlated with the elastic spectral acceleration, i.e. the level of the seismic design intensity, while the 6- and 9-cases exhibited an improvement of the median. Hence, this fragility invariance of the formers led to the evaluation of failure rates that are strictly proportional to the hazard of the site of interest. However, the decrease in vulnerability observed for the 6- and 9-storey buildings is capable of slightly mitigating the effects of the hazard in the final determination of the reliability. Therefore, this behaviour is also confirmed for the *near collapse* and *collapse* damage state. In the former, the minimum mean value of failure rates of $2.58 \cdot 10^{-5}$ is registered for the DCM 3-storey frames, while the maximum of the mean of $2.60 \cdot 10^{-4}$ is observed for the DCH 9-storey frames. In the latter, the worst reliability condition is attained with a value of $2.13 \cdot 10^{-4}$, while the safest case takes a value of $1.72 \cdot 10^{-4}$.

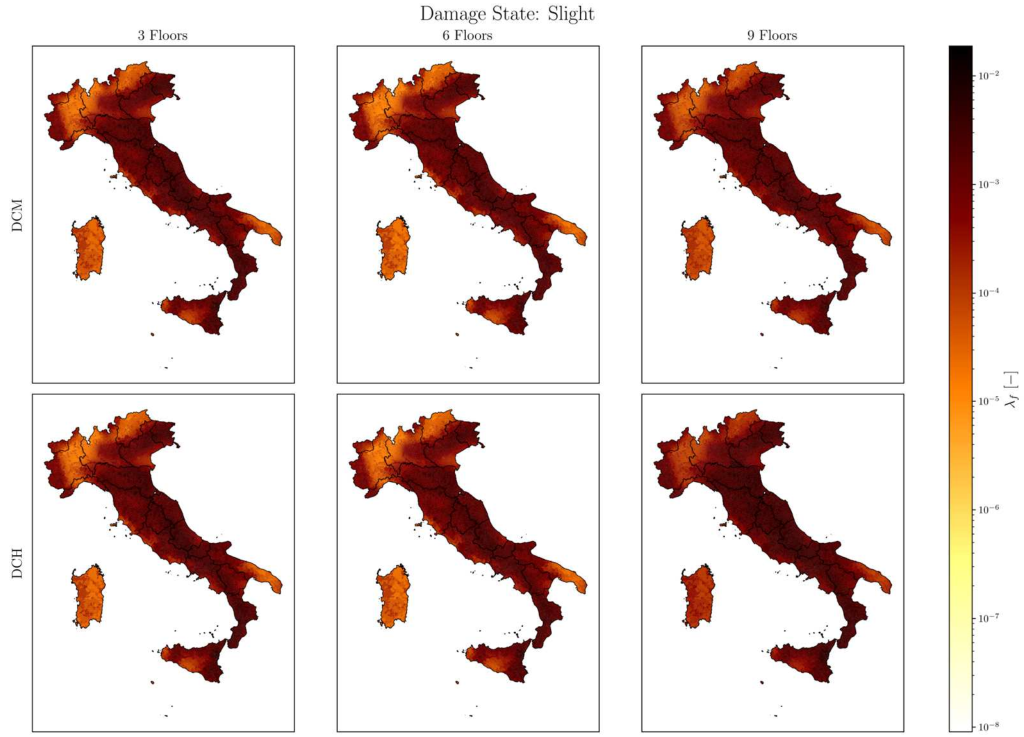

Figure 2-20 Reliability Maps- Bare Frames - SD

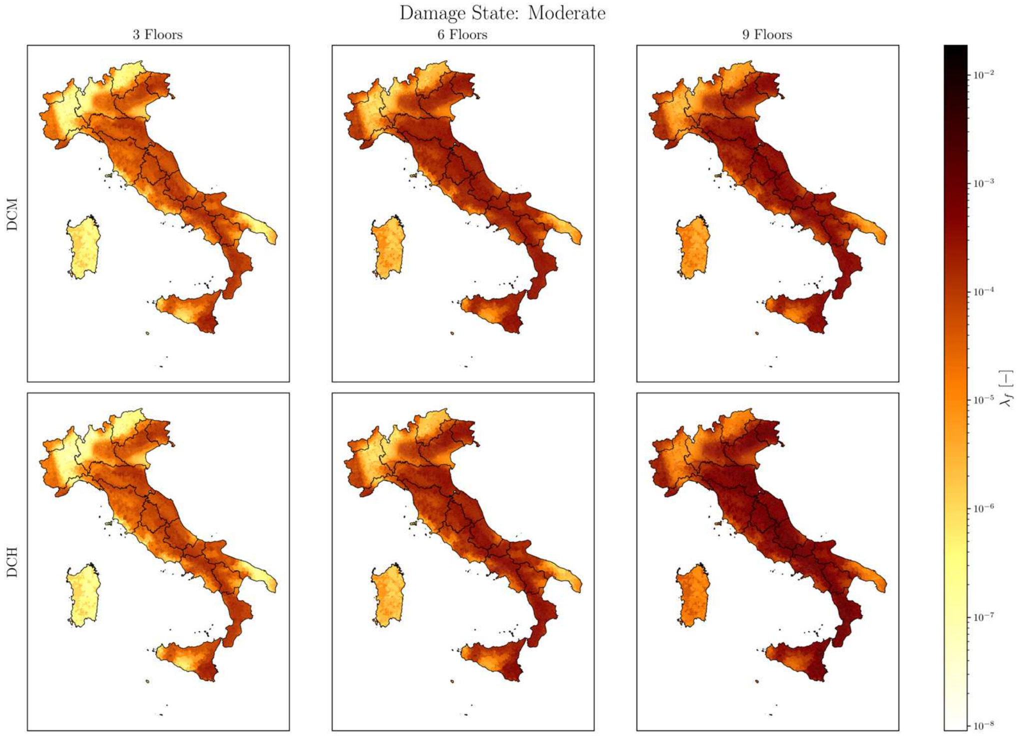

Figure 2-21 Reliability Maps - Bare Frames - MD

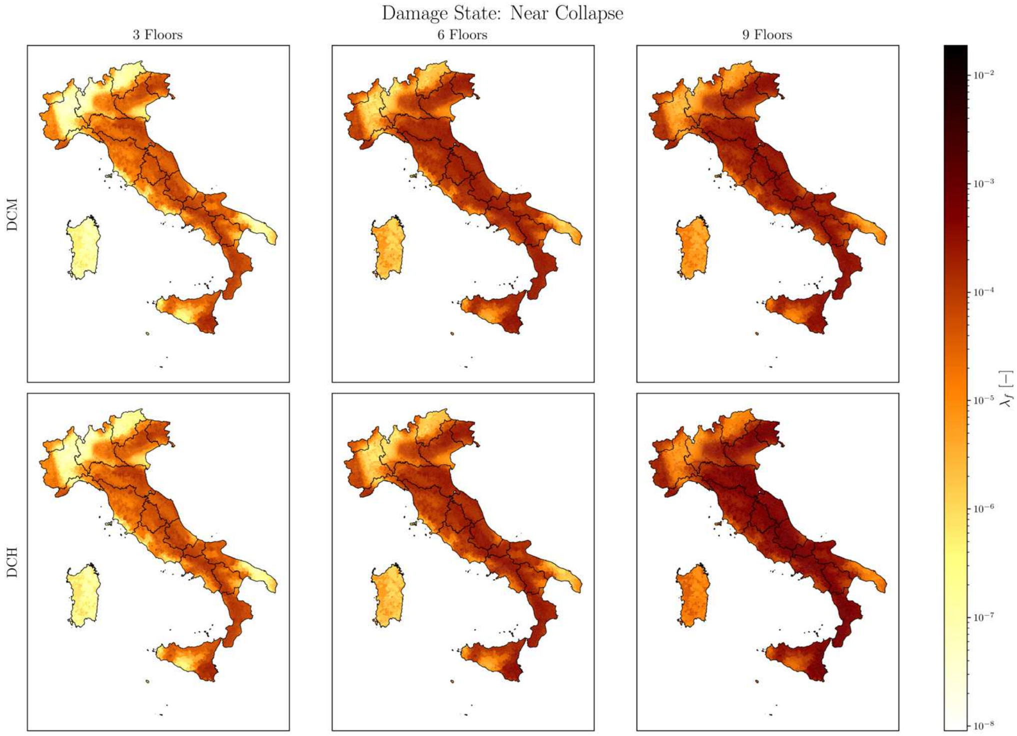

Figure 2-22 Reliability Maps- Bare Frames - NC

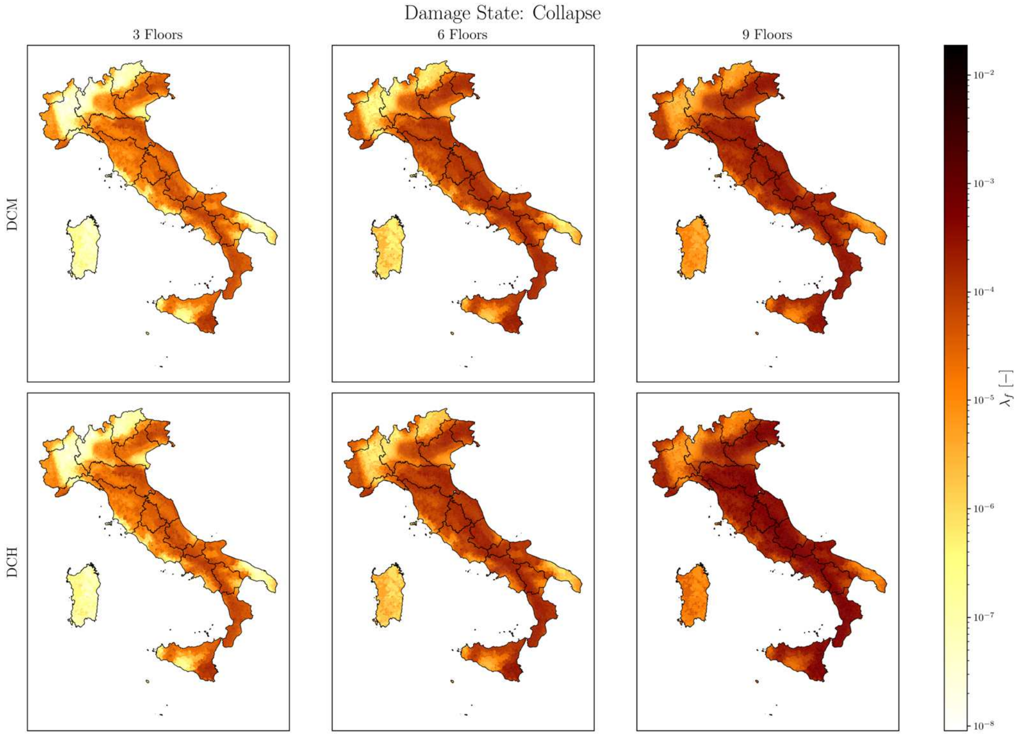

Figure 2-23 Reliability Maps – Bare Frames - C

Therefore, these outcomes have been grouped to develop seismic reliability maps, which are useful for depicting the distribution of failure rates along Italian territory. These results have been reported from Figure 2-20 to Figure 2-23 for each archetype configuration and damage state. The shades of the colours in the first map confirm the comparable results obtained through all the different layouts for the *slight* damage state. In contrast, the prevailing outcome of this analysis is outlined in the maps with respect to the remaining damage states. The dispersion of the colour map along the land enhances the non-uniform level of seismic reliability of code-compliant buildings. More in detail, failure rates appear to follow the pattern of the seismic hazard map, so the actual building code fails to ensure a uniform level of structural safety throughout the nation. In other words, the performance of code-compliant buildings is strictly dependent on the seismicity of the construction site. This *'hazard-targeted'* design is in contrast to the philosophy at the heart of the

Code, which should ensure the achievement of uniform safety for all buildings assigned a predefined class of importance.

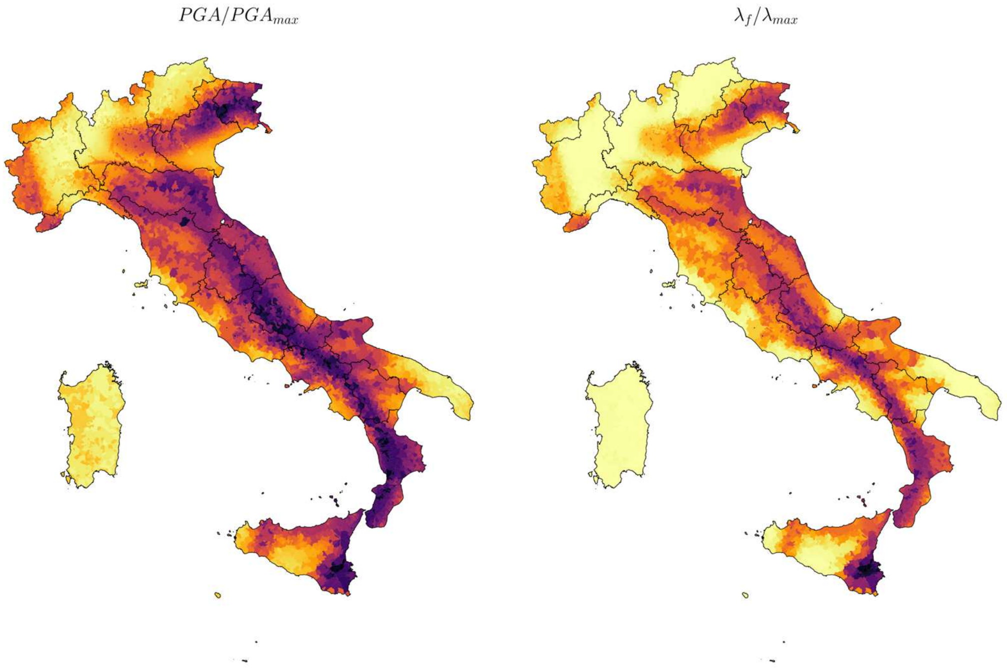

Figure 2-24 Comparison of normalized seismic hazard (on the left) and reliability maps (on the right)

The trend mentioned above could be better appreciated in Figure 2-24, where the seismic hazard map and the seismic reliability one have been compared for the case of DCM 6-storey in their *collapse* damage state, normalized to their maximum value. In this way, the figure clearly shows the correlation in terms of spatial distribution between the two quantities.

As a consequence, a regression analysis has been carried out on the failure rate data to establish a relationship between the seismic design action on the construction site and the achievable code-conforming seismic reliability. In this way, practitioners could use these laws to obtain a prior estimate of structural safety when designing a building following the current provisions. Hence, the laws have been formulated considering an intensity measure independent of the structural system, and specifically the peak ground acceleration PGA has been selected.

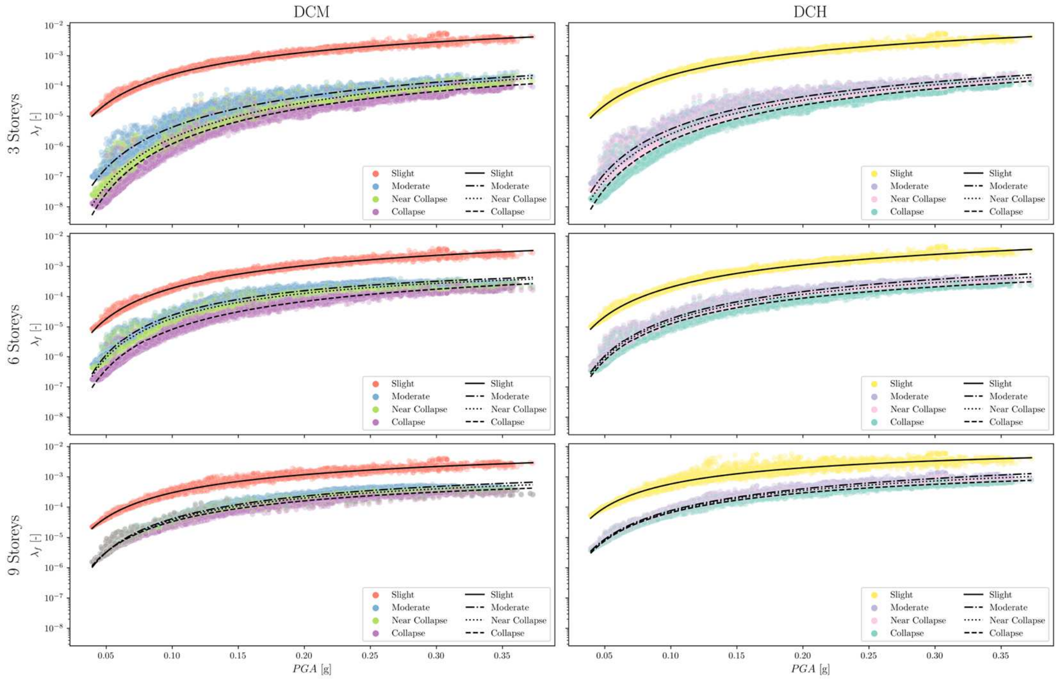

Figure 2-25 Regression laws for failure rates estimation – Bare Frames

Therefore, the mathematical expression of these laws has been formulated with a functional form similar to the one of the hazard curves, due to the related trend between failure rate and site seismicity observed from the seismic reliability analyses outcomes. Hence, after performing a series of tests to achieve a good level of statistical significance employing the parameter R^2, the subsequent formulation has been determined:

$$ln(\lambda_f) = k_0 \cdot e^{[k_1 \cdot ln(PGA) + \, k_2 ln^2(PGA)]} + \sigma\varepsilon \tag{2.9}$$

where the coefficients k_0, k_1, and k_2 are determined by minimising the interpolation error, the terms ε and σ refer to a normal random variable with zero mean and unitary dispersion, and the standard deviation of the model error, respectively.

The outcomes are reported in Figure 2-25 for each of the investigated building layouts and Table 2-4 illustrates the regression coefficients and the accuracy of the model through the standard deviation σ and the parameter R^2:

Table 2-4 Regression parameters – Bare Frames

Frame type	***DS***	k_0	k_1	k_2	**σ**	R^2
3-DCH-B	ds_1	-4.048	-0.293	0.010	0.124	0.994
	ds_2	-6.473	-0.241	0.020	0.337	0.981
	ds_3	-6.599	-0.246	0.019	0.369	0.979
	ds_4	-6.744	-0.257	0.018	0.413	0.976
3-DCM-B	ds_1	-4.105	-0.282	0.011	0.120	0.995
	ds_2	-6.541	-0.239	0.016	0.339	0.978
	ds_3	-6.439	-0.282	0.013	0.408	0.976
	ds_4	-6.973	-0.243	0.021	0.451	0.972
6-DCH-B	ds_1	-4.229	-0.275	0.012	0.122	0.994
	ds_2	-5.964	-0.203	0.025	0.207	0.990
	ds_3	-6.324	-0.175	0.029	0.220	0.988
	ds_4	-6.792	-0.143	0.034	0.245	0.984
6-DCM-B	ds_1	-4.392	-0.245	0.020	0.125	0.994
	ds_2	-7.031	-0.037	0.062	0.255	0.983
	ds_3	-6.995	-0.067	0.054	0.257	0.983
	ds_4	-6.826	-0.155	0.035	0.287	0.982
9-DCH-B	ds_1	-4.707	-0.113	0.037	0.128	0.974
	ds_2	-5.299	-0.217	0.015	0.181	0.994
	ds_3	-5.684	-0.171	0.023	0.170	0.994
	ds_4	-6.208	-0.114	0.033	0.172	0.993
9-DCM-B	ds_1	-4.838	-0.164	0.026	0.122	0.991
	ds_2	-6.297	-0.112	0.040	0.207	0.989
	ds_3	-6.543	-0.100	0.040	0.220	0.990
	ds_4	-6.860	-0.088	0.039	0.245	0.988

3 SEISMIC RELIABILITY OF CODE-CONFORMING RC INFILLED FRAME BUILDINGS

The previous Chapter developed a methodology capable of assessing the seismic reliability maps of code-compliant reinforced concrete bare frames. In this way, the effect of design prescriptions on the resultant seismic structural performance was highlighted. As a consequence, this Chapter proposes to apply the framework previously defined to the cases of infilled reinforced concrete frames. Therefore, it would be possible to evaluate how the presence of the infill panels affects the final seismic reliability of the compliant building.

3.1 CASE-STUDY BUILDINGS

The archetype buildings of the investigated infilled frames present the same topology layouts as the bare cases previously defined, as outlined in Figure 3-1. Thus, this Section outlines only the essential features of the buildings, while the extended description is reported in Section 2.1.

The investigated buildings are characterised by a rectangular plan with three and five bays of 5 metres in length each, in the two horizontal directions. A total of three different levels of floor layouts (i.e. three, six, and nine) were analysed. The prototype buildings were meant to be representative of residential buildings; therefore, the typical construction techniques of this structural typology were adopted. To this end, traditional infill panels made of clay bricks and built in accordance with the surrounding structural elements are considered.

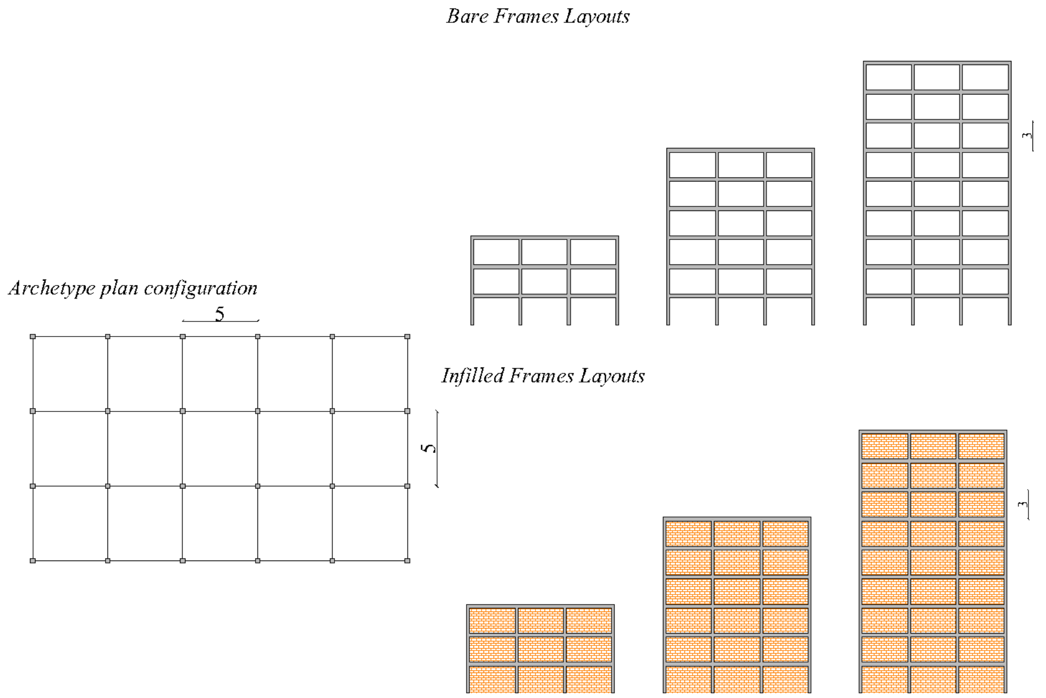

Figure 3-1 Bare and Infilled Archetypes

Furthermore, concrete and steel with the same mechanical properties as the bare frame cases have been used, as outlined in Table 3-1 and Table 3-2. In addition, the main properties of the masonry infills are resumed in Table 3-3 since they will be necessary for the assembling of the nonlinear models. These values have been selected in agreement with the one classified in the literature as medium-strong type [68, 69] to be consistent with those adopted in common practice.

Table 3-1 Mechanical properties of concrete C25/30

f_{ck} *[MPa]*	R_{ck} *[MPa]*	E_{cm} *[MPa]*	f_{cd} *[MPa]*
25.00	*30.00*	*31475.81*	*14.17*

Table 3-2 Mechanical properties of reinforcing steel B450C

f_{yk} [MPa]	E_s [MPa]	f_{yd} [MPa]
450.00	206000.00	391.30

Table 3-3 Mechanical properties of masonry infills

f_{wh} [MPa]	f_{wv} [MPa]	f_{wu} [MPa]	f_{ws} [MPa]	E_{wh} [MPa]	E_{ws} [MPa]	G [MPa]	W [kN/m^3]
1.50	3.51	0.30	0.36	1050.0	3240.0	1296.0	7.36

3.2 SEISMIC DESIGN PROCEDURE

This step consists of code-compliant sizing of prototype buildings according to the provisions of the current Italian Building Code [3], based on the principles of the *capacity-design* with two different ductility classes, namely the medium ductility class *DCM* and the high one *DCH*.

According to the current Code provisions, the infill walls are treated as nonstructural elements, thus it is not mandatory to explicitly account for their contribution to the overall seismic behaviour of the analysed buildings. Therefore, in common design practise, they are only modelled in terms of the masses and vertical load acting on the perimeter beams and neglecting any interaction with the structural elements of the frames. As a consequence, there is no difference in terms of sized section and reinforcement ratio between code-compliant infilled and bare frames. In other words, the design procedure fully described in Section 4.2 is identically replicated for the infilled frames, and the same design outcomes are adopted as starting data for assembling the nonlinear models.

3.3 SEISMIC VULNERABILITY ASSESSMENT

Once the design process has been completed, the infilled frames must be evaluated to derive the fragility parameters, and this is achieved by implementing a parametric algorithm that follows the main path reported in Section 2.3 and outlined in Figure 2-4.

Based on the outcomes of the parametric design, the explicit modelling strategy of the infill panels has to be established to account for their role in the global response of the buildings. The impact of infill walls on the seismic behaviour of RC frames has been widely demonstrated in the literature through experimental and numerical investigations [70, 71]. In this regard, recent earthquake events showed extensive damage to the infills not only for gravity-designed frames, but also for newly designed ones, and this led to costly repairs [72]. Therefore, this implies that a more refined consideration of nonstructural elements should be included in the Codes provisions, which confirms the need to account for the interaction between the frame and the masonry walls in terms when assessing the seismic performance.

Infills could be schematised, in a macro-modelling approach [73], through diagonal compressive struts, which increase the global lateral stiffness and induce additional lateral forces on the surrounding columns. The latter effect is herein neglected, since the principles of *capacity-design* aim at preventing the occurrence of brittle failures to ensure the achievement of ductile behaviour. In light of this, the modelling strategy based on a *single-strut* element has been preferred to the *multiple-strut* one, in order to properly address the scope of the investigation without spreading the computational effort. A wide range of studies provide relationships to properly characterise the equivalent strut in terms of both geometrical characteristics and *stress-strain* behaviour [74, 75]. More in detail, the width of the strut b_w has been calibrated with the model [75]:

$$b_w = \left(\frac{K_1}{\lambda h} + K_2\right) d_w \tag{3.1}$$

where d_w is the diagonal length of the panel, while the terms K_1 and K_2 are defined as a function of the value assumed by the nondimensional parameter λh, which is obtained from the relationship reported in [76]:

$$\lambda h = \sqrt[4]{\frac{E_{w\theta} \cdot t_w \cdot sin2\theta}{4 \cdot E_c \cdot I_c \cdot h_w}} h \tag{3.2}$$

where the terms h_w and t_w stand for the height and the thickness of the panel, respectively. E_c is the elastic modulus of the concrete and I_c is the moment of inertia of the adjacent columns. Additionally, θ is the angle of the diagonal strut relative to the horizontal direction and $E_{w\theta}$ is the elastic modulus of the masonry in the inclined direction. Referring to mechanical characteristics, the resistance of the strut is defined as the minimum value assumed by four different possible failure mechanisms, namely the compression failure at the centre σ_{wcc}, compression failure at the corners σ_{wccorn}, sliding shear failure σ_{wss}, and diagonal cracking σ_{wsd}:

$$\sigma_{wcc} = \frac{1.16 f_{vert} tan\theta}{K_1 + K_2 \lambda h} \tag{3.3}$$

$$\sigma_{wccorn} = \frac{1.2 f_{vert} sin\theta cos\theta}{K_1 (\lambda h)^{-0.12} + K_2 (\lambda h)^{0.88}} \tag{3.4}$$

$$\sigma_{wss} = \frac{(1.2 sin\theta + 0.45 cos\theta) f_{v0} + 0.3 \sigma_v}{b_w / d_w} \tag{3.5}$$

$$\sigma_{wsd} = \frac{0.6 f_t + 0.3 \sigma_v}{b_w / d_w} \tag{3.6}$$

where f_{vert} is the vertical compression strength of the panel, f_{v0} is the resistance of the mortar joint to the sliding effect, σ_v is the acting vertical stress due to gravity loads, and f_t is the shear resistance under diagonal compression.

The lateral force-displacement (or axial stress-strain) behaviour is commonly described with a trilinear relationship. Specifically, the first elastic branch spans up to the attainment of 80% of the maximum force; then a change in stiffness appears due to the complete cracking of the section, and it continues up to the maximum force. The third phase presents a degrading in force until the residual strength is reached, and then the backbone continues horizontally. In the present study, the crucial points to characterise this behaviour are defined according to the calibrated values of the fragility function in [77].

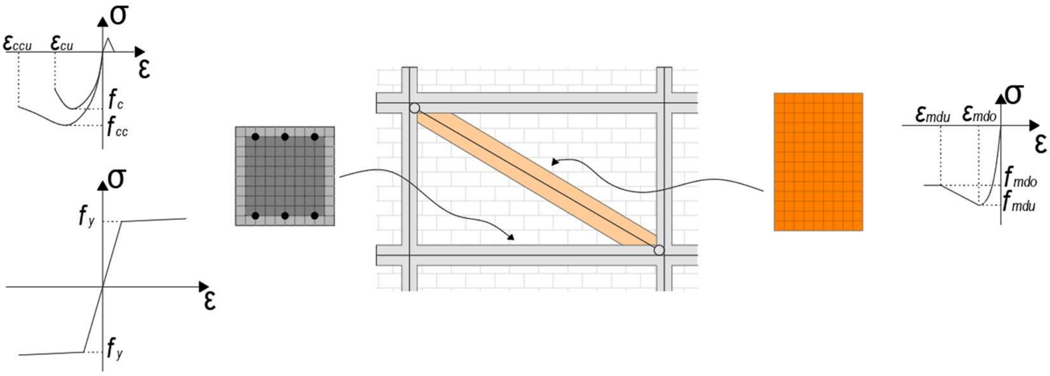

Figure 3-2 Nonlinear modelling techniques of infilled frames

In light of this, the numerical models are assembled in OpenSees using mono-dimensional frame elements with distributed plasticity. In this way, the nonlinearity is introduced in the model by the actual constitutive laws of the materials. Specifically, the infill struts are modelled with *pinned* elements characterised by the *Hysteretic* material of the OpenSees library, aimed at recreating the trilinear behaviour previously described. On the other hand, beams and columns sections are modelled with their proper dimensions and materials, as reported in detail in Section 2.3. Subsequently, nonlinear static analyses are carried out to obtain the capacity curves of the infilled frames for all geometrical layouts and to consider all the levels of the elastic spectral acceleration, and they are reported from Figure 3-3 to Figure 3-5.

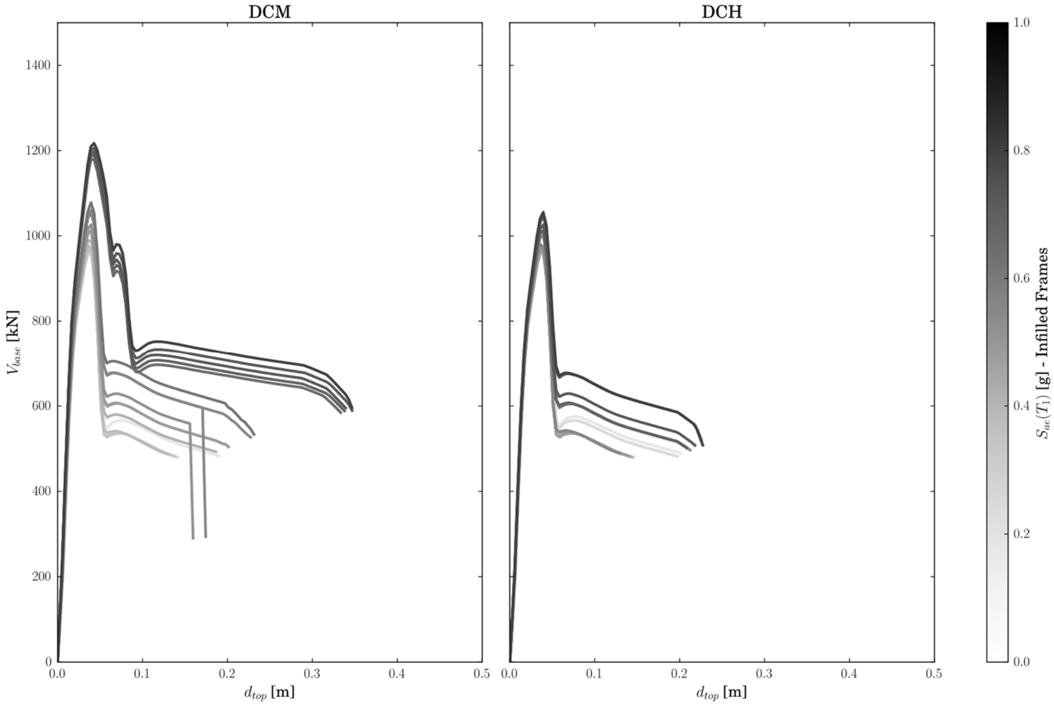

Figure 3-3 Pushover curves of code-compliant infilled frames - 3storeys

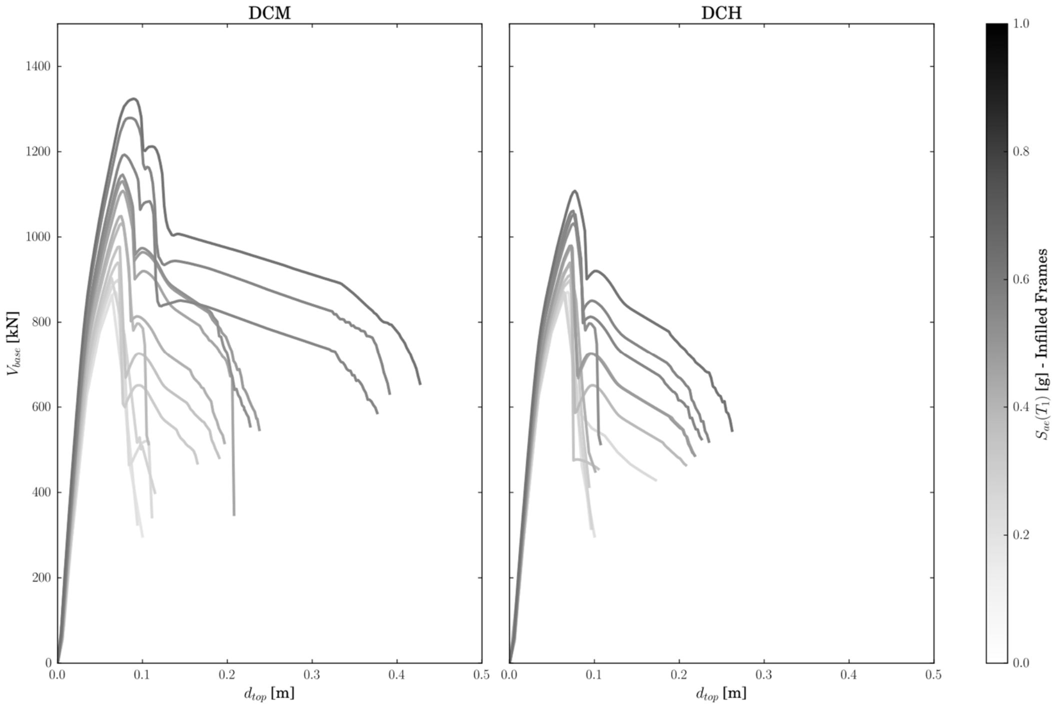

Figure 3-4 Pushover curves of code-compliant infilled frames – 6 storeys

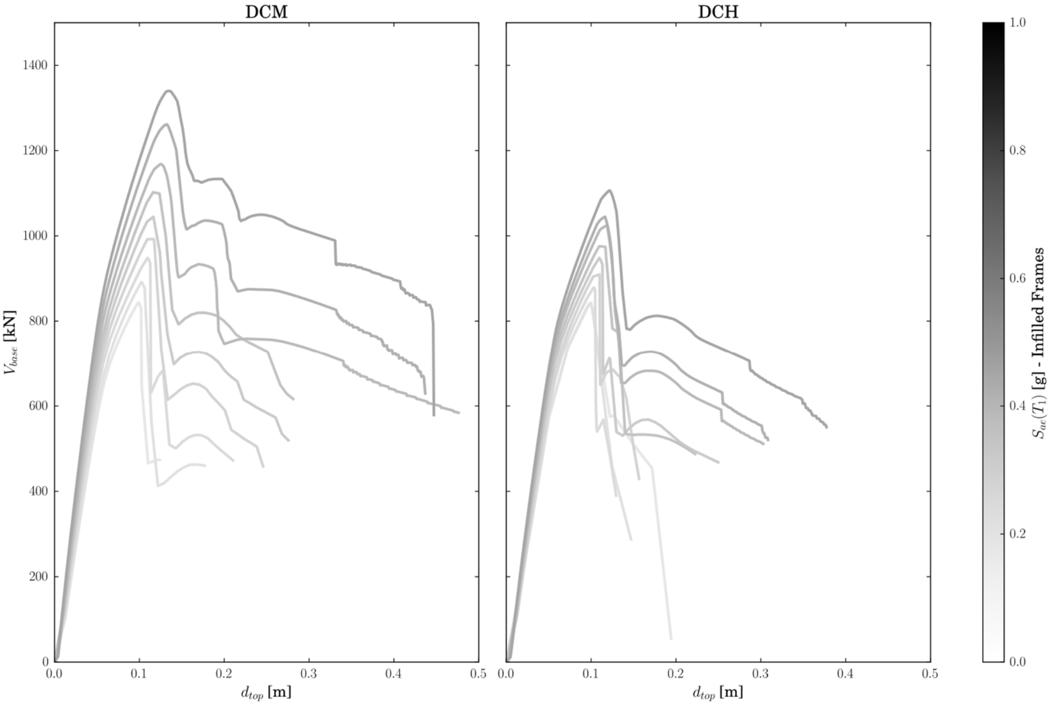

Figure 3-5 Pushover curves of code-compliant infilled frames – 9 storeys

First, the capacity curves highlight the global stiffening effect due to the presence of diagonal struts, since there is a steep drop immediately after attainment of the maximum base shear. For instance, in 3-storey frames, this force reduction is close to 50%, whereas it moderates when the number of floors increases. This effect could be ascribed to the higher presence of structural elements that enables a better force distribution in the structures. In addition, the capacity curves of the bare frames showed that the 9-storey cases are capable of attaining a maximum base shear greater than the 3-storey one, see Figure 2-7 and Figure 2-5, respectively. This implies that when the total cracking condition in the infill panels is achieved and the structure begins to behave as a bare frame, the 9-storey configuration is capable of sustaining a higher level of lateral force than the 3-storey configuration, and this delays the decrease of the base shear.

When comparing the results in terms of ductility class, the figures show a better performance of the DCM configurations in terms of base shear capacity. In this regard, the adoption of a higher design spectral acceleration due to a lower behaviour factor in DCM leads to frames with sections of greater size that reflect on an enhancement of the maximum base shear achievable. On the other hand, there is no significant difference in terms of ultimate displacement between the two ductility classes. On the contrary, this behaviour differs with the varying of the storeys. Hence, performance improves according to the number of storeys due to the greater flexibility of taller buildings.

In summary, the pushover results revealed a significantly reduced ductile behaviour of infilled frames when compared to the bare layouts, with an improvement of global lateral stiffness that strongly increases their maximum base shear.

Thereafter, a multi-linearised envelope is applied to the pushover curves to carry out a conversion from the MDOF system to an equivalent SDOF, which will be used to perform the non-linear dynamic analyses needed for the fragility assessment. This methodology is consistent with the approach adopted for the bare frames in Section 2.3. However, the different global trends of the capacity curves require a different linearisation process [78-80]. In detail, the base shear-displacement relationship could be subdivided into four branches. The first linear ascending one depicts the elastic phase of the frame; then a short horizontal part represents the yield of the system with low ductility due to the stiffening effects of the infills. The subsequent branch is ruled by the strength degradation of the system; thus, there is a global reduction of base shear, while the last part is characterised by total cracking of the infills, and the global behaviour is governed by the bare frame. Consequently, the main points of the backbone are estimated via the use of the principle of energy equivalency and by determining the maximum and minimum strength points, where the latter corresponds to the above-mentioned point of total failure of the infills. The multilinearised curve and the hysteretic behaviour of the SDOF are shown in Figure 3-6. The cyclic dynamic behaviour herein obtained is in good agreement with the one adopted in the study by Suzuki and Iervolino[59], which aimed to assess the seismic fragility of Italian buildings using the SDOF approximation.

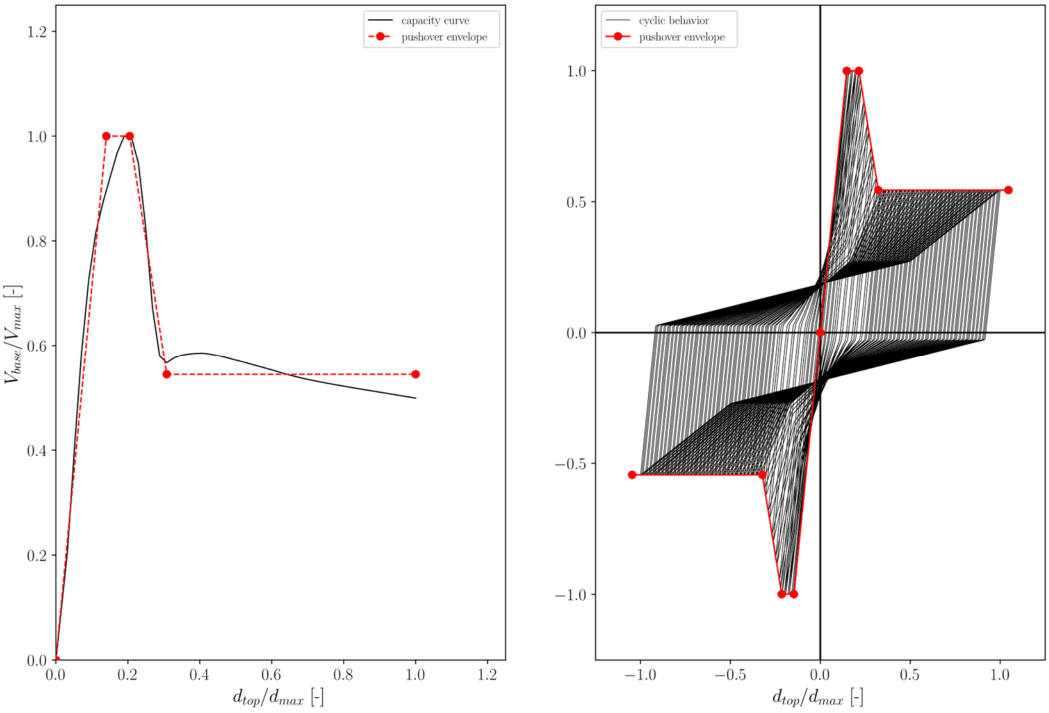

Figure 3-6 Backbone and Hysteretic Behaviour of SDOF – Infilled Frames

At this point, the fragility parameters have been derived using the same extended approach described in Section 2.3. Namely, the same dataset of ground motions has been selected and the same criterion has been applied to define the damage state points. For this reason, the results of the vulnerability assessment are directly presented in the following figures. First of all, Figure 3-7 highlights a clear scattered behaviour between the median values of the *collapse* damage state and the other, for all the investigated configurations. These outcomes should be ascribed to the less ductile behaviour of the frames detected in pushover analyses, which causes close displacement thresholds. Furthermore, there is a slight link between the median intensity and the elastic spectral acceleration values, which denotes a decrease in seismic vulnerability when adopting higher seismic design actions. As outlined for the bare frames, the fragility values exhibit an inverse trend with the number of storeys, whereas no significant discrepancies are reported in terms of ductility classes.

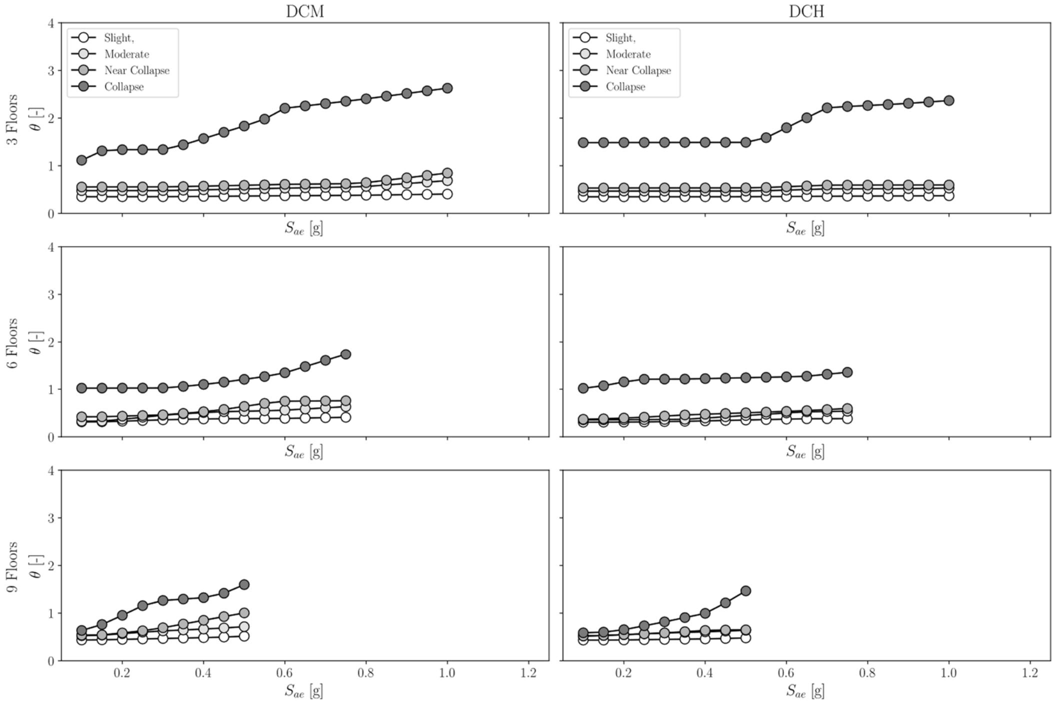

Figure 3-7 Correlation between the median parameter θ and the spectral acceleration S_{ae}

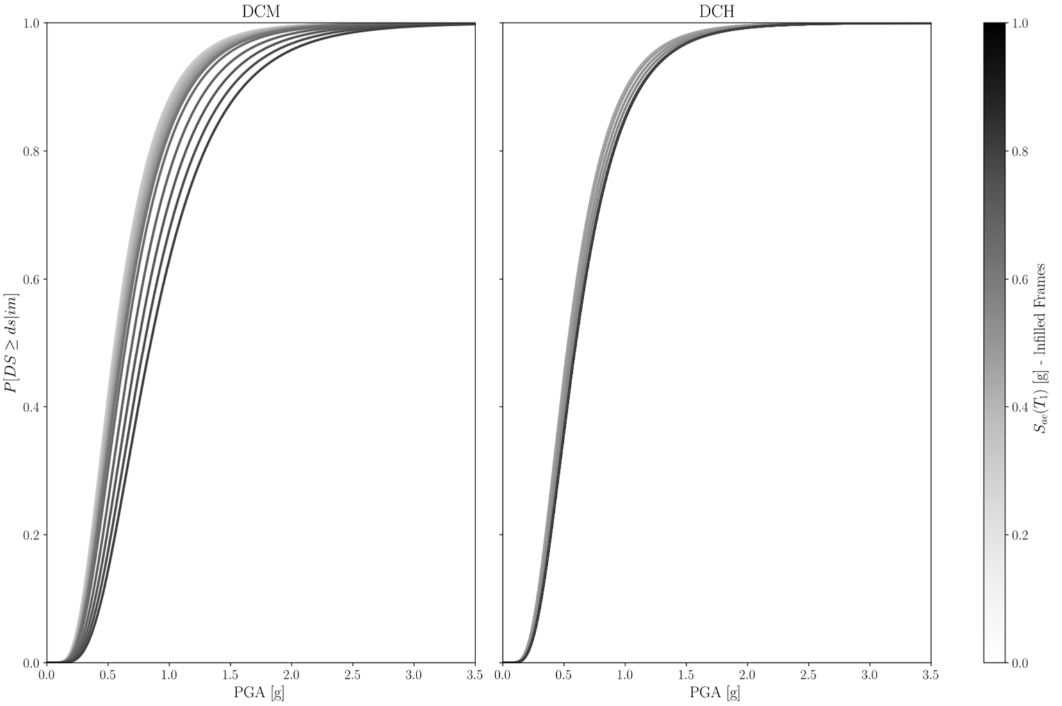

Figure 3-8 Fragility curves code-compliant infilled frames – 3 storeys - NC

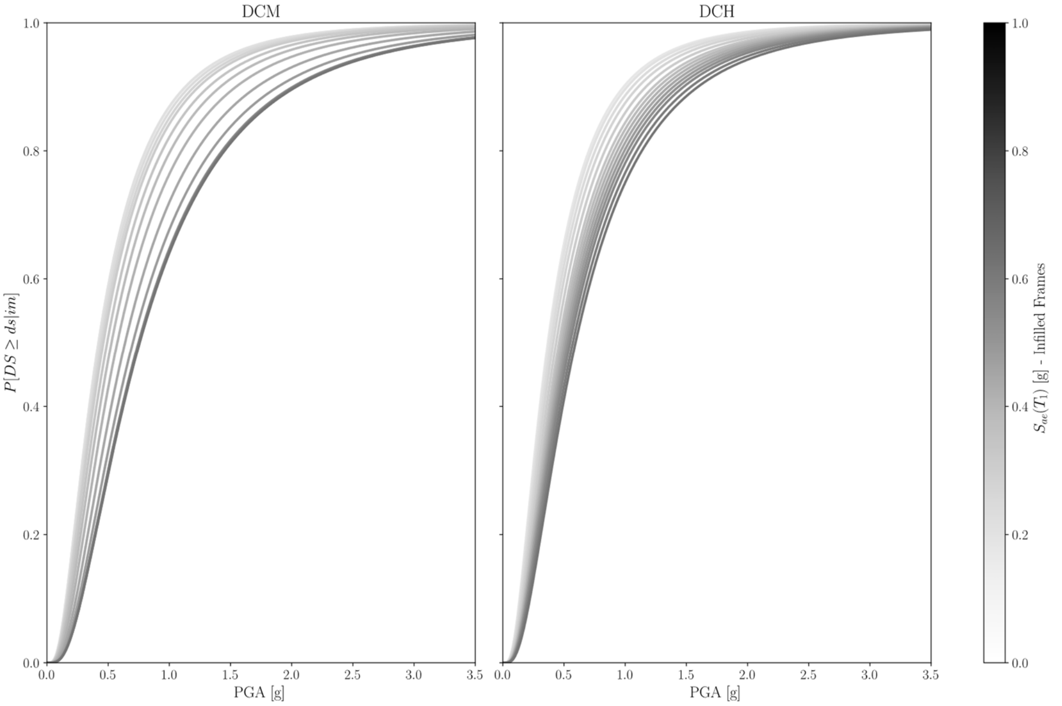

Figure 3-9 Fragility curves code-compliant infilled frames – 6 storeys - NC

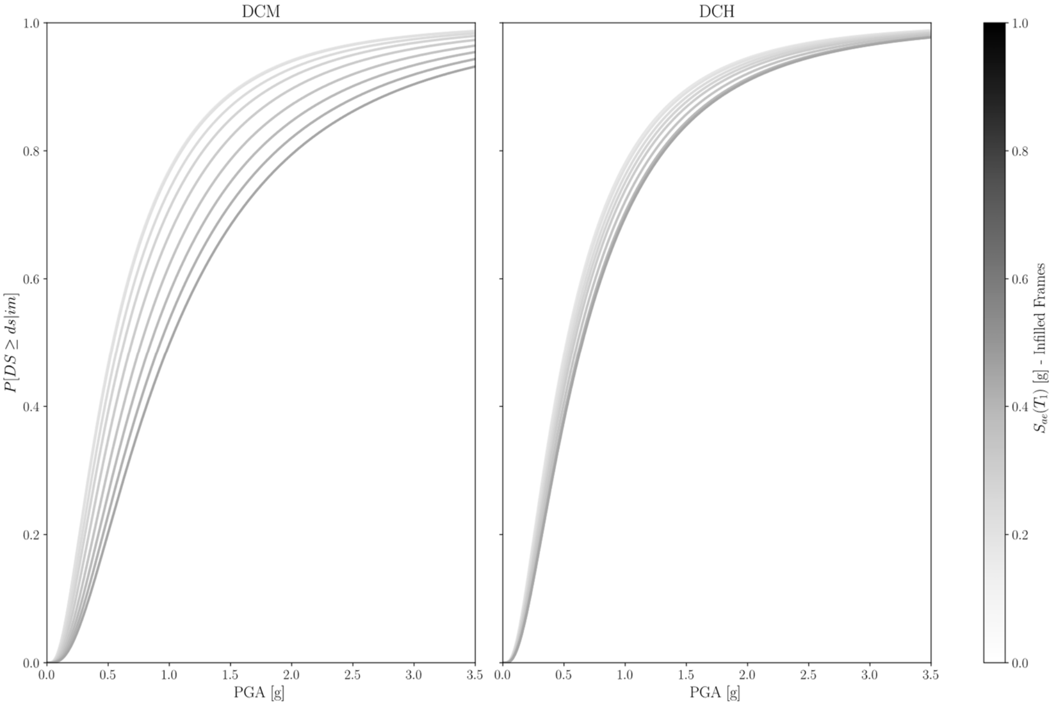

Figure 3-10 Fragility curves code-compliant infilled frames – 9 storeys - NC

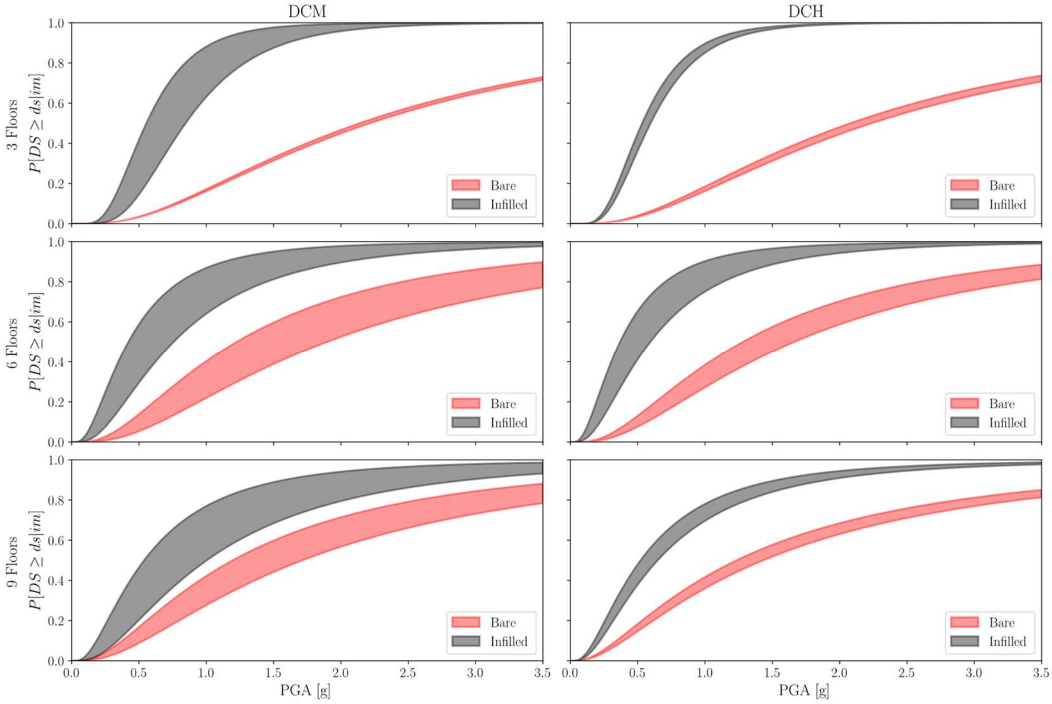

Figure 3-11 Fragility Curves NC: Bare vs Infilled

The fragility curves are presented from Figure 3-8 to Figure 3-10 from the third damage state, i.e. *near collapse*. These figures emphasise the observations deduced from Figure 3-7. The almost steady trend of the median values for the 3-storey layouts leads to a strict bundle of curves, while for the other storeys, the increasing trend of the median according to the elastic spectral acceleration results in a wider scatter of the fragilities. Thereafter, these results have been compared to those obtained for the bare frames in order to detect how the stiffening of the infills affects the vulnerability. Hence, Figure 3-11 compares the regions of minimum and maximum fragility between the bare and infilled layouts, referring to the *near collapse* damage state; thus, the greater vulnerability of the second case is highlighted.

3.4 SEISMIC RELIABILITY MAPS

The final step of this framework consists of determining the seismic failure rates through the Italian territory, and it has been described in detail in Section 2.4; hence it will only be briefly described hereafter, so as to focus more on the obtained results. The fragility parameters of the infilled frames are ideally associated with each Italian municipality by matching the elastic spectral acceleration S_{ae}, which simulates the application of the design process at the site of interest. Then, the specific hazard curve expressed in terms of PGA is computed by enveloping the values at nine return periods. In this way, the fragility curve and the derivative of the hazard one are coupled together to numerically solve the integral expressed in Equation (1.4), and in this way it is possible to obtain the seismic failure rates. The results are preliminary presented employing the boxplot elements (Figure 3-12) and are summarised in terms of minimum, maximum and mean values.

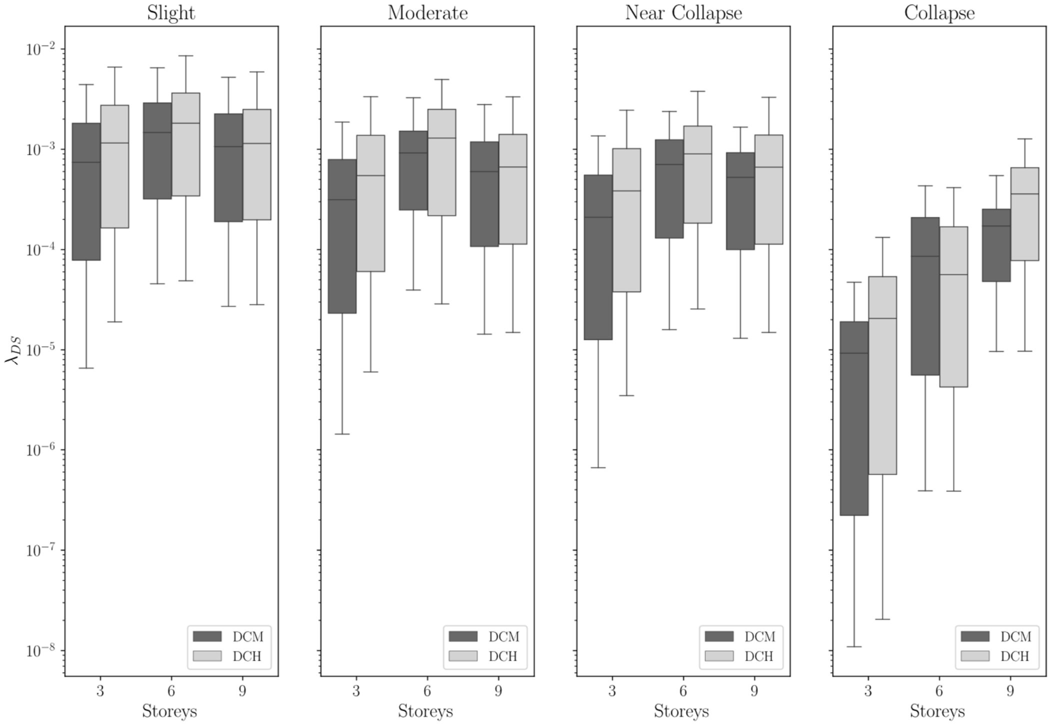

Figure 3-12 Seismic failure rates boxplot – Infilled frames

Figure 3-12 shows a marked reliability difference in the results of the *collapse* damage state. In this case, there is an opposite trend between seismic safety and the number of floors in the buildings, since the 9-storey frames report higher failure rates than the 3-storey. However, the position of the median marker is indicative of a skewed distribution, with most of the values located at the upper limit. Namely, the minimum values span from $2.05 \cdot 10^{-8}$ and $9.69 \cdot 10^{-6}$ for the 3- and 9-storey, respectively. Hence, a range of variation of two orders of magnitude is observed. On the contrary, the maxima start from $1.74 \cdot 10^{-4}$ and reach a value of $5.47 \cdot 10^{-4}$, thus there is no remarkable discrepancy.

Table 3-4 Summary of failure rates – Infilled Frames

Case	**Damage State**	λ_f *Min*	*Max*	*Mean*
3 -DCH	*ds_1 (SD)*	1.90E-05	8.99E-03	1.61E-03
	ds_2 (MD)	5.96E-06	3.84E-03	7.75E-04
	ds_3 (NC)	3.46E-06	2.64E-03	5.62E-04
	ds_4 (C)	2.05E-08	1.73E-04	2.90E-05
3 -DCM	*ds_1 (SD)*	6.49E-06	5.80E-03	1.07E-03
	ds_2 (MD)	1.43E-06	1.87E-03	4.55E-04
	ds_3 (NC)	6.63E-07	1.36E-03	3.22E-04
	ds_4 (C)	1.09E-08	1.13E-04	1.22E-05
6 -DCH	*ds_1 (SD)*	4.88E-05	9.44E-03	2.12E-03
	ds_2 (MD)	2.87E-05	4.97E-03	1.40E-03
	ds_3 (NC)	2.56E-05	4.11E-03	1.02E-03
	ds_4 (C)	3.87E-07	4.94E-04	1.00E-04
6 -DCM	*ds_1 (SD)*	4.56E-05	8.51E-03	1.77E-03
	ds_2 (MD)	3.95E-05	3.69E-03	9.63E-04
	ds_3 (NC)	1.59E-05	2.38E-03	7.35E-04
	ds_4 (C)	3.90E-07	4.32E-04	1.17E-04
9 -DCH	*ds_1 (SD)*	2.82E-05	7.09E-03	1.46E-03
	ds_2 (MD)	1.49E-05	3.77E-03	8.33E-04
	ds_3 (NC)	1.49E-05	3.61E-03	8.06E-04
	ds_4 (C)	9.69E-06	1.27E-03	3.82E-04
9 -DCM	*ds_1 (SD)*	2.71E-05	6.20E-03	1.32E-03
	ds_2 (MD)	1.44E-05	2.97E-03	7.06E-04
	ds_3 (NC)	1.30E-05	1.66E-03	5.37E-04
	ds_4 (C)	9.65E-06	5.47E-04	1.67E-04

Moving to the other states of damage, it is not possible to identify a similar trend, referring not to the variation in terms of floors or between the different damage states themselves. For instance, referring to the 6-storey DCH case, the median in the *slight* state of damage is $2.12 \cdot 10^{-3}$, while at the *near collapse* reaches $1.00 \cdot 10^{-3}$.

Consequently, the failure rates are plotted on a map, and their trend throughout the Italian territory is highlighted. Seismic reliability maps of code-compliant infilled frames are presented from Figure 3-13 to Figure 3-16 for each state of damage.

These maps point out a darker shade of colours compared to those obtained for the failure rates for every damage state. In particular, this effect is emphasised in the initial states of damage, while it eases in the *collapse*. This trend is consistent with the issues revealed in recent post-earthquake surveys: the presence of the infills detrimentally diminishes the performance of recently designed buildings for the so-called *serviceability* damage state. However, it should be underlined that the present study focused only on the stiffening effect due to explicit modelling of the masonry panels, while it does not investigate the impact of the additional shear forces induced from the infills to the adjacent members. Therefore, this aspect could affect the vulnerability in the ultimate damage state.

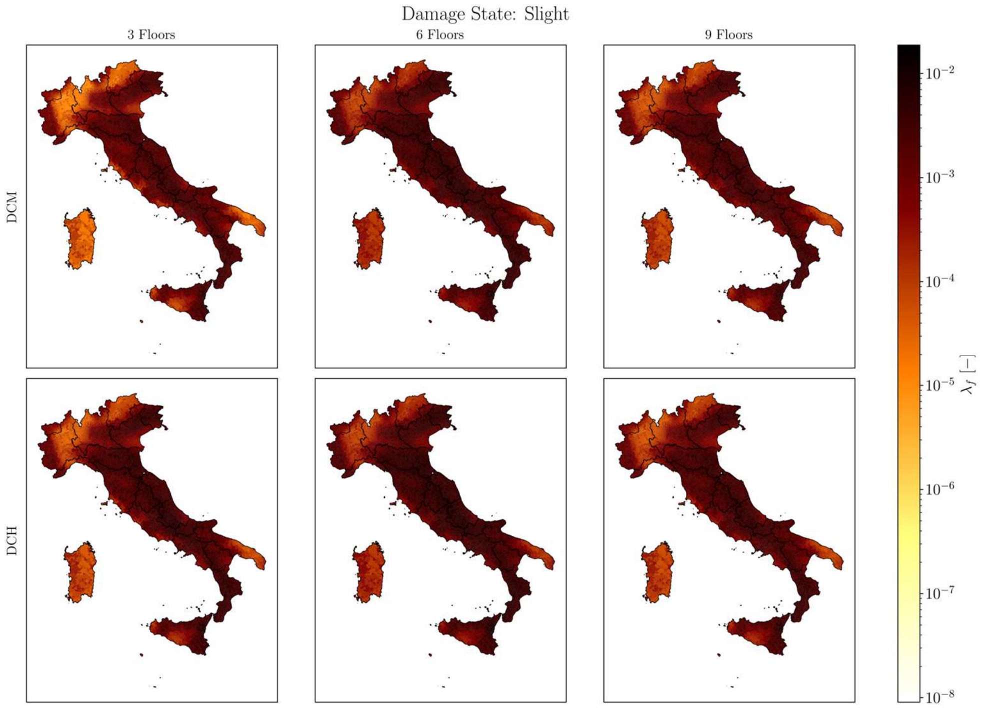

Figure 3-13 Reliability Maps - Infilled Frames – SD

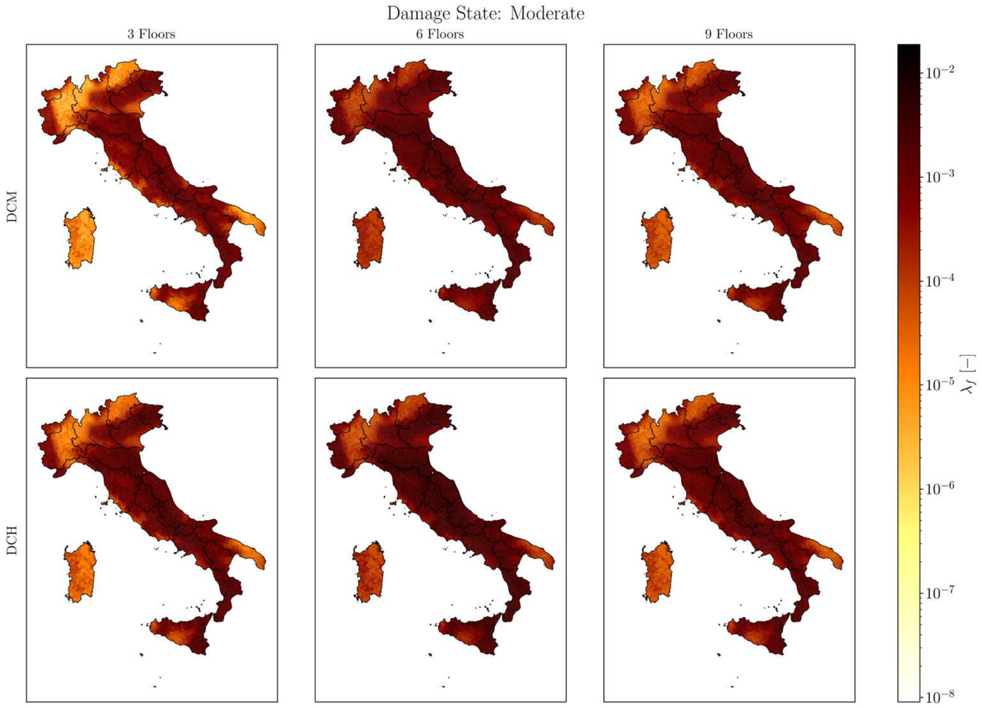

Figure 3-14 Reliability Maps - Infilled Frames – MD

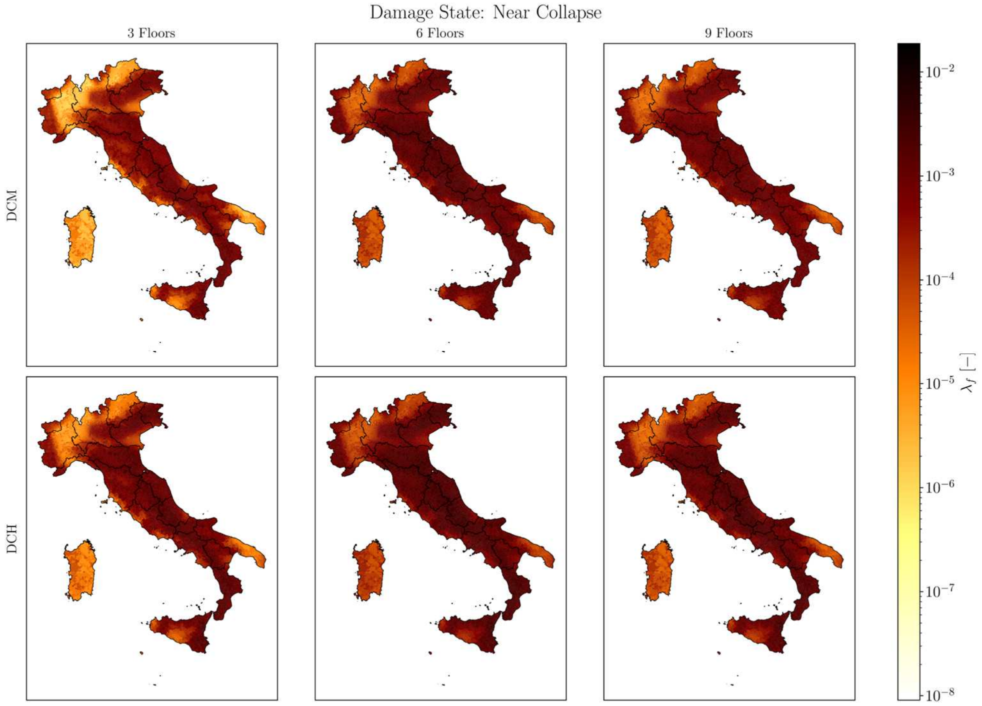

Figure 3-15 Reliability Maps - Infilled Frames – NC

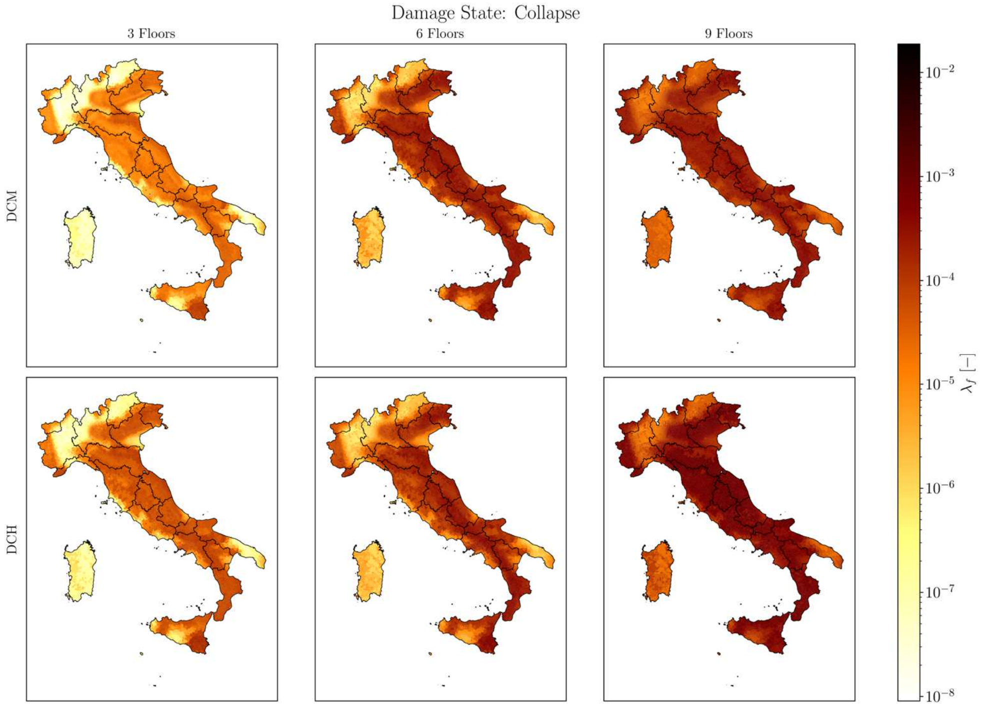

Figure 3-16 Reliability Maps - Infilled Frames – C

Finally, as for the bare configurations, a functional form has been determined to relate the seismic design action at a specific place, in terms of PGA, to the achievable code-compliant seismic failure rate. A mathematical expression with the same functional form of hazard curves, reported in Equation (2.9), has been employed for giving an exploratory appraisal of code-conforming failure rates, which could be adopted by structural designers in common applications. Hence, Figure 3-17 illustrates the outcomes of this regression analysis, whereas Table 3-5 proves the goodness of the statistical model.

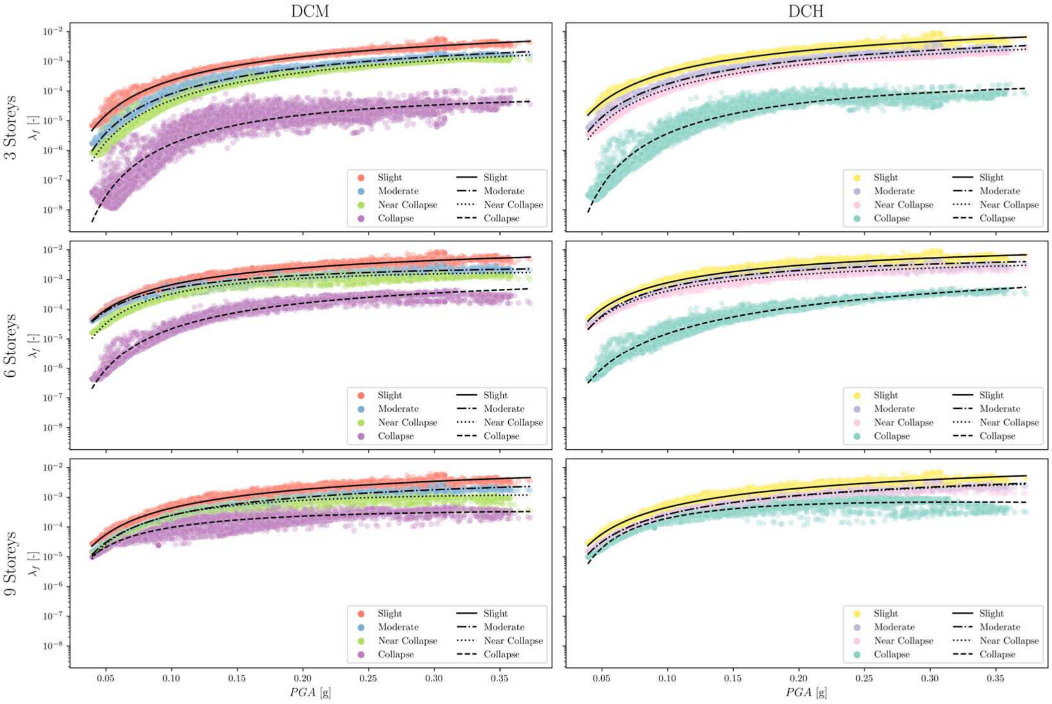

Figure 3-17 Regression laws for failure rates estimation – Infilled Frames

Table 3-5 Regression parameters – Infilled Frames

Frame type	***DS***	k_0	k_1	k_2	σ
3-DCH-B	ds_1	-3.793	-0.266	0.020	0.126
	ds_2	-4.449	-0.223	0.029	0.138
	ds_3	-4.684	-0.218	0.030	0.155
	ds_4	-8.426	0.009	0.079	0.515
3-DCM-B	ds_1	-4.104	-0.241	0.030	0.146
	ds_2	-4.925	-0.187	0.041	0.216
	ds_3	-5.063	-0.205	0.038	0.258
	ds_4	-9.765	0.055	0.082	0.745
6-DCH-B	ds_1	-4.219	-0.129	0.044	0.146
	ds_2	-5.115	-0.011	0.068	0.172
	ds_3	-5.258	-0.050	0.053	0.125
	ds_4	-5.739	-0.263	0.010	0.263
6-DCM-B	ds_1	-4.344	-0.142	0.037	0.126
	ds_2	-5.958	0.041	0.064	0.160
	ds_3	-6.611	0.128	0.092	0.191
	ds_4	-6.722	-0.073	0.057	0.287
9-DCH-B	ds_1	-4.163	-0.207	0.026	0.142
	ds_2	-4.867	-0.148	0.035	0.120
	ds_3	-5.045	-0.119	0.041	0.128
	ds_4	-8.350	0.247	0.112	0.261
9-DCM-B	ds_1	-4.394	-0.175	0.031	0.135
	ds_2	-5.290	-0.097	0.043	0.121
	ds_3	-7.085	0.142	0.092	0.204
	ds_4	-8.167	0.074	0.055	0.300

4 SEISMIC RELIABILITY OF CODE-CONFORMING RC SHEAR WALL BUILDINGS

In this chapter, the proposed framework for assessing seismic reliability of code-compliant buildings is applied to shear-wall buildings. First, the prototype structures will be designed according to Code provisions, and after that a series of non-linear dynamic analysis will be carried out to determine the vulnerability. The results of this step will be coupled with the risk term to obtain the final results of seismic failure rates.

4.1 CASE-STUDY BUILDINGS

Shear-wall (SW) reinforced concrete structures represent a widely adopted structural scheme for newly designed buildings. According to the current Italian Building Code [3], a reinforced concrete element is identified as a *seismic wall,* if its section has a slender rectangular shape and satisfies a slenderness ratio greater than four. Thus, an RC structure could be classified as SW-type when over 65% of the seismic action is absorbed by *seismic wall* elements that are dominated by a flexural behaviour.

As a result, the prototype buildings are rectangular symmetric-plan structures, with three bays of 5 m length each in one direction, and two spans of 6 m in the other. Shear-wall elements are placed in the exterior bays in order to maximise their lever arm. Four SWs with a length of 150 cm are positioned in one direction, while two elements are set in the perpendicular one. Additionally, the shear walls have a constant thickness of 25 cm. The investigated archetypes vary in height; namely, 2-, 4-, and 6-storey layouts have been considered, and they have a constant storey height of 3 m. These buildings are meant to be representative of common residential buildings; thus, typical construction technologies are assumed. Therefore, the inter-storey slabs are one-way type with a permanent load of 5.80 kN/m^2 and a live load of 2.00 kN/m^2, while at the roof the permanent load decreases to 5.00 kN/m^2. The minimum dimensions are assigned to beams and columns, since they have to carry out only gravitational load because it is assumed that the entire horizontal action is sustained by the slender walls. The main geometric features of the archetype buildings are outlined in Figure 4-1.

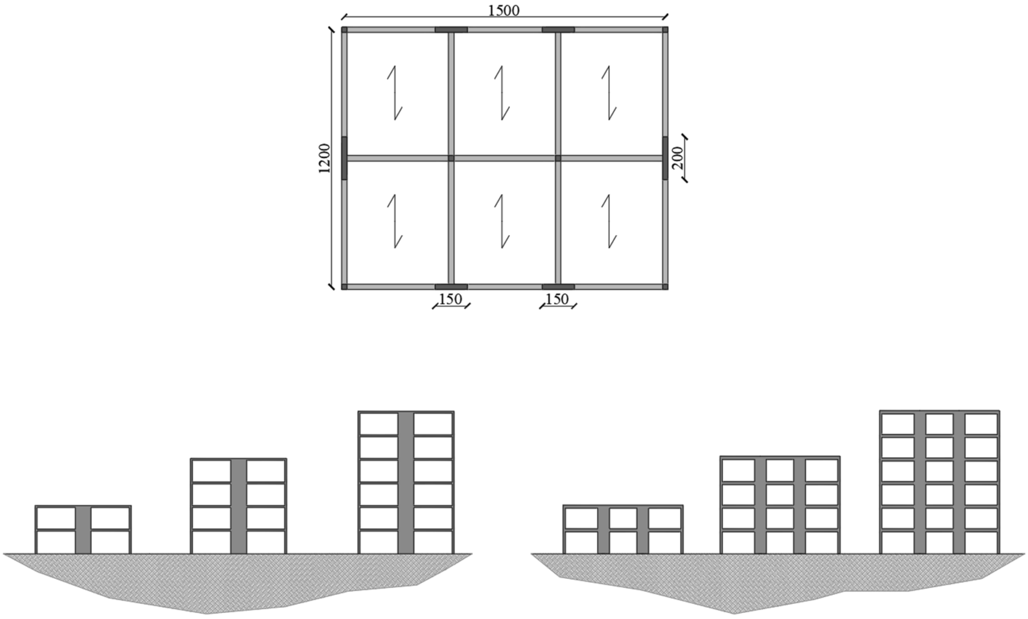

Figure 4-1 Layouts of the archetype SW buildings

Concrete C30/37 has been adopted for shear-wall elements, and steel □450C has been considered for reinforcements; thus, their main properties are summarised in Table 4-1 and in Table 4-2, respectively. The contribution of the foundation has been neglected, and thus the vertical elements have been considered fixed at the base.

Table 4-1 Mechanical properties of concrete C30/37

f_{ck} [MPa]	R_{ck} [MPa]	E_{cm} [MPa]	f_{cd} [MPa]
30.00	*37.00*	*32836.57*	*17.00*

Table 4-2 Mechanical properties of reinforcing steel B450C

f_{yk} [MPa]	E_s [MPa]	f_{yd} [MPa]
450.00	206000.00	391.30

4.2 SEISMIC DESIGN PROCEDURE

The design process has been performed following the prescriptions of the Italian Building Code [3], to simulate the common sizing practice adopted by designers to obtain code-compliant buildings.

As a consequence, seismic design loads are applied to the structures using the *equivalent lateral force (ELF)* method, which consists of a linear elastic analysis where the inherent nonlinear structural resources are taken into account through a force reduction coefficient q (i.e. behaviour factor), and its implementation is described in detail in Section 2.2. In this way, the seismic intensity is expressed in terms of elastic spectral acceleration $S_{ae}(T_1)$, which is derived from uniform hazard spectra (UHS). The design process is carried out for a range of spectral accelerations that cover all possible levels of intensity that could be applied to the investigated buildings. In detail, the spectral acceleration ranges up to an intensity of 0.85g, which is the maximum achievable in Italy considering a 475-year return period T_R, typical for residential buildings.

The sizing process is performed according to the *capacity-design* rules contained in the Code; thus, the structures are evaluated with the provisions of both the medium ductility class (DCM) and the high ductility class (DCH). In this regard, a behaviour factor equal to 3.0 is used for the DCM cases and a value of 4.0 for the DCH ones.

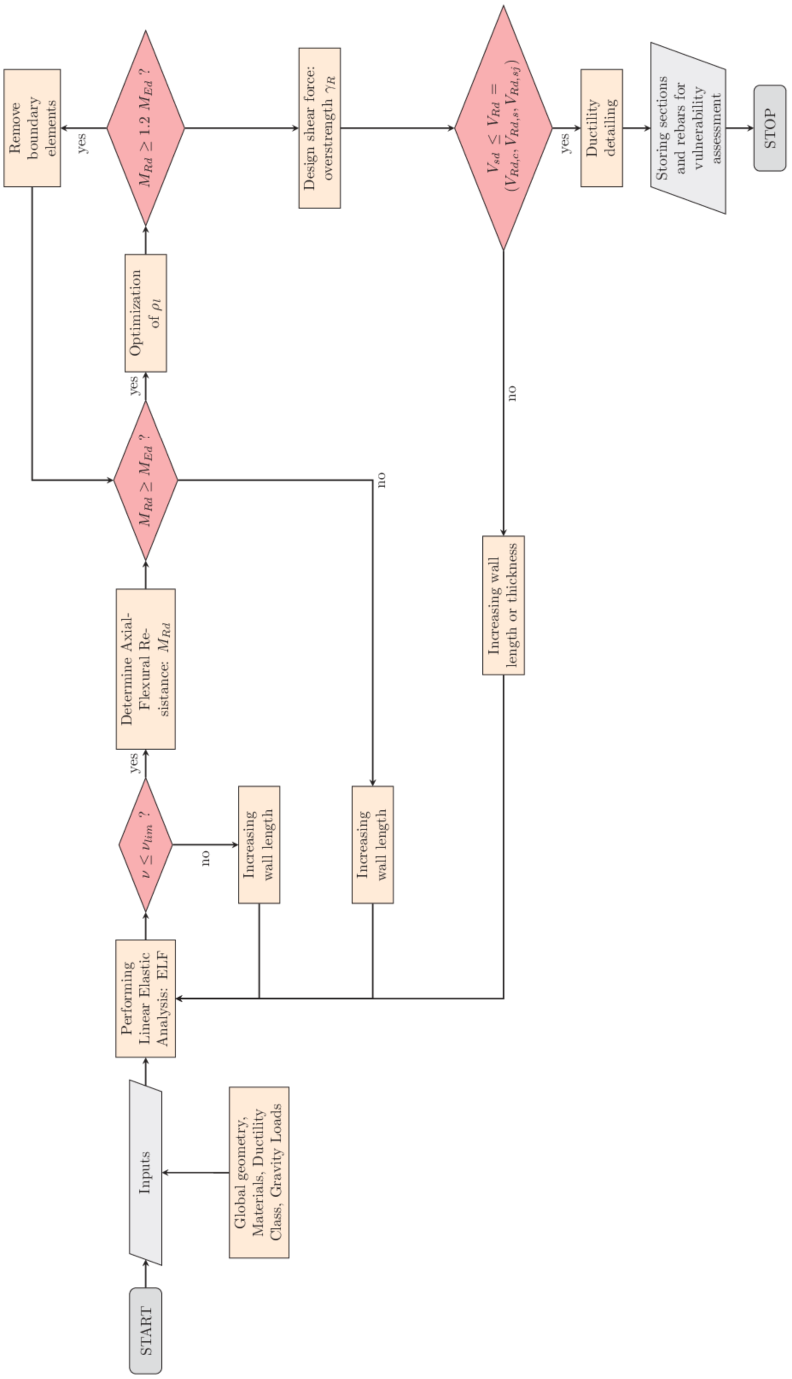

Figure 4-2 Flowchart for the seismic design of shear walls

The fulfilment of the requirements is achieved by implementing an iterative procedure (Figure 4-2) in the Matlab environment [53], starting from the general input data described in the previous section. Therefore, the first part of the workflow focusses on checking the flexural provisions. Thus, the resisting moment is evaluated by limiting the safety check between resistance (M_{Rd}) and solicitation (M_{Sd}) up to 20% and by considering a proper detailing of the boundary elements placed along the plastic hinge region at the base of the wall. In the event that the required longitudinal reinforcement ratio exceeds the upper limit, the wall section increases, and the process starts again from the calculation of the acting forces. In contrast, when a satisfactory flexural condition is met, it is possible to move to the transverse reinforcement detailing. To this end, the design shear force is computed by applying an amplification factor based on the previously determined flexural capacity, with the aim of avoiding the development of a brittle behaviour of the wall. Shear resistance must be tested against three possible mechanisms: concrete shear compression failure, horizontal shear tension failure, and sliding in the construction joint. In this way, the diameter and spacing of the transverse bars are defined, while the dimensions of the wall section could be increased when the shear compression check is not satisfied, causing the process to be re-start. The last step of the procedure involves the ductility checks in the base section of the wall, which is committed to the dissipation of seismic energy.

Finally, the design outcomes are properly stored in a series of matrices that will be used to assemble the nonlinear models to assess the seismic vulnerability.

4.3 SEISMIC VULNERABILITY ASSESSMENT

The main framework developed in Section 2.3 for the assessment of RC frames has been slightly modified to properly capture the response of the buildings on the shear walls.

Firstly, it has been necessary to find a suitable modelling strategy for shear wall elements in the OpenSees non-linear analysis platform [54]. The regular and symmetrical configuration of the buildings allows for the realisation of planar 2D models, where only the walls are explicitly modelled, since the horizontal seismic forces are absorbed by them. The behaviour of this type of structural element could be reproduced with different techniques, such as distributed plasticity [81], multiple vertical line element model (MVLEM) [82, 83], or more complex and refined methods based on a non-linear formulation [84]. In the present study, the design prescriptions led to the size of slender walls with a flexural-dominated behaviour and negligible shear deformations, thus the baseline MVLEM results in a suitable modelling solution both in terms of response precision [85] and computational efficiency. The MVLEM element recreates the axial-flexural behaviour with a series of uniaxial macro-fibres coupled together at their bottom and top sections using two rigid beams. Hence, the dynamic response depends on the constitutive laws assigned to the uniaxial materials of the macrofibers. On the other hand, the shear behaviour is modelled with a horizontal spring located at a defined height from the bottom section, which corresponds to the relative rotation centre of the main element. Thus, an entire shear wall is modelled by vertical stacking of a series of MVLEM elements on each other.

Consequently, in the present study, the analysed planar models are composed of a unique shear wall per direction with a vertical discretization of six MVLEMs for each storey of the building, as in Figure 4-3. The design assumption of identifying the shear walls as *uncoupled* allows one to not model the shear walls in series since their seismic response is independent. Furthermore, five microfibers are used to discretise the element along the horizontal local axis. Namely, two of them are necessary to reproduce the behaviour of the unconfined boundary elements, while the remaining three account for the web reinforcement.

The constitutive laws of the materials are selected following the indications contained in the report developed by Kolozvari et al. [86], where the more suitable uniaxial materials for MVLEM are expressed. Specifically, the *ConcreteCM* in OpenSees library is adopted for both confined and unconfined concrete. This material is formulated with the hysteretic behaviour developed by Chang and

Mander [87], and the compressive properties of the confined concrete are calibrated considering the enhancing effect due to transverse reinforcement, using Mander formulations [56]. On the other hand, *SteelMPF* material is assigned to the longitudinal reinforcement bars, which is based on the constitutive law developed by Menegotto and Pinto [57] and extended by Filippou et al. [88].

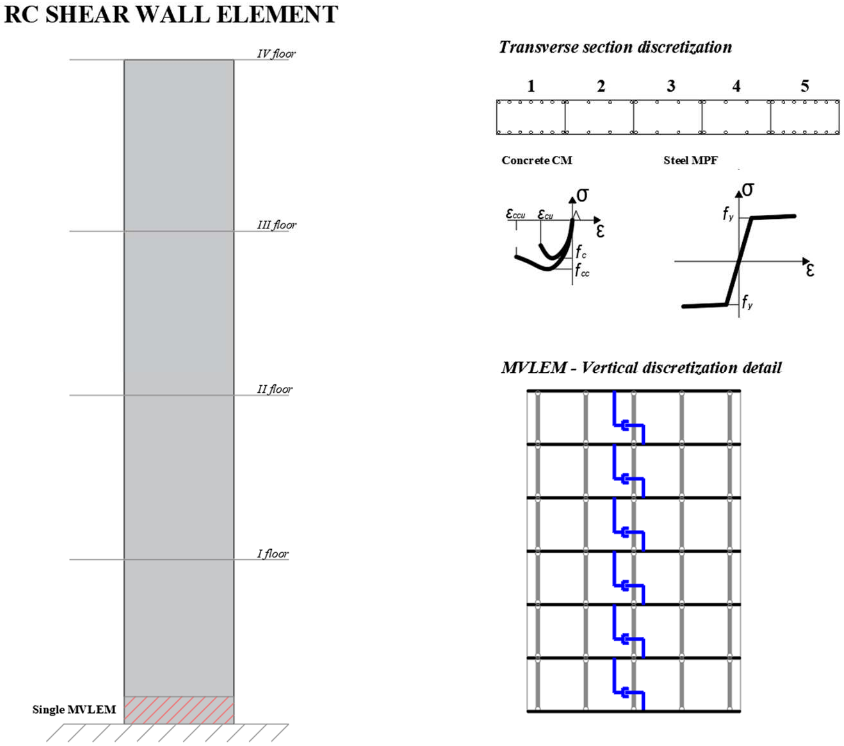

Figure 4-3 Nonlinear model of Shear Wall element

After defining the model, the fragility parameters are derived from the *Cloud Analysis* method [9], in accordance with the approach adopted in the previous Chapter for the bare and infilled frames (e.g. see Section 2.3). Consequently, the same dataset of 200 natural ground motions composed of 100 different events (Figure 2-12) is applied to all the models.

However, in this case, the nonlinear dynamic analyses are performed directly on the shear wall assembly avoiding the conversion to an equivalent SDOF. The nonlinear models of the SW buildings contain only the MVLEM element; thus, it is not necessary to simplify the modelling strategy to reduce the computational effort, and the seismic performance could be assessed using the actual shear wall element.

As a consequence, the definition of damage states is not based on the envelopes of the pushover curves. Thus, the engineering demand parameter (EDP) is expressed in terms of inter-storey drift ratio (IDR), and the thresholds are set considering well-established literature values [89], specifically ASCE 41 [90] limits are adopted herein. Specifically, the *slight* damage state (SD) is reached at 0.5% of the IDR, while values of 1% and 2% are used for the *moderate damage states* (MD) and *near collapse* (NC), respectively. The collapse damage state is associated with a total loss of vertical load capacity, and following Gogus and Wallace [91] for the case of shear wall buildings is met when an IDR of 5% is achieved. At this point, the results of the nonlinear dynamic analysis could be post-processed to determine the fragility parameters, i.e. the median θ and the logarithmic standard deviation σ. In particular, Figure 4-4 shows the trend of the median θ against the elastic spectral acceleration $S_{ae}(T_1)$, which identifies the different levels of design intensity.

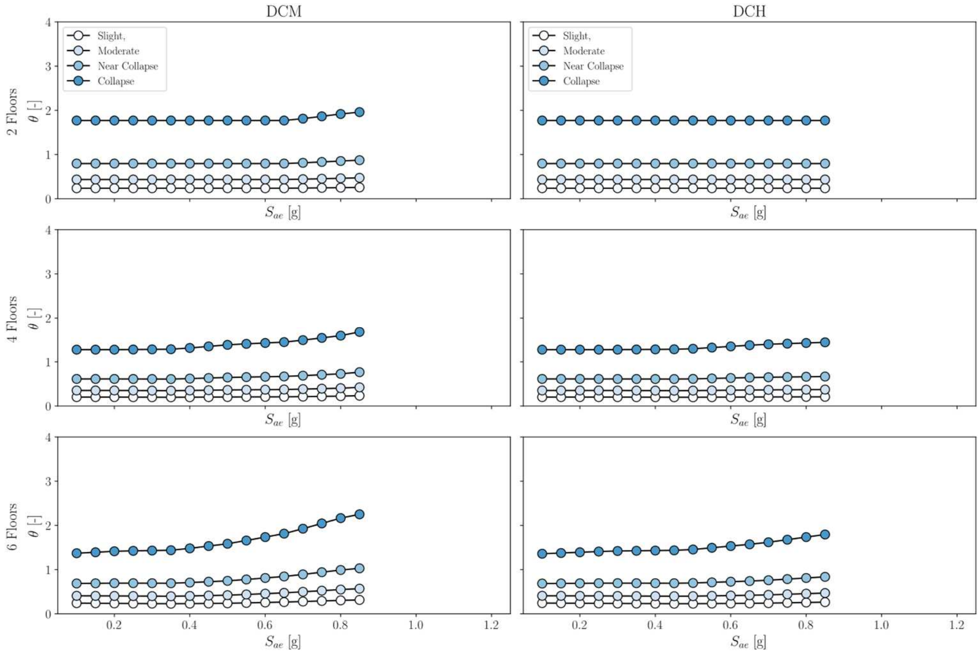

Figure 4-4 Correlation between the median θ and the spectral acceleration S_{ae}

First, both DCH- and DCM-designed buildings exhibit a similar trend, given the number of floors, for all damage states. This means that the different prescriptions related to the desired ductility level do not influence the vulnerability of SW buildings. On the other hand, seismic performance varies depending on the number of floors. Specifically, low-designed buildings exhibit a vulnerability that increases with the number of floors, whereas those designed with higher S_{ae} values show an opposite trend. For instance, selecting an elastic spectral acceleration equal to 0.1g, the 2-storey case assumes a value slightly less than 2.0g, while in the 6-storey is approximately 1.5g. When designing with the maximum achievable $S_{ae}(T_1)$, the median amounts around 2.0g and 2.25g for the 2 and 6 storey buildings, respectively. Moreover, the two-storey cases show an almost steady trend along the variation of $S_{ae}(T_1)$, and this outcome could be due to the high impact of the minimum code requirements in the sizing process, which leads to an invariant seismic performance.

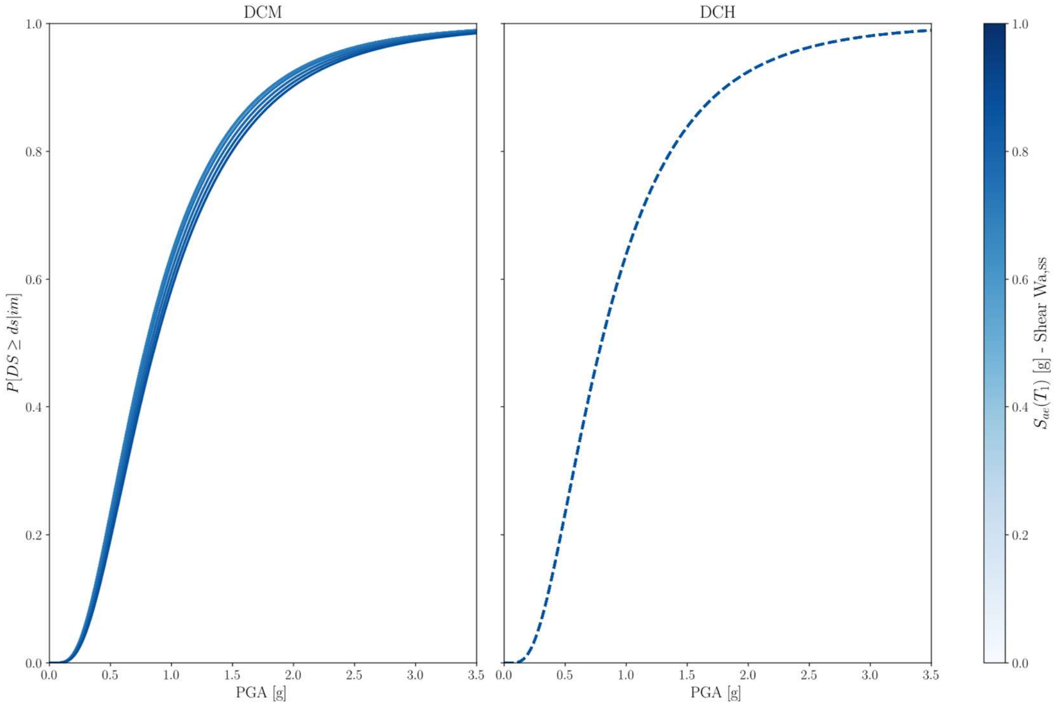

Figure 4-5 Fragility curves code-compliant SWs buildings – 2 storeys - NC

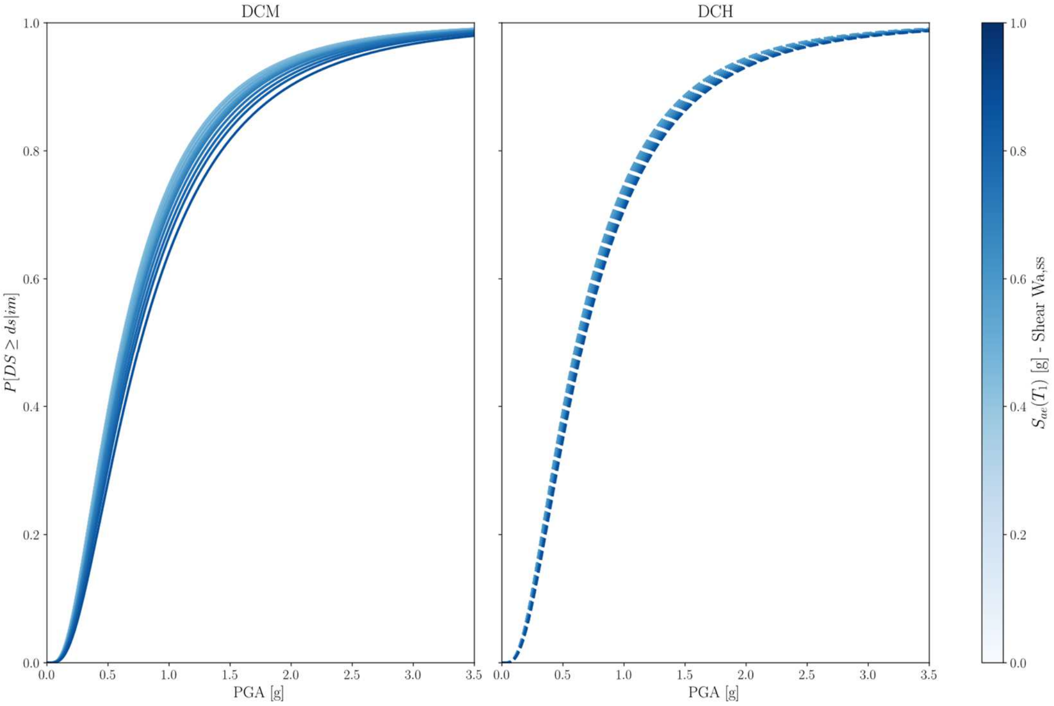

Figure 4-6 Fragility curves code-compliant SWs buildings – 4 storeys - NC

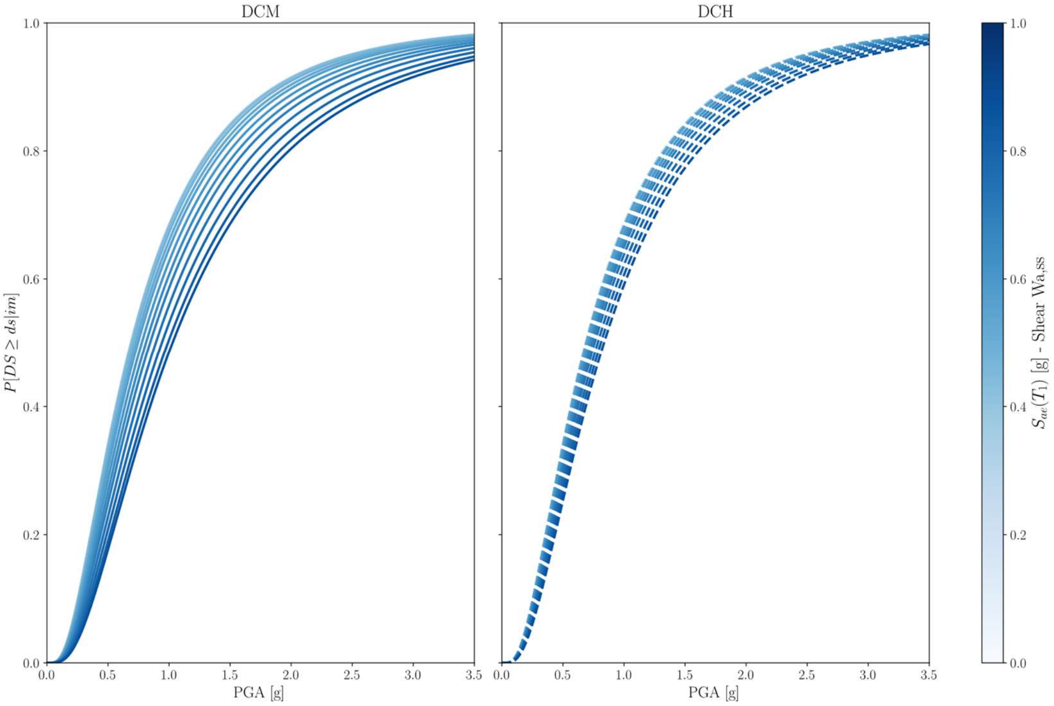

Figure 4-7 Fragility curves code-compliant SWs buildings – 6 storeys – NC

This effect is also underlined by the behaviour of the fragility curves, reported from Figure 4-5 to Figure 4-7, where the 6-storey curves are contained in a wider bundle than the 2-storey cases. The trend is highly notable for the DCH cases due to the greater behaviour factor, which implies the adoption of extremely reduced seismic design forces. In addition, this trend is ascribable to the seismic weight, which linearly increases the seismic forces with the number of storeys.

4.4 SEISMIC RELIABILITY MAPS

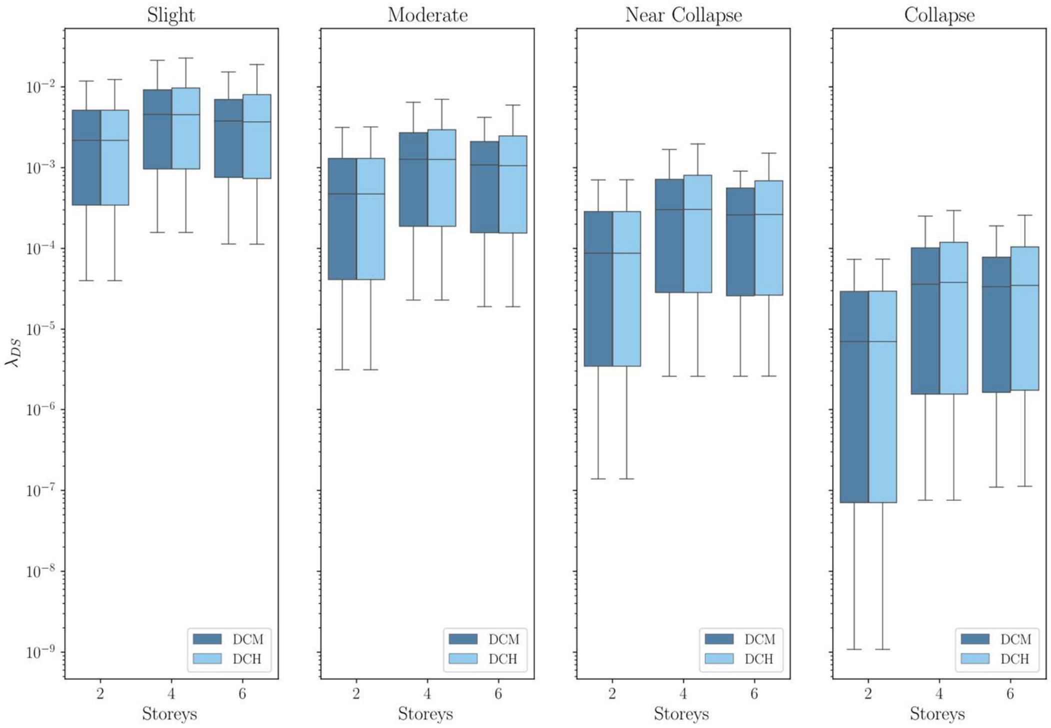

Figure 4-8 Seismic failure rates boxplot – Shear Walls

The seismic reliability maps for code-conforming SW buildings are obtained by calculating the mean annual frequency of each damage state for every Italian municipality. Therefore, the integration of the fragility curves on the specific hazard curve of the site must be performed, to solve the integral reliability expressed in Equation (1.4). In detail, this procedure consists of determining at each municipality the design spectral acceleration $S_{ae}(T_1)$ for the specific archetype building, thus it is possible to associate the results of the vulnerability assessment. Then, the site-specific hazard curve has to be computed starting from the results of a PSHA. These steps are extensively described in Section 2.4, since the same procedure proposed for frame-buildings is adopted herein for shear-wall ones.

Table 4-3 Summary of failure rates – Shear Walls

Case	**Damage State**	λ_f		
		Min	***Max***	***Mean***
2-DCH	ds_1 *(SD)*	3.99E-05	1.85E-02	3.04E-03
	ds_2 *(MD)*	3.10E-06	4.44E-03	7.74E-04
	ds_3 *(NC)*	1.39E-07	1.01E-03	1.74E-04
	ds_4 *(C)*	1.08E-09	2.29E-04	2.00E-05
2-DCM	ds_1 *(SD)*	3.99E-05	1.66E-02	2.99E-03
	ds_2 *(MD)*	3.10E-06	3.75E-03	7.54E-04
	ds_3 *(NC)*	1.39E-07	8.79E-04	1.67E-04
	ds_4 *(C)*	1.08E-09	1.90E-04	1.90E-05
4-DCH	ds_1 *(SD)*	1.58E-04	2.95E-02	5.68E-03
	ds_2 *(MD)*	2.30E-05	9.20E-03	1.71E-03
	ds_3 *(NC)*	2.58E-06	2.20E-03	4.61E-04
	ds_4 *(C)*	7.57E-08	4.47E-04	6.89E-05
4-DCM	ds_1 *(SD)*	4.40E-04	2.59E-02	5.42E-03
	ds_2 *(MD)*	1.58E-04	7.61E-03	1.58E-03
	ds_3 *(NC)*	2.30E-05	1.68E-03	4.13E-04
	ds_4 *(C)*	2.57E-06	3.53E-04	5.88E-05
6-DCH	ds_1 *(SD)*	7.56E-08	2.19E-02	4.60E-03
	ds_2 *(MD)*	1.13E-04	6.48E-03	1.40E-03
	ds_3 *(NC)*	1.90E-05	1.51E-03	3.82E-04
	ds_4 *(C)*	2.59E-06	3.31E-04	5.86E-05
6-DCM	ds_1 *(SD)*	1.12E-07	1.53E-02	4.08E-03
	ds_2 *(MD)*	1.14E-04	4.20E-03	1.18E-03
	ds_3 *(NC)*	1.90E-05	9.07E-04	3.06E-04
	ds_4 *(C)*	2.58E-06	2.17E-04	4.34E-05

First, the determined seismic failure rates are shown in the boxplot of Figure 4-8. These results show how the design ductility class leads to similar results considering both height variation and state of damage. However, the DCM cases exhibit slightly better reliability, which could be ascribed to the greater impact of using a higher behaviour factor in terms of seismic performance. Furthermore, when comparing the number of storeys, the 2-floor layouts seem to lead to safer code-conforming buildings, and this is consistent with the results highlighted from the fragility curves. Table 4-3 depicts the variation intervals of the failure rates for the investigated configurations. In detail, the shear-wall code-compliant building ranges from $7.56 \cdot 10^{-8}$ to $4.40 \cdot 10^{-4}$ for SD, and $3.10 \cdot 10^{-6}$ to $1.58 \cdot 10^{-4}$ for MD, while the intervals for the damage states of *near collapse* and *collapse* are $1.35 \cdot 10^{-7}$-$2.30 \cdot 10^{-5}$ and $1.09 \cdot 10^{-9}$-$2.59 \cdot 10^{-6}$.

Subsequently, the seismic reliability maps are illustrated from Figure 4-9 to Figure 4-12. The results outline the strict relationship between reliability and hazard in the subset of investigated buildings; thus, higher failure rate values are registered at more hazardous sites; in particular, this tendency is more evident with the increasing damage state. Additionally, the maps show a similarity between the 4- and 6-storey ranges of λ_f, which are slightly higher than those of the 3-storey ones.

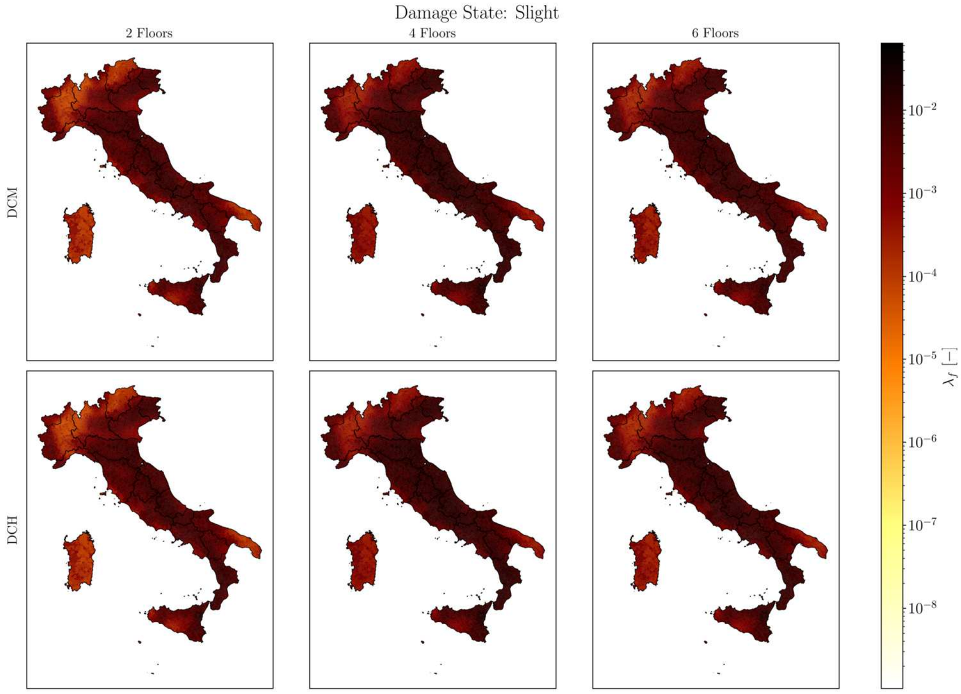

Figure 4-9 Reliability Maps - Shear Walls - SD

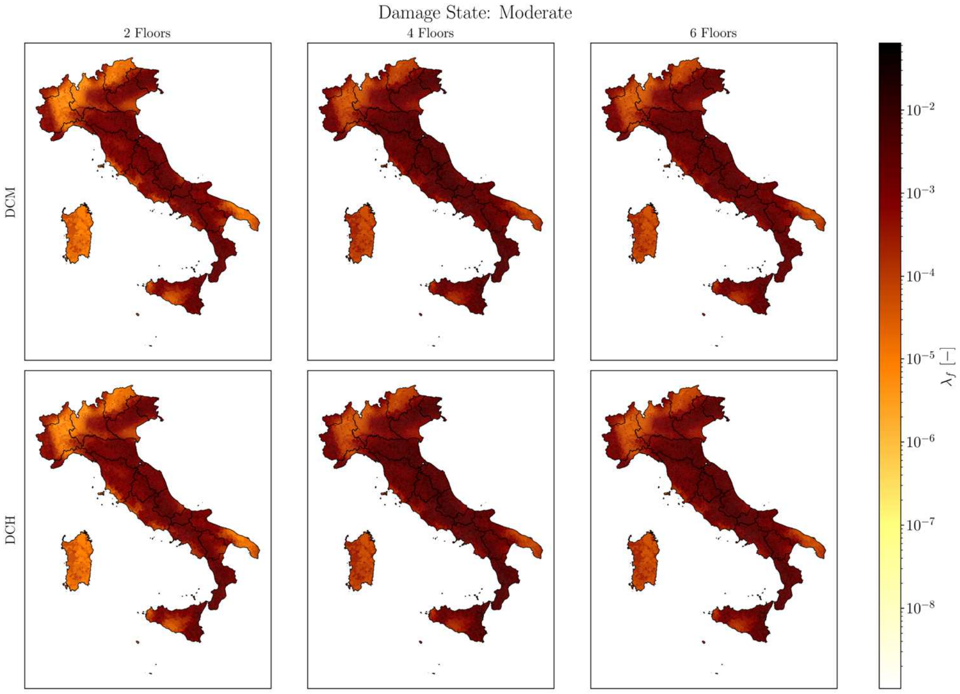

Figure 4-10 Reliability Maps - Shear Walls - MD

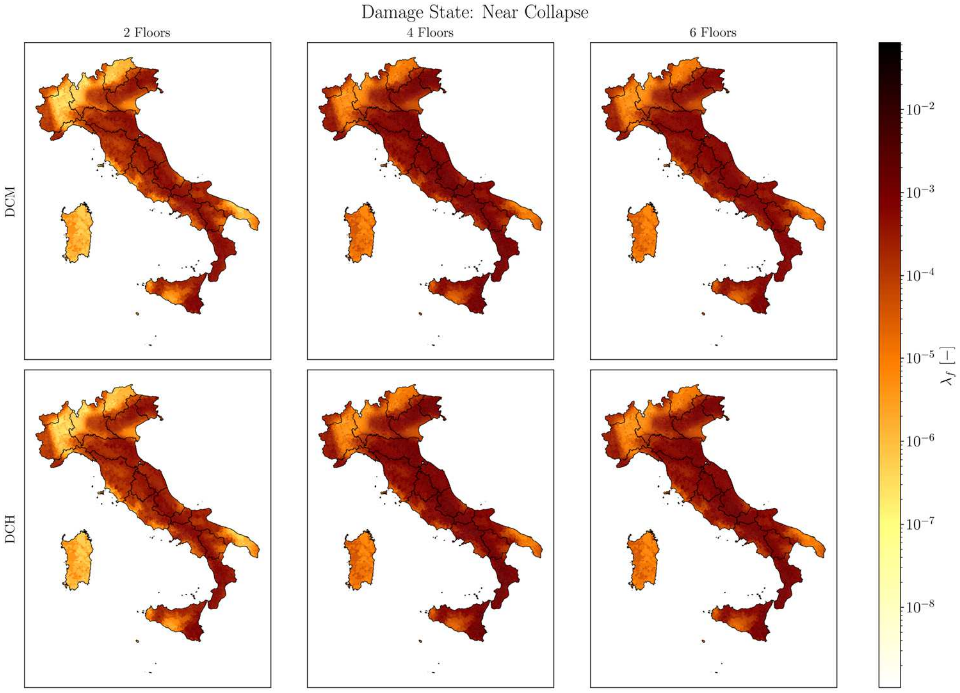

Figure 4-11 Reliability Maps - Shear Walls - NC

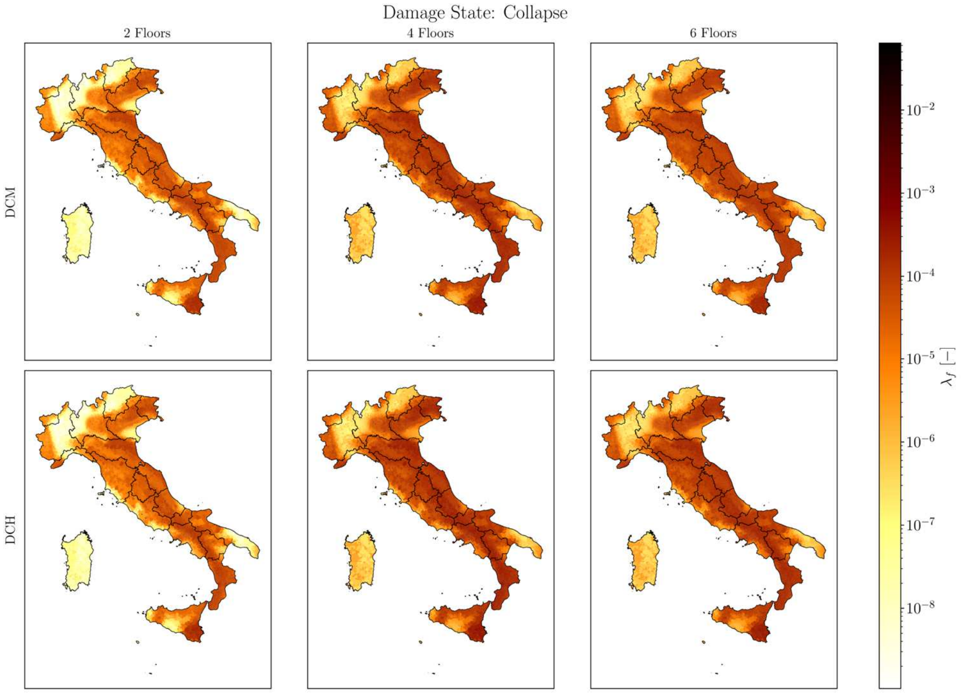

Figure 4-12 Reliability Maps - Shear Walls – C

The last step of this process consists of determining a functional form to relate the seismic design action at a specific place, in terms of PGA, to the achievable code-compliant seismic failure rate. In this way, the *hazard-dependent* reliability of a newly designed structure could be preliminary estimated from a practitioner. The mathematical expression of this relationship has been reported in (2.9), and it has the same form as the hazard curve. Therefore, Figure 4-13 shows the results of the regression analysis for all the shear wall building layouts, while Table 4-4 lists the parameters of the statistical model.

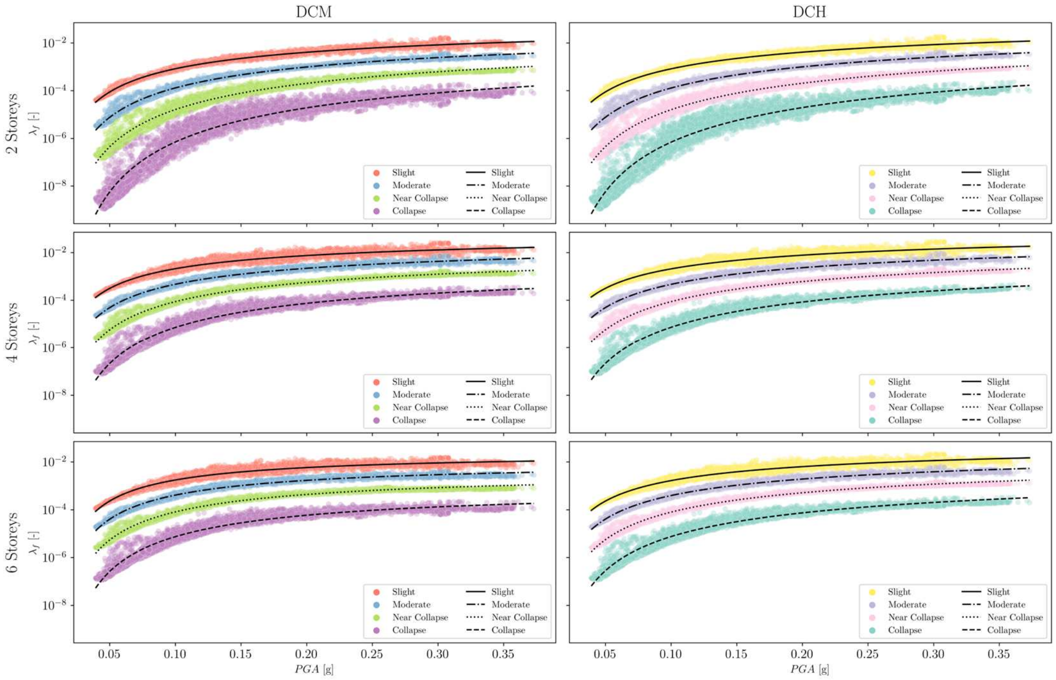

Figure 4-13 Correlation PGA-λ_{DS} - Shear Walls

Table 4-4 Regression parameters – Shear Walls

Shear-Wall Type	***DS***	k_0	k_1	k_2	σ	R^2
2-DCH-B	ds_1	-3.229	-0.303	0.017	0.137	0.993
	ds_2	-4.015	-0.313	0.016	0.166	0.993
	ds_3	-4.927	-0.310	0.018	0.337	0.982
	ds_4	-6.342	-0.296	0.023	0.695	0.958
2-DCM-B	ds_1	-3.314	-0.280	0.022	0.138	0.99
	ds_2	-4.126	-0.289	0.021	0.168	0.99
	ds_3	-5.066	-0.286	0.023	0.341	0.98
	ds_4	-6.532	-0.270	0.029	0.701	0.96
4-DCH-B	ds_1	-3.060	-0.245	0.026	0.200	0.977
	ds_2	-3.826	-0.250	0.023	0.134	0.993
	ds_3	-4.728	-0.239	0.024	0.154	0.994
	ds_4	-6.142	-0.214	0.031	0.344	0.980
4-DCM-B	ds_1	-3.313	-0.179	0.040	0.199	0.977
	ds_2	-4.146	-0.186	0.035	0.132	0.993
	ds_3	-5.128	-0.177	0.036	0.156	0.993
	ds_4	-6.674	-0.152	0.042	0.353	0.978
6-DCH-B	ds_1	-3.326	-0.206	0.034	0.203	0.978
	ds_2	-4.122	-0.213	0.029	0.139	0.992
	ds_3	-5.051	-0.206	0.029	0.153	0.993
	ds_4	-6.505	-0.184	0.032	0.323	0.980
6-DCM-B	ds_1	-4.120	-0.025	0.071	0.206	0.975
	ds_2	-5.033	-0.048	0.062	0.149	0.990
	ds_3	-6.099	-0.054	0.059	0.176	0.990
	ds_4	-7.772	-0.044	0.060	0.356	0.974

5 RELIABILITY-TARGETED BEHAVIOUR FACTOR

This Chapter focusses on the evaluation of a force-reduction coefficient to introduce in the current code design process, to explicitly consider the seismic reliability. Specifically, this *reliability-targeted* indicator will be formulated by means of a hands-on approach for the benchmark structural archetypes analysed in the previous Chapter, namely the RC frames, both in the bare and infilled condition and the RC shear-wall ones.

5.1 METHODOLOGY

The outcomes of seismic reliability analyses performed in the previous Chapter stressed how the safety of code-compliant buildings is strictly proportional to the hazard of their specific construction site. This means that the paradigm at the basis of most current Codes led to *hazard-targeted* structures rather than *reliability-targeted* ones because they are not capable of guaranteeing a uniform probability of failure across the land.

For this reason, the framework mentioned above has been adapted to overcome such an underlying flaw. Namely, it has been used to move into a reliability-targeted approach based on explicitly accounting for the desirable level of seismic safety. The core idea lies in the fact that to achieve a different seismic performance, it is necessary to design the building with a different spectral acceleration, but this is directly related to varying the ratio between the elastic spectral acceleration derived from the UHS $S_{ae}(T_1)$ and the one capable of ensuring the adequate fragility $S_{ad}^{*}(T_1)$, which coincides with the formulation of the behaviour factor q. In other words, it is possible to achieve different levels of seismic reliability by simply changing the behaviour factor at the beginning of the design process.

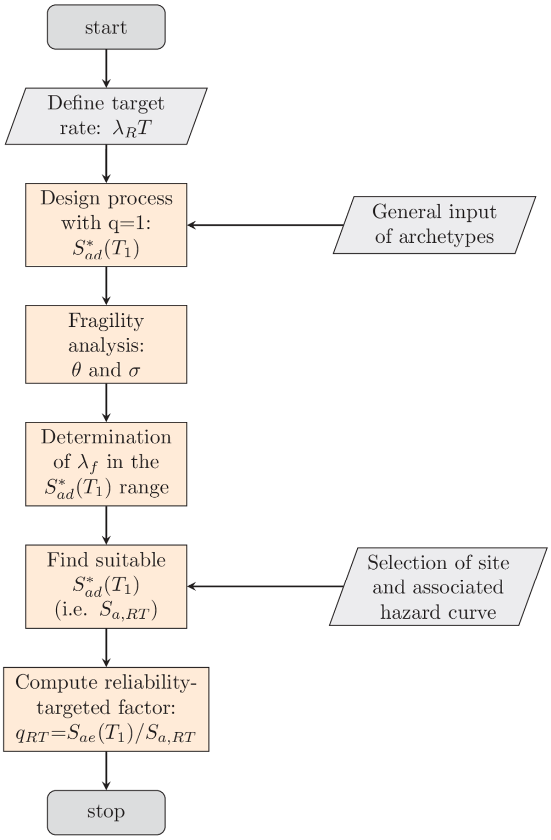

Figure 5-1 Framework for deriving q_{RT} factors

As a consequence, the algorithm developed to parametrically size code-compliant buildings, both for frames and shear walls, has been further utilised to re-analyse them with a wider range of spectral acceleration and a unitary behaviour factor, as illustrated in Figure 5-1. To this end, the upper limit of this interval is automatically identified when sections of the structural elements reach an unfeasible size for practical applications (i.e., beams' height), which means that for higher spectral accelerations, it would be more suitable to move to different resistive structural schemes.

After that, the results of these fictitious design spectral accelerations were inserted into the framework to assess their vulnerability. Hence, a set of *site-independent* fragilities is derived, since they are linked to the design phase only by the ratio with a possible elastic spectral acceleration. Figure 5-2 depicts the effect of adopting a wider range of design cases by comparing the so-derived fragility curves with the ones obtained from code-compliant sizing (i.e. design spectral accelerations determined with the classical behaviour factor).

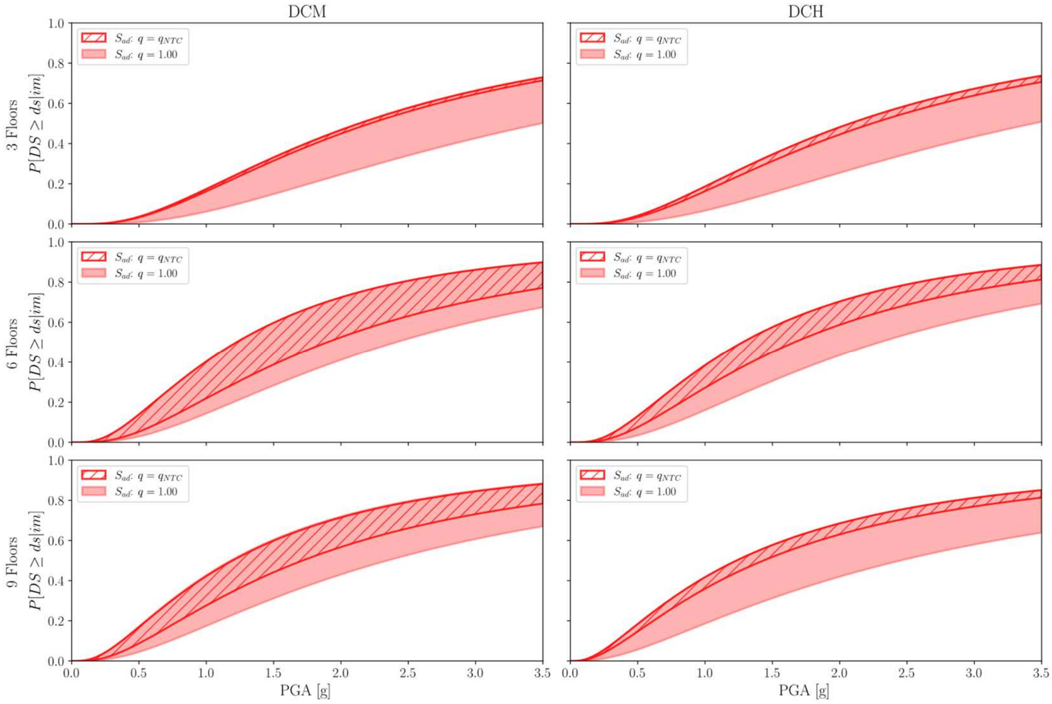

Figure 5-2 Fragility curves for reliability-targeted design

At this point, it is possible to convolve the seismic hazard curve of a specific site of interest to the fragility curve, which allows achieving the target performance fixed a priori regarding a certain damage state. Hence, the ratio between the fictitious spectral acceleration $S_{ad}^{*}(T_1)$ and the site's specific UHS elastic one $S_{ae}(T_1)$, will lead to the definition of the behaviour factor that ensures the achievement of the desired failure rate λ_t, i.e. the so-called *reliability-targeted* behaviour factor q_{RT}.

As a consequence, the maps of the *reliability-targeted* q_{RT}, associated with an arbitrary seismic failure rate, could be derived by repeating the process outlined above for all municipalities, in order to derive a uniform reliability level across the country.

However, it should be underlined that the target threshold of seismic safety should be defined according to social characteristics, which are strictly dependent on the examined country. Referring to current European building regulations, the minimum level of ensured reliability is not clearly stated in the case of seismic actions [42]. On the other hand, in an informative Annex of Eurocode 0 [2], the target annual failure rate for static loads in ordinary structures is explicitly set equal to $\lambda_t = 1 \cdot 10^{-6}$. As a consequence, the calculations in the following Sections will be performed considering two reasonable target values according to relevant studies. Namely, a target value equal to $\lambda_t = 2 \cdot 10^{-4}$ (i.e. 1% for 50 years) consistent with the national risk of the USA [92] and a stricter one at $\lambda_t = 1 \cdot 10^{-4}$ as proposed in [32] referring to a European country.

Finally, in the presentation of the outcomes for the reference buildings, it will be introduced Cornell's reliability index B_{RT} [93], to associate q_{RT} factors with an indicator of the same magnitude:

$$\mathrm{B}_{RT} = -\Phi^{-1}(P_{f,RT}) \tag{5.1}$$

where the operator Φ^{-1} expresses the inverse of the cumulative standard normal distribution function, while $P_{f,RT}$ is the probability of failure of the component in the selected time-window *T* and linked to the failure rate with the Poissonian event formulation:

$$P_{f,RT} = 1 - e^{-\lambda_{f,RT} \cdot T} \tag{5.2}$$

Thus, when the reference time-window is set equal to 1 year, the two quantities coincide. It should be underlined that, the indicator B_{RT} has an inverse relationship with the failure rate, hence high values of B_{RT} corresponds to high seismic safety (i.e. low failure rates).

5.2 RELIABILITY-TARGETED BEHAVIOUR FACTOR FOR BARE FRAMES

In this Section, the above-mentioned procedure is applied to the RC bare frame archetypes investigated in Chapter 2. To sum up, three different elevation layouts of typical residential buildings in Italy have been analysed (i.e. 3-, 6-, 9-storey), considering both the medium and ductility classes.

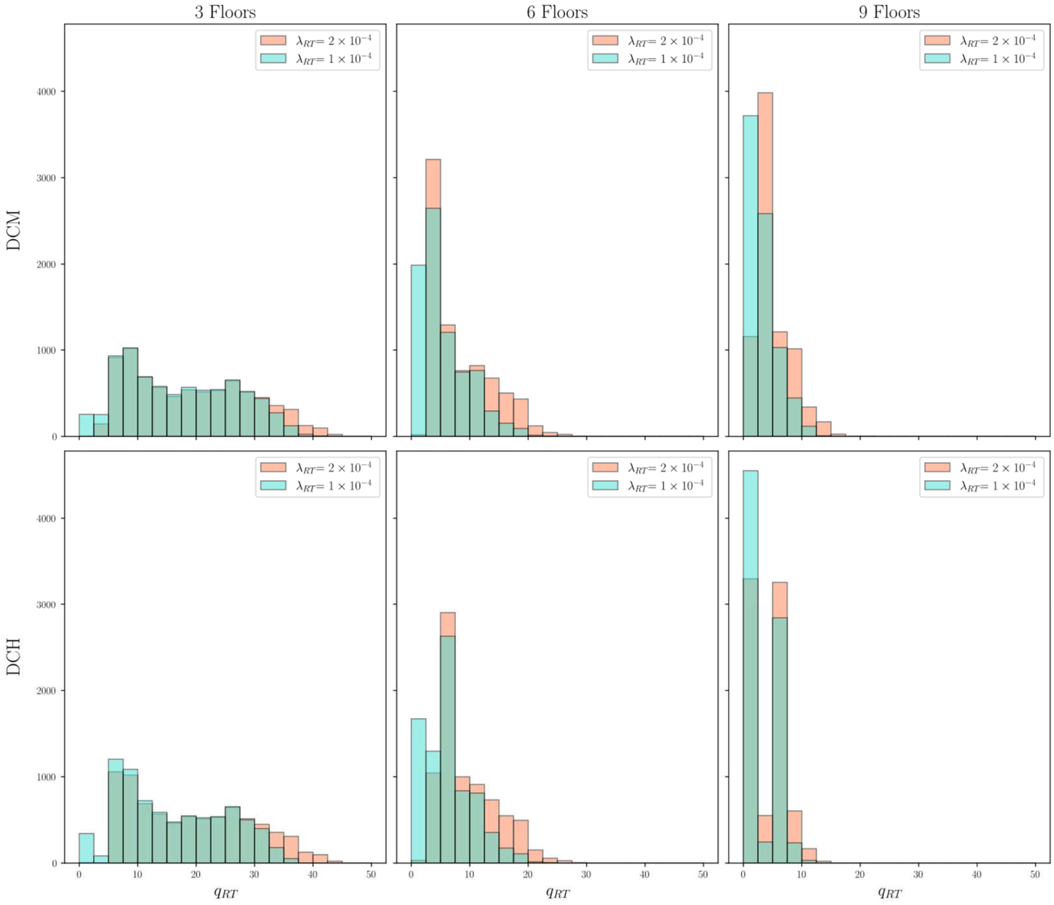

Figure 5-3 Histogram of reliability-targeted q_{RT} - Bare Frames

Firstly, the results of the reliability-targeted behaviour factor q_{RT} are reported in Figure 5-3. This figure shows the q_{RT} histograms for all the configurations studied, and they are calculated for both of the two fixed levels of reliability, i.e. $\lambda_{RT} = 2 \cdot 10^{-4}$ and $\lambda_{RT} = 1 \cdot 10^{-4}$, respectively. It should be underlined that high values of q_{RT} occur in cases where code-compliant design, adopting the standard behaviour factor q_{NTC}, would lead to a λ_f lower than that stated at the beginning of the reliability-targeted process (i.e. λ_{RT}).

Histograms depict a clear decreasing trend with the number of storeys, since the 3-storey cases reach values of q_{RT} up to around 40, while the 9-storey configurations do not exceed 20. This behaviour is highlighted by the distribution of the data. The 6- and 9-storey frames are more concentrated in the surrounding of the q_{NTC} value, whereas the 3-storey frames are fairly evenly distributed throughout their range.

Furthermore, Figure 5-3 does not show a significant difference between the DCM and DCH classes, which is consistent with the results of the code-compliant seismic reliability analyses. Furthermore, the histograms highlight the effect of fixed target failure rates in terms of the q_{RT} distribution. Specifically, a stricter choice of the seismic safety level would cause a left-shifted distribution of force reduction coefficients. For example, in the 6-storey DCM layout, the mean values are equal to 8.32 and 5.57 for $\lambda_{RT} = 2 \cdot 10^{-4}$ and $\lambda_{RT} = 1 \cdot 10^{-4}$, respectively.

To better address this tendency, reliability-targeted behaviour factor maps of Italy have been determined. Therefore, Figure 5-4 shows how for 6- and 9-storey frames q_{RT} lower values occur in more hazardous sites, which means that to meet the minimum safety level, it would be necessary to design them with lateral forces greater than those currently prescribed in the Code. On the contrary, a completely inverse trend is observed for 3-storey conditions, since the highest values of q_{RT} are experienced in hazardous sites. The reason for this performance lies in the ranges of variation of the seismic failure rates λ_f determined in Section 2.4.

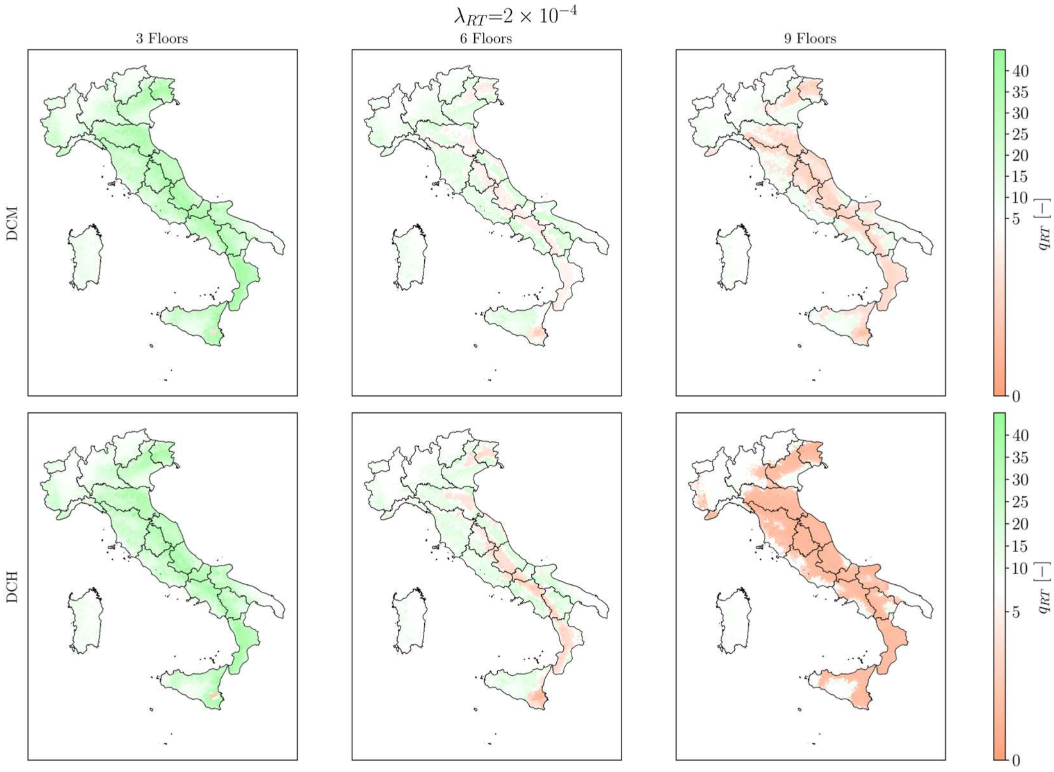

Figure 5-4 Italian maps of reliability-targeted factors q_{RT} – Bare Frames

More in detail, Table 2-3 showed how code-compliant 3-storey bare frames attained a maximum value around the targeted λ_f but the mean one is far lower than the threshold, namely around $2.00 \cdot 10^{-5}$. In other words, most of the sites meet the desirable safety level; therefore, it is possible to increase the force reduction coefficient to optimise the design outcomes; thus, this aspect particularly affects sites with high seismic hazard. On the other hand, the mean value of code-compliant failure rates reaches the fixed threshold by increasing the height; therefore, the hazard-dependent reliability outlined in Section 2.4 implies a lower behaviour factor directly proportional to the seismicity for ensuring the achievement of λ_{RT}.

Table 5-1 Summary of q_{RT} - Bare Frames

Case	$\lambda_{RT}=2\cdot10^{-4}$			$\lambda_{RT}=1\cdot10^{-4}$		
	Min	*Max*	*Mean*	*Min*	*Max*	*Mean*
3-DCH	2.15	45.00	19.07	1.33	37.74	16.18
3-DCM	2.42	45.00	19.06	1.35	40.05	17.10
6-DCH	1.27	29.27	9.37	0.74	23.23	6.25
6-DCM	1.58	29.11	8.32	0.62	23.23	5.57
9-DCH	1.09	15.52	4.34	0.70	11.77	3.23
9-DCM	1.28	21.10	5.03	0.52	13.13	3.47

The q_{RT} ranges are further highlighted in Table 5-1, which reports the minimum, maximum, and mean values obtained for both of the λ_{RT} investigations. These results are comparable to those obtained in similar recent works, such as those of Ricci et al. [40] and Baltzopoulos et al. [39]. However, the results could be compared only in terms of macrotrend since different assumptions have been made, both at the design level and at the criteria for collapse evaluation. However, referring to the common 6-storey case, it has been confirmed that the general attainment of values higher than q_{NTC} for low seismicity sites and an opposite behaviour with increasing hazard.

Furthermore, Table 5-1 shows that all the investigated layouts exhibit a mean q_{RT} higher than the code-compliant one, for both DCM and DCH, when fixing a target failure rate equals to $2\cdot10^{-4}$. In other words, this implies that, on average, frames could be designed with forces lower than current ones, and in parallel ensuring an adequate level of seismic safety. To this end, the q_{RT} data have been classified as a function of the code-conforming behaviour factor; therefore, they have been classified: as "*Higher*" when q_{RT} exceeds q_{NTC}, "*Lower*" for the opposite condition, and "*Equal*" for the remaining one.

As a consequence, Figure 5-5 shows the categorisation outcomes in the case of $\lambda_{RT}=1\cdot10^{-4}$, and it attests to the previous considerations. In detail, the reliability-targeted design of 3-storey frames could be performed with force lower than code-compliant conditions, while this is possible only for half of the sites in 9-storey buildings. Additionally, Figure 5-5 highlights a slightly worse performance of the DCH prototypes compared to the DCM, as the percentage of the "*Lower*" category is more significant.

The effectiveness of the developed approach is demonstrated in Figure 5-6, which compares the code-conforming failure rates derived in Section 2.4 against those obtained by adopting the reliability-targeted procedure. In particular, Figure 5-6 shows the case of 9-storey DCM and DCH frames with a threshold set at $\lambda_{RT} = 1 \cdot 10^{-4}$.

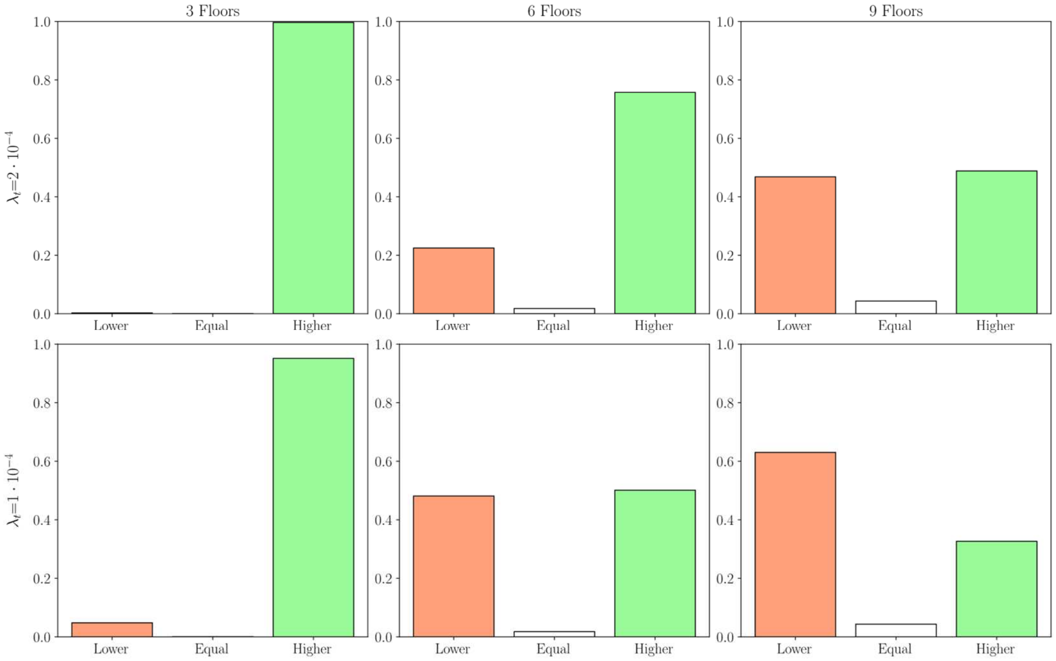

Figure 5-5 Bar chart of q_{RT} - Bare Frames

The limited range of variation of the colouring contour in the maps on the right of Figure 5-6, immediately proves the achievement of the minimum target failure rate. Code-compliant maps show a darker colouration, and their shading follows the trend of the hazard maps, while the reliability-targeted ones are characterised by a more uniform behaviour, which is consistent with the explicit aim of the developed procedure.

However, it should be noted that some areas of the reliability-targeted maps exhibit a brighter colour than the one associated with the threshold. Namely, this occurs mostly in low-seismicity zones, for instance, in the territory of Lombardia and Piemonte (i.e. north-west areas) and the Sardegna island. The cause of this outcome lies in the limited range of reliability values that are achievable for a specific site of interest due to some constraints.

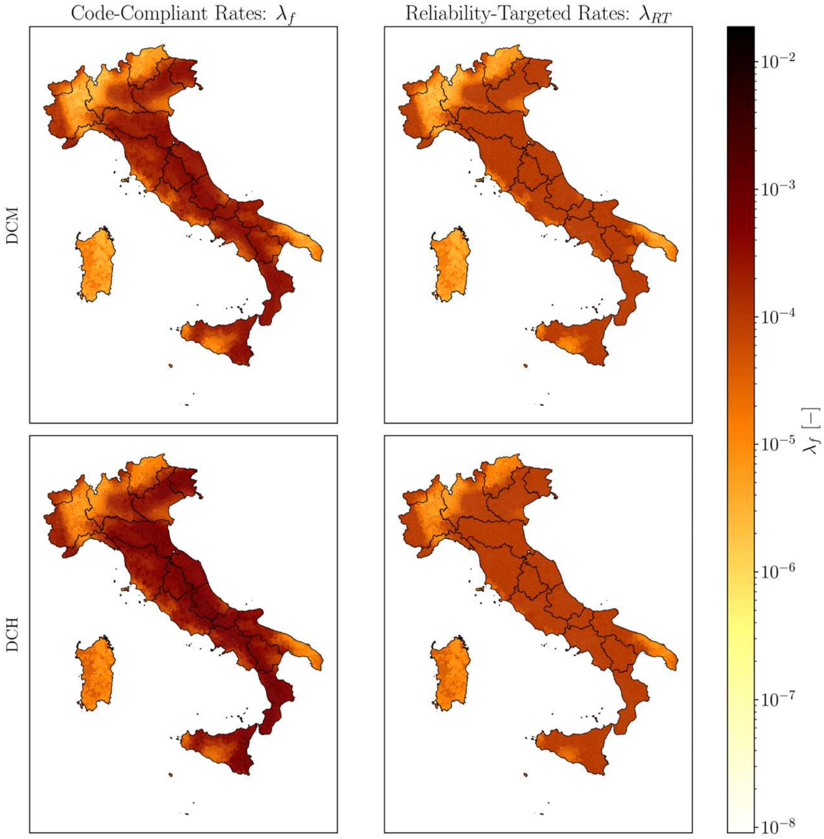

Figure 5-6 Comparison of failure rates: code-compliant vs. reliability-target - Bare Frames

This effect is highlighted in Figure 5-7, where the relationship between the level of safety, expressed in terms of the reliability index B_{RT}, and the reliability-targeted behaviour factor q_{RT} is determined for five specific municipalities. These sites are selected to cover the range of variation of the Italian seismic hazard in terms of *PGA,* as outlined in Table 5-2.

Table 5-2 Municipalities for curves B_{RT}-q_{RT}

Location	PGA [g]
Milano	0.059
Roma	0.163
Parma	0.211
L'Aquila	0.300
Cividale del Friuli	0.364

It is worth recalling that the adopted target failure rates correspond to a reliability index B_{RT}, using Equation (5.2), equal to 3.54 and 3.72 in the case of $\lambda_{RT} = 2 \cdot 10^{-4}$ and $\lambda_{RT} = 1 \cdot 10^{-4}$, respectively.

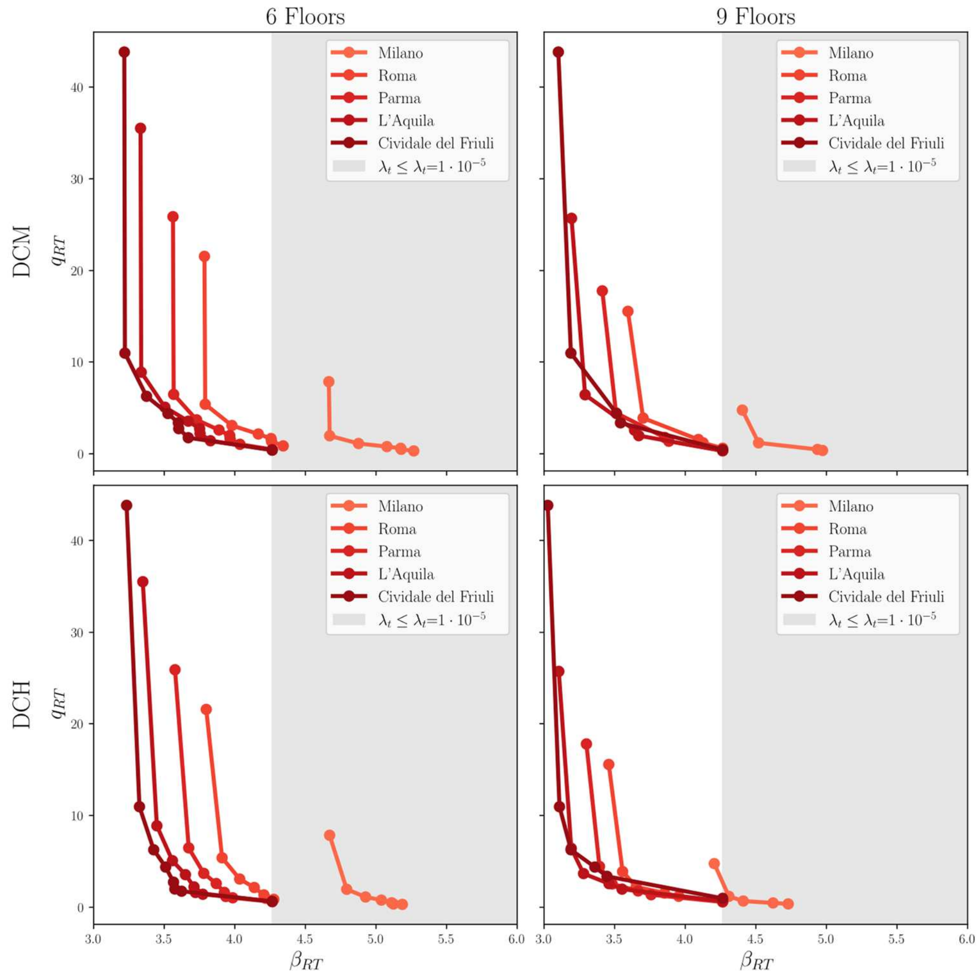

Figure 5-7 Reliability-targeted behavior factor q_{RT} curves - RC bare frames

As expected, the curves B_{RT}-q_{RT} shown in Figure 5-7, are characterised by an inverse proportional relationship, thus low values of desirable seismic safety are achievable with high safety factors that imply designing with lower seismic forces. However, the curves derived from this scheme span in limited ranges, which vary from site to site. More in-depth, the lower bound is determined by minimum code prescriptions. Namely, the seismic design is negligible below a certain level of spectral acceleration when compared to the static one, and so only minimum ductility detailing has to be placed. In other words, when this lower threshold is reached, the seismic response of the sized buildings remains constant, and this causes the inability to achieve lower values of B_{RT}. This outcome is shown in Figure 5-7 by the almost vertical segment at the left end of the curves, which proves the invariance of B_{RT}. On the other hand, the upper limit has to be ascribed to a geometrical infeasibility, since the section of elements cannot be increased indefinitely. As a consequence, it is not possible to achieve B_{RT} beyond some maxima in terms of the geometric dimensions of the beams or columns. In some way, the right endpoints of the curves suggest a change in the horizontal resisting scheme. Additionally, to highlight this concept, in Figure 5-7 it has been marked the region of seismic failure rates lower than $1 \cdot 10^{-5}$, and it is possible to see that there are almost no cases capable of achieving this target level of safety.

At this point, the outcomes of the developed method have been compared with those resulting from the one proposed by Žižmond and Dolšek [32]. In detail, the indirect formulation (RTA-I) has been applied to the DCM 6-storey frames located in the five established municipalities and setting a target failure rate equal to $2 \cdot 10^{-4}$. The values assigned to the overstrength factor r_s and the system ductility μ_s are equal to those suggested by the authors (r_s=2.0 and μ_s=6.0), as they are derived from previous parametric analyses performed on reinforced concrete buildings that comply with the Eurocode [94]. Therefore, the ductility reduction factor $r_{\mu NC}$ is determined according to the simplified literature formulation proposed in [95]. The last step in the implementation of this method requires the evaluation of the so-called risk-targeted safety factor γ_{im}, following equation proposed in [24]:

$$\gamma_{im} = \frac{1}{\gamma_{ls}} \cdot \left(T_R \cdot P_{C,a}\right)^{-\frac{1}{k} \cdot e^{\frac{k\beta_{Se,c}^2}{2}}} \tag{5.3}$$

Where the coefficient γ_{ls} represents the limit-state reduction factor that accounts for the transition from the collapse to the near-collapse damage state and it takes the value of 1.15. Furthermore, the coefficient k stands for the angular coefficient of the hazard curve in the bi-logarithmic space and the term β represents the standard deviation of the fragility curve and it is set equal to the proposed value of 0.4.

Table 5-3 Comparison of reliability-targeted behaviour factor

Location	**q_{rt} [-]**	**q_a [-]**
Milano	4.76	6.07
Roma	15.56	4.82
Parma	17.79	4.52
L'Aquila	3.36	4.32
Cividale del Friuli	4.04	2.70

Table 5-4 Comparison of reliability-targeted failure rates

Location	**λ_{NTC} [-]**	**λ_{rt} [-]**	**λ_a [-]**
Milano	1.53E-06	1.53E-06	1.53E-06
Roma	7.52E-05	7.52E-05	6.58E-05
Parma	1.60E-04	1.25E-04	1.25E-04
L'Aquila	2.48E-04	2.00E-04	1.75E-04
Cividale del Friuli	1.92E-04	2.00E-04	1.61E-04

Consequently, the results of the two methods have been determined in terms of force reduction factors and seismic failure rates and compared in Table 5-3 and Table 5-4, respectively. In detail, the data for the RTA-I formulation are indicated with the subscript *"a"*, while the data for the proposed hands-on approach are specified with the letters *"rt"*. As highlighted in Table 5-4, the approaches show a good agreement in terms of the seismic failure rates achieved. On the other hand, there is a discrepancy between the values of reliability-targeted behaviour factors. This inconsistency is more evident in less hazardous sites, where the code-compliant approach meets the target failure rates. In these cases, the presented hands-on approach utilises a spectral acceleration value as low as possible because the performance is governed by minimum code provisions, leading to seismic failure rates significantly smaller than the target one. At the same time, as exposed by Žižmond and Dolšek in [32], the overstrength factor should be adequately calibrated at low-hazard sites in order to properly account for the effects of minimum requirements, while in this example the reduction coefficient has been assumed according to the suggested pre-calibrated values. However, the overruling of minimum code prescriptions leads to identical probabilities of failure for the two approaches.

Finally, an application of the proposed reliability-targeted behaviour factors is presented. The selected case-study is one of the 6-storey frame configurations located in Cividale del Friuli ($PGA = 0.364g$), and the target value of proability of failure is set equal to $\lambda_t = 2.00 \cdot 10^{-4}$. The design process is performed for both the code-compliant approach ($q_{NTC} = 5.85$) and the reliability-targeted one ($q_{RT} = 3.13$). The latter force reduction factor is determined according to the outcomes of the extensive numerical analyses aforementioned, and its value implies the failure of current Codes' provisions in ensuring the achievement of the desirable level of safety. The outcomes of the two methodologies are compared by means of Table 5-5 and Figure 5-8, whose highlight the actual seismic performance of sized buildings and some characteristics of design process, respectively.

Table 5-5 Features of the case-study

	Code-Compliant	**Risk-Targeted**
Force reduction factor q	5.85	3.13
Design spectral acceleration [g]	0.15	0.28
Median PGA_c *(ds=NC) [g]*	1.71	2.05
Probability of failure (ds=NC)	2.97E-04	2.00E-04

Thus, Figure 5-8 shows an increment in both longitudinal reinforcement and sectional area of elements in the reliability-targeted configuration to bear the horizontal forces related to the lower behaviour factor. In particular, the gap is more pronounced in cross sectional area of beams when compared to columns one. This could be ascribed to the capacity design rules, which require that the flexural resistance of beams is directly dependent on seismic forces, whereas the characteristics of columns are governed by strength hierarchy principles (i.e. *strong column-weak beam*). Furthermore, focussing on Table 5-5; the applied behaviour factor leads to a reduction of almost 49% of the seismic probability of failure, which achieves the target of $2 \cdot 10^{-4}$. In addition, it should be noted that the chosen municipality represents a worst-case scenario due to its high peak ground acceleration, which implies that it is necessary to significantly increase both concrete volume and steel reinforcement area to achieve the target reliability level. Thus, when dealing with low-hazard sites, more balanced amounts of materials would be used in solutions with the reliability-targeted approach.

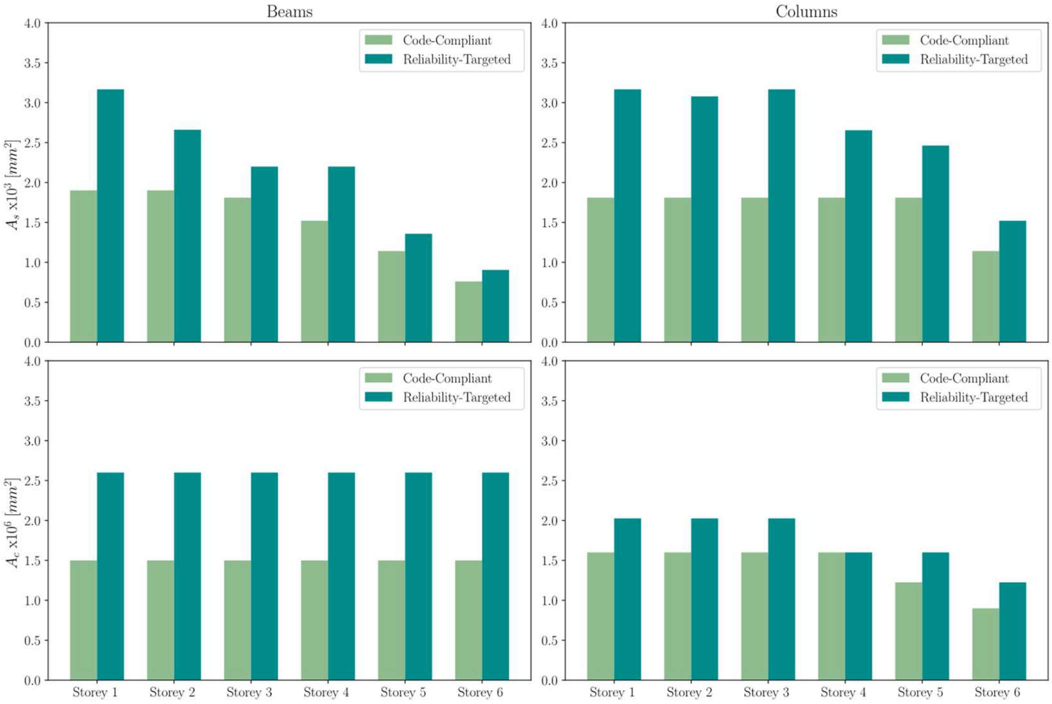

Figure 5-8 Comparison of design otucomes: Code-compliant and reliability-targeted

5.3 RELIABILITY-TARGETED BEHAVIOUR FACTOR FOR INFILLED FRAMES

In this Section, the developed *reliability-targeted* approach presented at the beginning of the present Chapter is applied to the RC infilled frames. Hence, the same logical flow previously adopted for bare-frame structures will be followed herein.

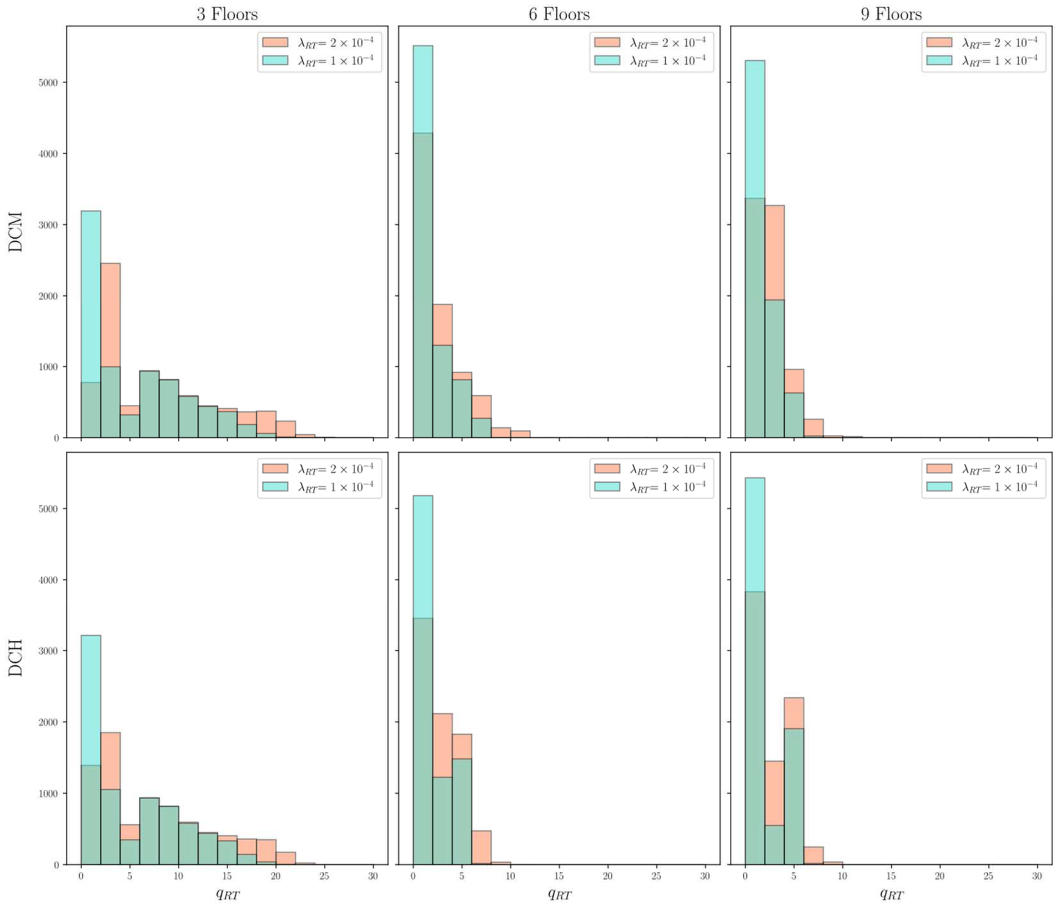

Figure 5-9 Histogram of reliability-targeted q_{RT} - Infilled Frames

Figure 5-9 shows the histograms of the q_{RT} *reliability-targeted* behaviour factors, which aims to emphasise their distributions considering the variation due to the different elevation layouts and the levels of target failure rates. The amplitude of the histograms is proportionally reduced with the number of floors, while it has a similar trend for the two classes of ductility. Namely, the 6- and 9-storey frames exhibit a very similar trend, as they slightly exceed a value equal to 10; whereas 3-storey cases show a larger interval of values, which spans up to 25. The global tendency of the q_{RT} factors is further highlighted by Table 5-6.

Table 5-6 Summary of q_{RT} - Infilled Frames

Case	**$\lambda_{RT}=2\cdot10^{-4}$**			**$\lambda_{RT}=1\cdot10^{-4}$**		
	Min	***Max***	***Mean***	***Min***	***Max***	***Mean***
3-DCH	1.21	23.86	7.50	0.78	20.50	5.51
3-DCM	1.31	25.55	7.74	0.85	21.62	5.69
6-DCH	0.68	10.01	3.07	0.54	7.15	2.44
6-DCM	0.73	11.15	2.87	0.57	8.82	2.21
9-DCH	0.90	9.16	3.18	0.68	7.19	2.33
9-DCM	0.94	10.64	2.82	0.72	7.48	2.15

Furthermore, it is possible to assess the effect of varying the desired level of safety. In detail, when moving from $\lambda_{RT} = 2 \cdot 10^{-4}$ to $\lambda_{RT} = 1 \cdot 10^{-4}$, a general decrease of q_{RT} is indicated. For instance, Table 5-6 shows how the minima of q_{RT} do not exceed the unit value, which means that it is necessary to design with spectral accelerations extremely higher than $S_{ae}(T_1)$. Furthermore, the reliability-targeted approach seems to lead to a more severe design even when considering the means, because their values are lower than the respective code-compliant behaviour factors, except for 3-storey frames that reach mean values up to 7.74.

When comparing these results with those of bare frames, it is possible to denote a difference in terms of the maximum q_{RT} achievable in all cases. For instance, the 3-storey bare frames span up to a value of about 45 which is considerably higher than the 25.55 reached by the respective infilled ones. This aspect is strictly related to the results of the code-compliant seismic reliability assessment, where the infilled layouts globally showed a poorer performance, which causes the adoption of a lower q_{RT} to achieve the same level of reliability.

Consequently, the maps of the reliability-targeted behaviour factor q_{RT} are derived. Figure 5-10 shows the slight proportional relationship between q_{RT} and seismicity because the colouration of the q_{RT} map has an inverse trend when compared to the hazard one (Figure 2-18). The highest values of force-reduction factors are reached in the less hazardous areas, which are coloured dark blue. All three elevation layouts exhibit a similar trend throughout the country, with the only difference being that 3-storey frames reach higher values of q_{RT}. Additionally, the main colour reported in the maps demonstrates that to achieve the desired level of safety, it is necessary to adopt behaviour factors slightly lower than the current ones.

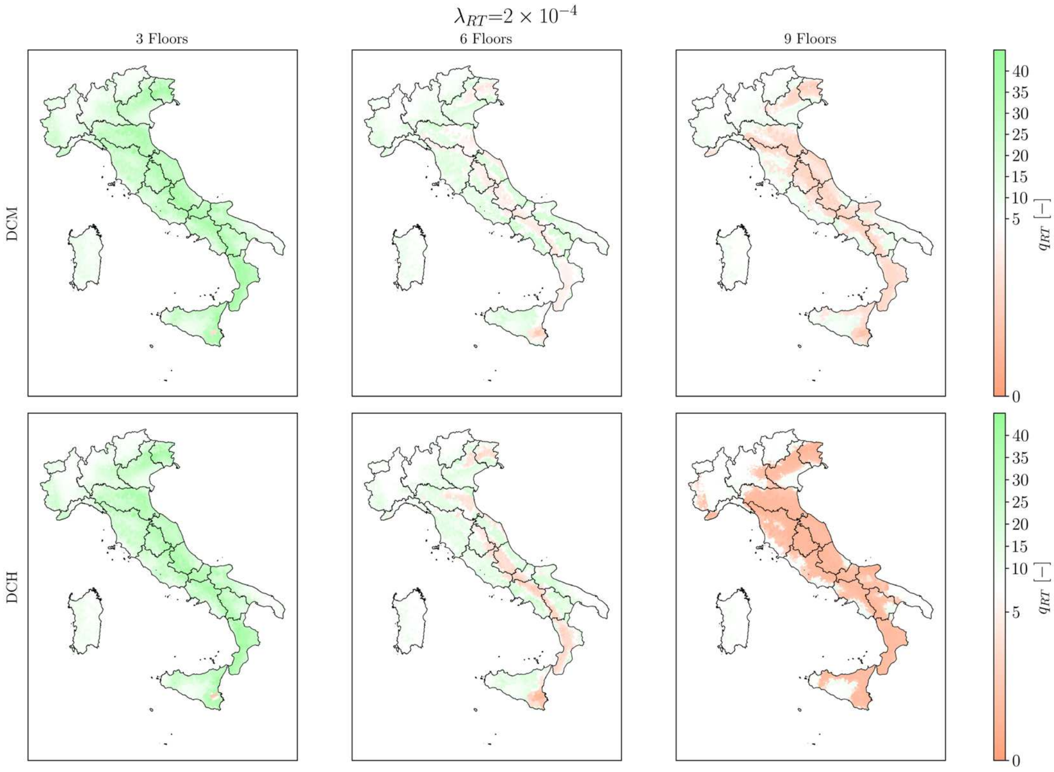

Figure 5-10 Italian maps of reliability-targeted factors q_{RT} – Infilled Frames

The main difference from bare frame cases is denoted in the 3-storey layout maps. Figure 5-4 shows that bare frames ensure the targeted reliability by adopting q_{RT} constantly higher than code ones, indicating independence from the seismic hazard. On the contrary, for the infilled frames, it is necessary to employ a behaviour factor lower than the code-conforming one, i.e. q_{NTC}. This means that explicit modelling of the stiffening effects of infill panels reduces the reliability of 3-storey frames.

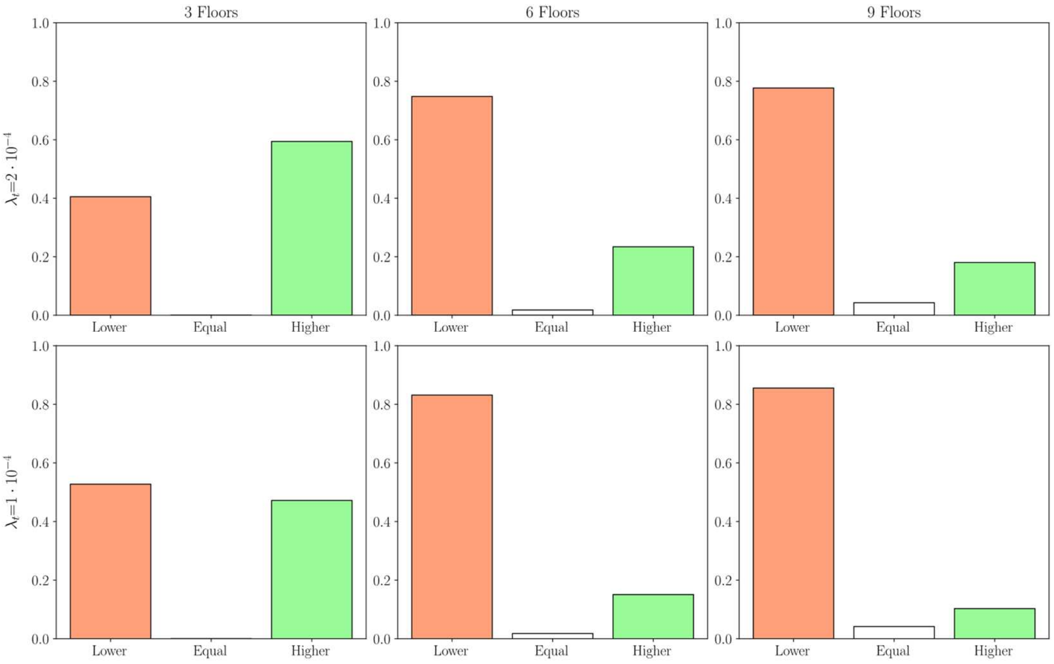

Figure 5-11 Bar chart of q_{RT} - Infilled Frames

In Figure 5-11 the behaviour factors are subdivided into three categories considering their ratio with the code-conforming q_{NTC}. The bar chart of the 'lower' condition increases with the number of floors, which means that 9-storey code-compliant frames are less reliable. Namely, the percentage of municipalities that need to be designed with higher forces grows from 40% to 80% when moving from 3- to 9-storey frames, respectively. More precisely, 6- and 9-storey frames show a similar percentage, which emphasises the fact that infill panels mostly affect the seismic performance of 3-storey frames. Furthermore, this aspect is highlighted when comparing Figure 5-11 and Figure 5-5. The latter shows that almost all municipalities fall into the "*Higher*" category, while in the infilled frames it does not exceed 60%. For the bare frames, a similar partitioning of the categories is obtained for the 9-storey cases.

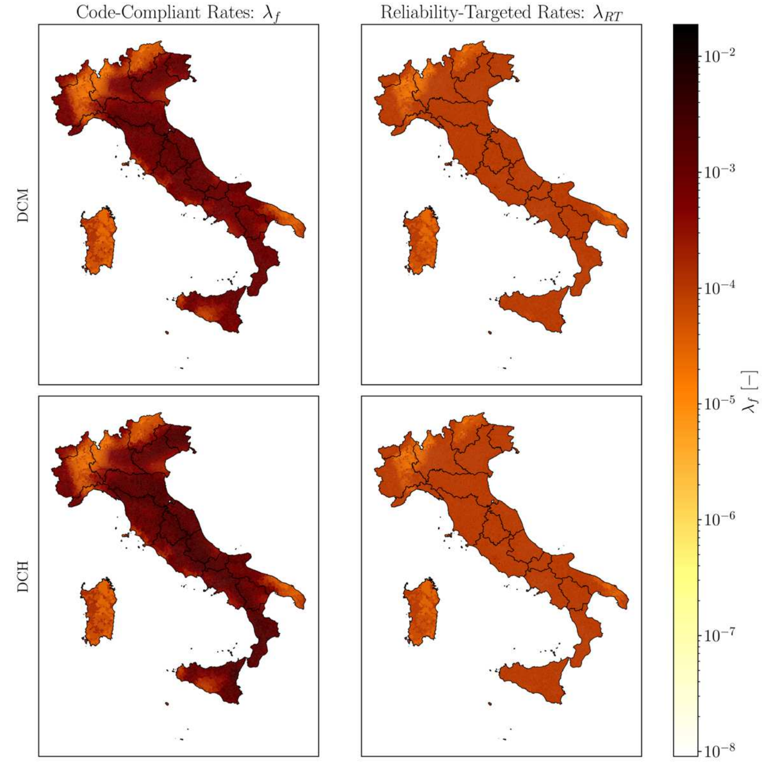

Figure 5-12 Comparison of failure rates: code-compliant vs. reliability-target - Infilled Frames

As previously done for the bare frames, the effectiveness of the established procedure is assessed by comparing the maps of failure rates throughout the land, between code-compliant and reliability-targeted designs. To this end, Figure 5-12 compares the results for 9-storey frames considering a target safety of $\lambda_{RT} = 1 \cdot 10^{-4}$. The targeted maps on the right show the achievement of a fairly uniform failure rate value throughout the entire territory, which implies that the adopted procedure is capable of mitigating the *hazard-dependent* reliability obtained by applying the design philosophy of the current code.

Moreover, Figure 5-12 shows how infilled frames are less affected by the low seismicity sites than the bare ones. Thus, the areas with a lighter colour are more limited than those previously found in Figure 5-6. In other words, the less safe conditions of code-compliant infilled frames (i.e. higher failure rates) lead to the possibility of ensuring a more uniform result when applying the reliability-targeted approach.

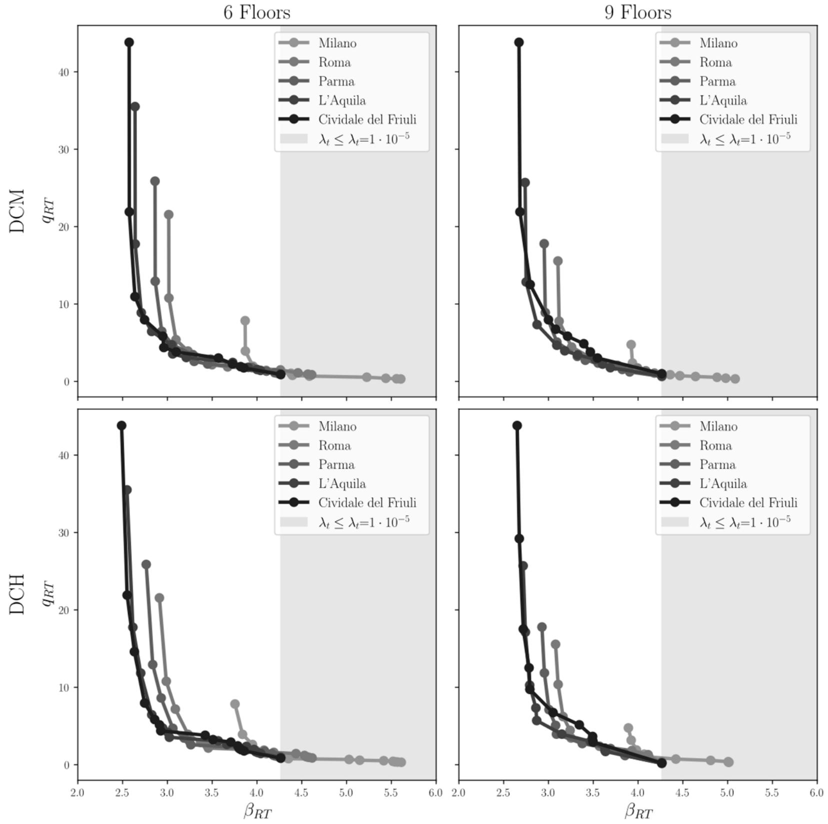

Figure 5-13 Reliability-targeted behaviour factor q_{RT} curves - RC Infilled frames

This implication is better explained by means of the B_{RT}-q_{RT} curves reported in Figure 5-13. This graph shows the inverse relationship between the reliability index B_{RT} and the targeted behaviour factor q_{RT} for five different municipalities characterised by an increasing PGA (see Table 5-2). From this figure, it is possible to observe that the curves shift left-side (i.e. to the less safety region) as far as the seismicity of the site increases, and this is associated with the role of the hazard in the convolution integral (1.4). However, the scatter between the curves is less marked than the one shown in Figure 5-7 for bare frames, and this is directly related to the outcome highlighted previously referring to the reliability-targeted failure rate maps. More in-depth, in Figure 5-7 the Milano-related curve is completely detached from the others and from the desired values of B_{RT}. This implies that for this site it would never be possible to reach the target failure rate, and this results in low failure rates, which appear in light colour on the reliability-targeted maps. On the contrary, the overlapping of the curves in the infilled frames allows for comparable levels of reliability in areas regardless of the hazard, and this implies achieving failure rates closer to the target one.

5.4 RELIABILITY-TARGETED BEHAVIOUR FACTOR FOR SHEAR WALLS

The reliability-targeted approach has also been applied to the RC shear wall buildings formerly assessed in Chapter 4. This process has been carried out setting two different target failure rates, namely equal to $\lambda_{RT} = 2 \cdot 10^{-4}$ and $\lambda_{RT} = 1 \cdot 10^{-4}$.

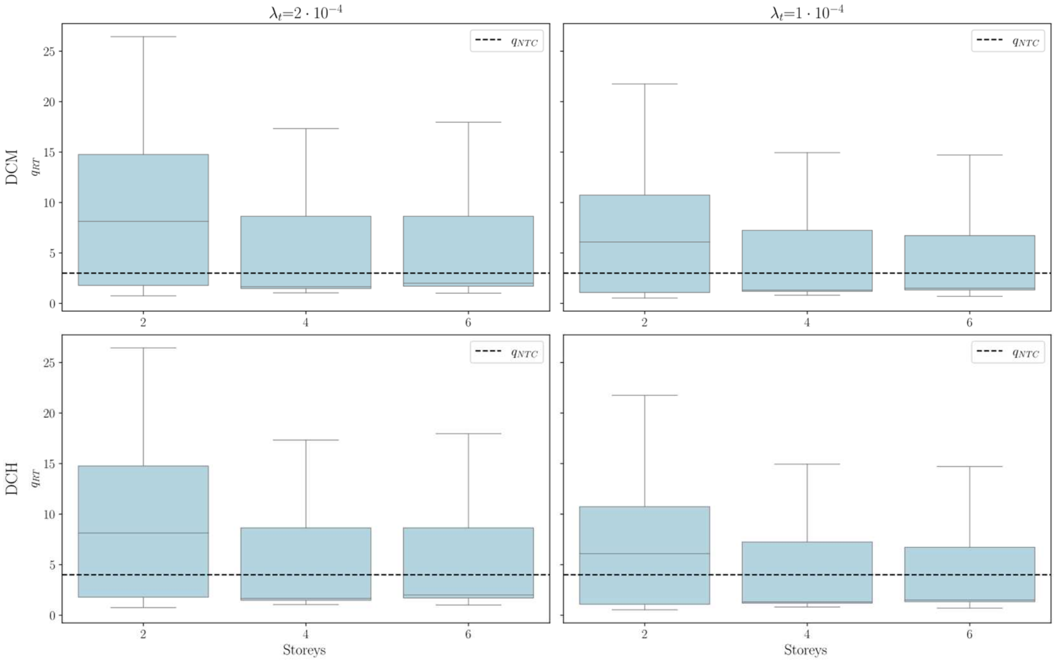

Figure 5-14 Boxplot of q_{RT} – Shear Walls

First, the global trend of the behaviour factors q_{RT} is presented in Figure 5-14. The boxplots show the general trend of decreasing reliability-targeted behaviour factor with increasing number of floors. For example, two-storey buildings register a maximum of 26.44, while four- and six-storey buildings do not exceed a value equal to 17.33 and 17.96, respectively. This results in the fact that only the first elevation layout shows a completely different trend, while the 4- and 6-shear walls behave in the same way.

Table 5-7 Summary of q_{RT} – Shear Walls

Case	$\lambda_{RT}=2\cdot10^{-4}$			$\lambda_{RT}=1\cdot10^{-4}$		
	Min	***Max***	***Mean***	***Min***	***Max***	***Mean***
2-DCH	0.75	26.44	9.28	0.54	21.75	6.42
2-DCM	0.75	26.44	9.28	0.53	21.75	6.42
4-DCH	1.04	17.33	5.16	0.81	14.94	3.96
4-DCM	1.04	17.33	5.16	0.81	14.94	3.96
6-DCH	1.01	17.96	5.22	0.70	14.94	3.95
6-DCM	1.01	17.96	5.22	0.70	14.94	3.95

Furthermore, Figure 5-14 shows how fixing a lower target failure rate involves a global reduction in q_{RT}, since the minimum values in Table 5-7 significantly drop below the unit, reaching a value of 0.53 for 2-storey DCM. Additionally, no relevant differences have been observed between all the shear wall buildings realised with DCH compared to the DCM ones. In general, the two fixed levels of safety could be achieved by shear wall archetypes adopting seismic design forces lower than or almost equal to those provided by the Code. In detail, focussing on the mean values reported in Table 5-7, the worst performance occurs for the 6-storey configurations, which has a minimum mean equal to 3.95.

The relationship between q_{RT} and the seismic hazard is highlighted by means of the maps in Figure 5-15, which represents q_{RT} values for all the Italian municipalities given a target of $\lambda_{RT} = 2 \cdot 10^{-4}$. In detail, the colouring of the maps clearly shows how q_{RT} is higher in low-hazard zones (e.g. the northwest regions), while it has an opposite trend with increasing site seismicity. Furthermore, the colour scale has been centred at the q_{NTC} value, in order to highlight the areas requiring the use of seismic design forces higher (low values of q_{RT}) or lower than those provided by the Code. Specifically, most of the municipalities in the 2-storey condition fall in the "higher" case, while this result is changed in the 4- and 6-storey ones, even if none of them is predominant.

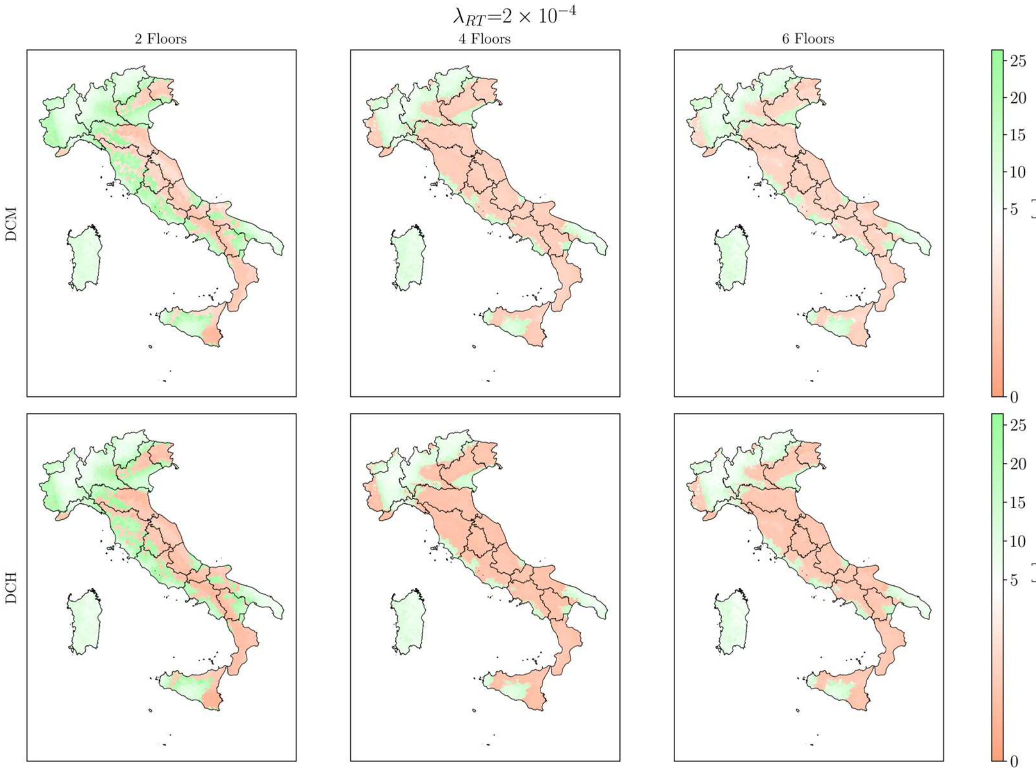

Figure 5-15 Italian maps of reliability-targeted factors q_{RT} – Shear Walls

The effective partition of q_{RT} between the municipalities is shown in Figure 5-16, which supports the outcomes of the previous maps, as none of the categories exceeds 65% of the municipalities. Moreover, the reverse distribution is emphasised according to the number of storeys. Namely, the predominance of the "higher" category occurs in the 2-storey buildings, while the 6-storey ones reach the maximum percentage of municipalities needing a lower value of seismic design action.

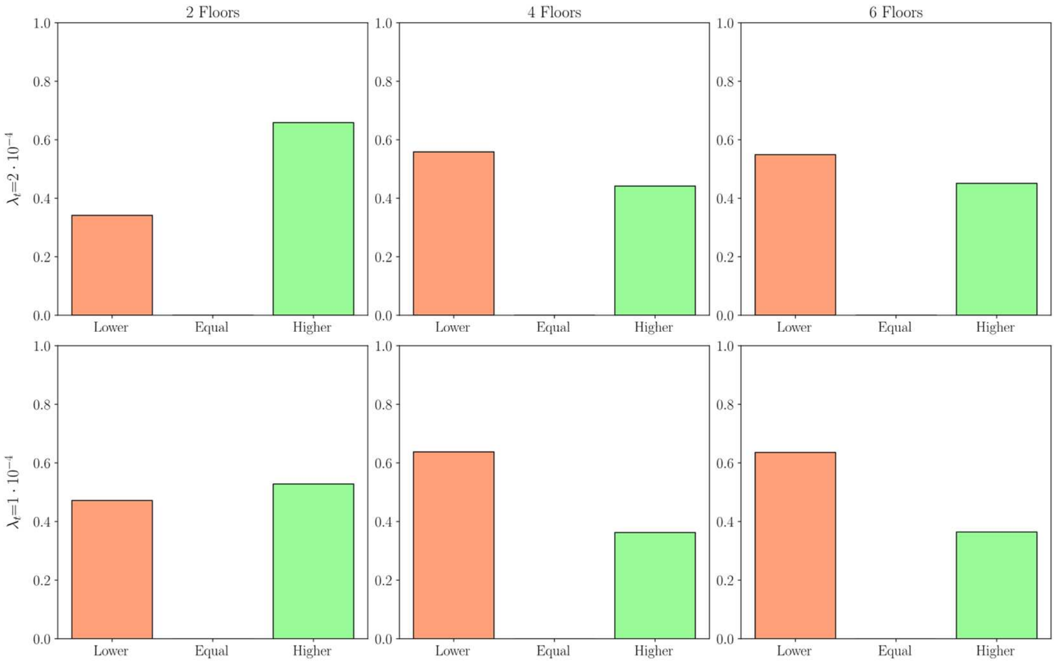

Figure 5-16 Bar chart of q_{RT} *– Shear Walls*

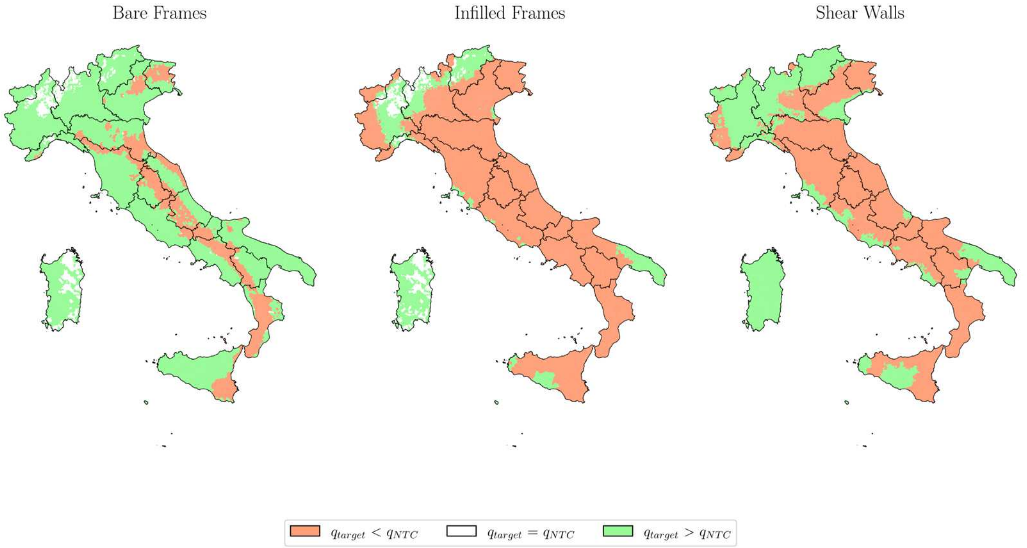

Figure 5-17 Italian Maps q_{RT} *– comparison – 6-storey DCM*

Moreover, the spatial distribution of q_{RT} has been compared to those of the frames analysed previously, considering both the bare and the infilled cases. To this end, Figure 5-17 shows the q_{RT} maps of 6-storey buildings designed according to the DCM prescriptions. Hence, the better performance of bare frames is marked by the predominance of green-coloured sites, while infilled frames seem to need the adoption of the lowest reduction coefficients.

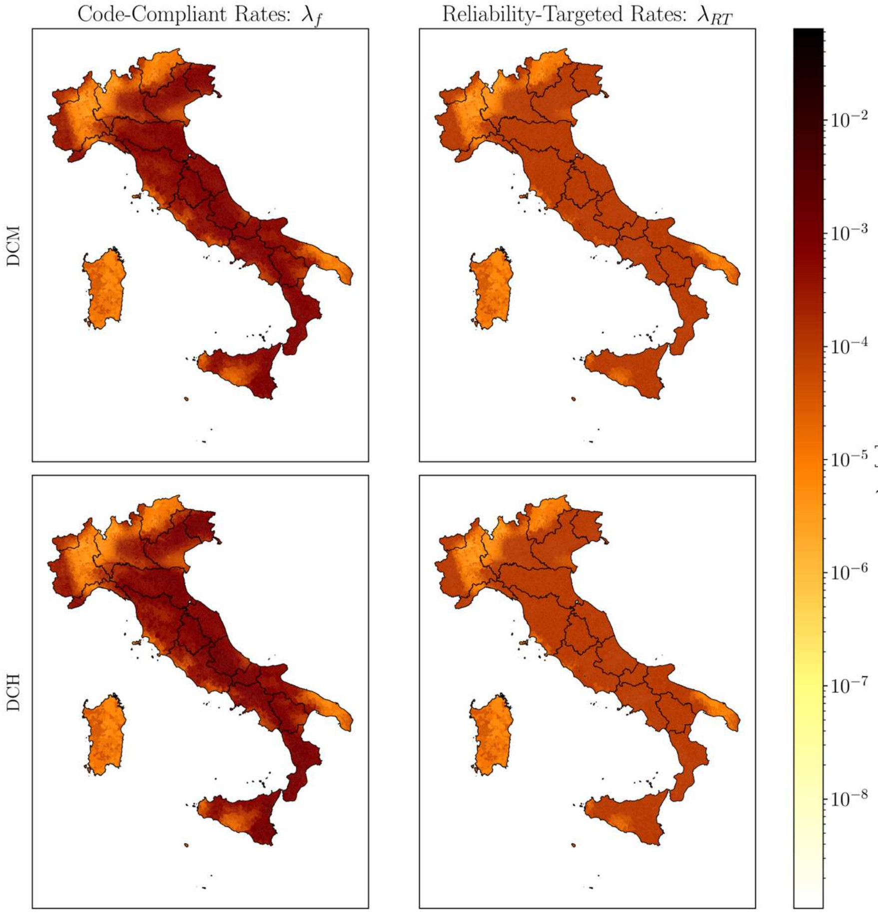

Figure 5-18 Failure rates comparison: code-compliant vs. reliability-target – Shear Walls

The spatial repartition of the behaviour factor is strictly related to the effective seismic failure rate achieved by adopting the developed approach, as shown in Figure 5-18. Namely, the exact achievement of the threshold value is ensured in the zones where q_{RT} is lower than q_{NTC}, while it could not be guaranteed in the opposite. The latter condition is appropriate for low-hazard sites because of the *hazard dependency* of the code approach, which leads to safer code-compliant solutions with the decrease of seismicity. At the same time, these buildings are detailed with minimum requirements, which act as reliability constraints and limit the maximum failure rate achievable. In other words, failure rates of low-hazard sites are not affected by the behaviour factor when trying to reduce their safety because their details remain unchanged.

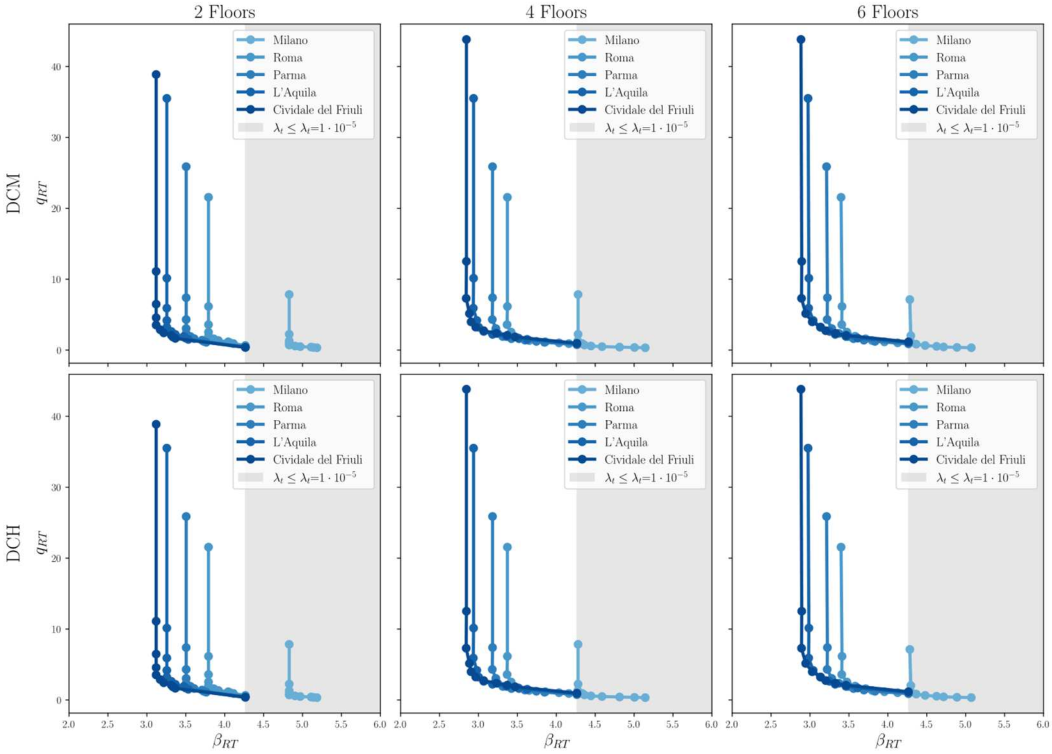

Figure 5-19 Curves q_{RT}-B_{RT} – Shear Walls

As a consequence, harmonisation of seismic reliability seems to be feasible only at hazardous sites. This result is emphasised in Figure 5-19, where the curves B_{RT}-q_{RT} show a vertical horizontal threshold at their left end, indicating a lower limit of the reliability index. For instance, the curve of the lowest hazard site (i.e. Milano) in the 2-storey case is limited to a range of 4.75-5.25, thus it is not possible to reach the desired failure rates. Moreover, the results obtained in Section 4.4 showed that the reliability decreased with the number of storeys, hence the aforementioned effect is mitigated, and this is demonstrated by the reduction in the scatter between the curves. In other terms, it is not possible to achieve the objective of a uniform-reliability solution without modifying the minimum-requirements criteria. Furthermore, another limitation lies in the upper bound of the curves as their right end tends to zero values, and this represents a physical limit that could be overcome only by changing the structural scheme.

5.5 COST-EFFECTIVENESS ANALYSIS OF RC FRAMES

A subsequent investigation consists of evaluating the cost-effectiveness of the different designed prototypes. In this way, the seismic reliability could be related to the inherent structural cost.

As a consequence, a procedure capable of computing the cost of the structural elements of each designed structure for the analysed building topologies has been developed. The evaluation focusses only on the cost associated with structural elements involved in the seismic design process, which are directly affected by seismic design actions, while all nonstructural cost items could be considered as constant factors. This investigation is performed considering the tridimensional configuration of structures and every cost item includes the material one plus all additional entries, such as installation and transportation. All the items are referred to a single regional price list to ensure a uniform and consistent evaluation.

The global cost computation for frame buildings implies the evaluation of the total volume of concrete and the mass of steel bars. Therefore, a different approach has been implemented for longitudinal and transverse reinforcements. In detail, the length of the longitudinal bars has been determined from the envelopes of the bending moments and considering the proper anchoring length provided by Code's prescriptions, while the diameters of the rebars result from the design phase. On the other hand, the number of transverse reinforcement ties was obtained by properly determining the extension of the critical length. These steps have been developed for both beam and column rebars.

First, the cost analysis has been applied to the code-compliant frames to evaluate how the code-conforming design process affects the related construction cost. As expected, there is a clear trend of global cost as a function of elastic spectral acceleration. To this end, Figure 5-20 shows how the expenses increase depending on the intensity of the design seismic action. This behaviour is more marked by the rising number of floors and, in particular, for the class of medium ductility. This could be ascribed to the lower behaviour factor required by the code, which implies higher seismic design forces that lead to larger sizing of concrete sections.

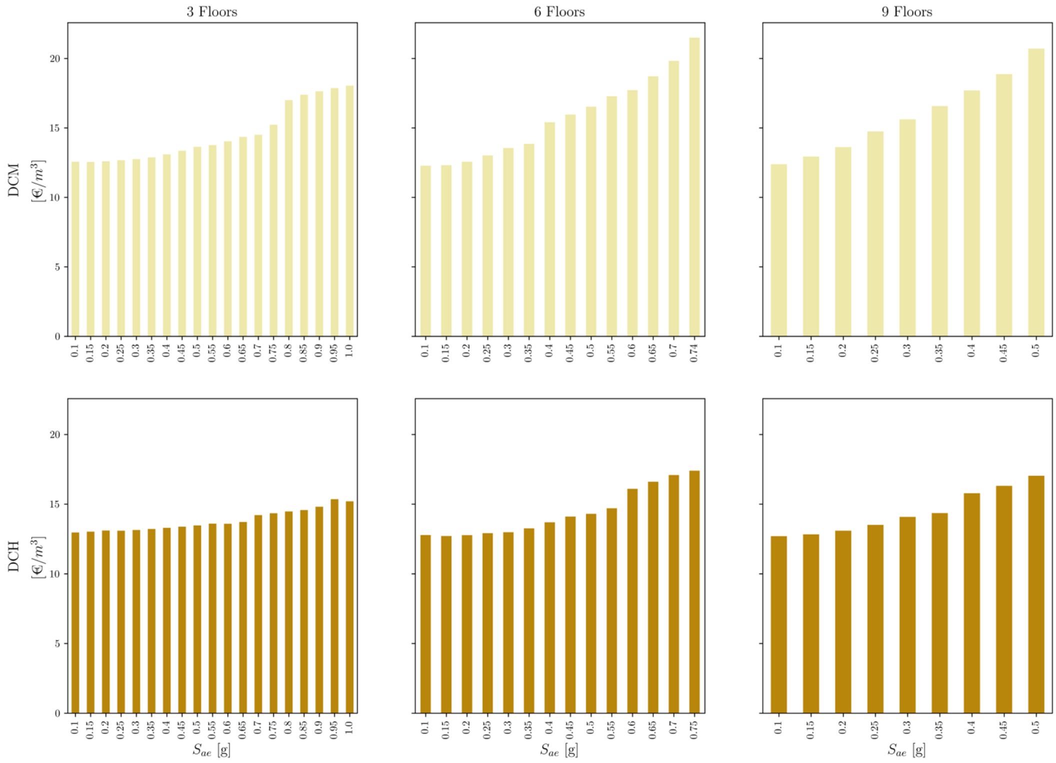

Figure 5-20 Cost variation of code-conforming frames

As a consequence, the trend of construction cost follows a similar path of code-conforming failure rates, which means that there is also a clear connection between cost and seismic hazard of the sites. To achieve this, a series of cost-effectiveness maps of the Italian territory are presented in Figure 5-21 for the layouts of all the analysed frames. Therefore, the colour variation of these maps recalls the one depicted by the seismic hazard one (Figure 2-18). In other words, the construction cost ranges from a value of around 12.5 €/m^3 in low seismicity sites to a value of around 20.5 €/m^3 in hazardous ones. Moreover, Figure 5-21 highlights an evident gaining in global cost with the increasing number of floors, as the green becomes the predominant colour in the map moving from the 3-storey layout to the 9-storey one for the DCM case.

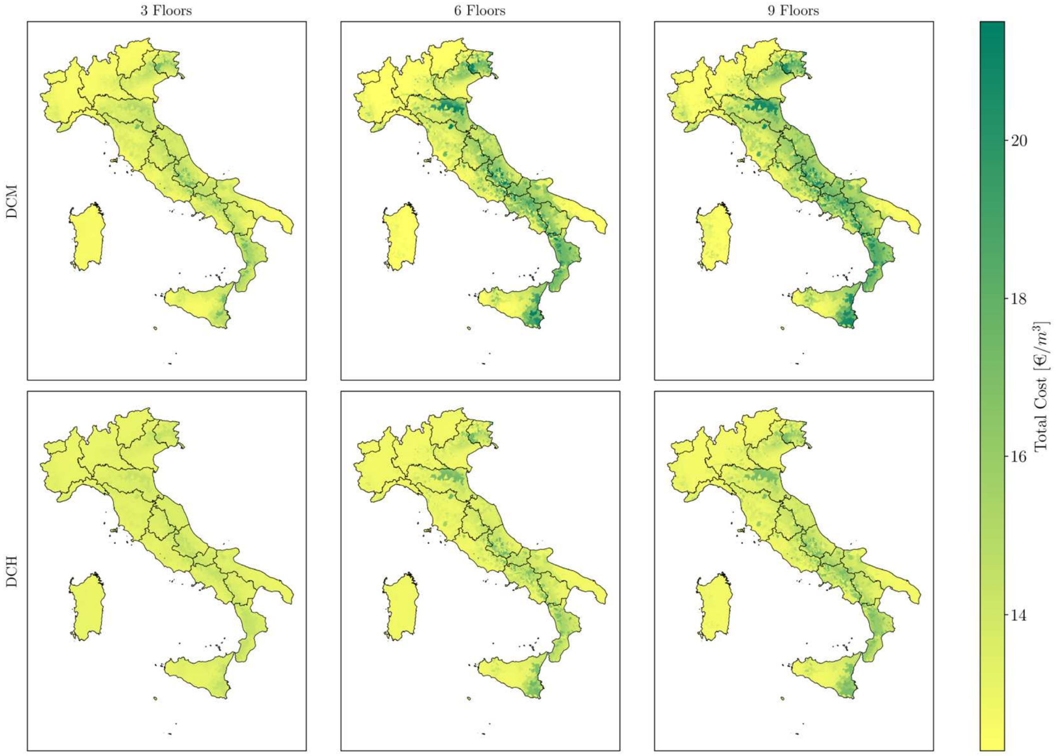

Figure 5-21 Total cost maps for code-conforming frames

As mentioned before, the lower value of the behaviour factor of DCM class design leads to a greater amount of construction material, thus a cost-effectiveness analysis between the two ductility classes has been performed to emphasise this implication. The results are reported in Figure 5-22, where the more convenient ductility class has been indicated for each Italian municipality. The aforementioned effect of the behaviour factor is clearly marked with increasing of floors, as for the 9-storey layout most of the sites fall into DCH class.

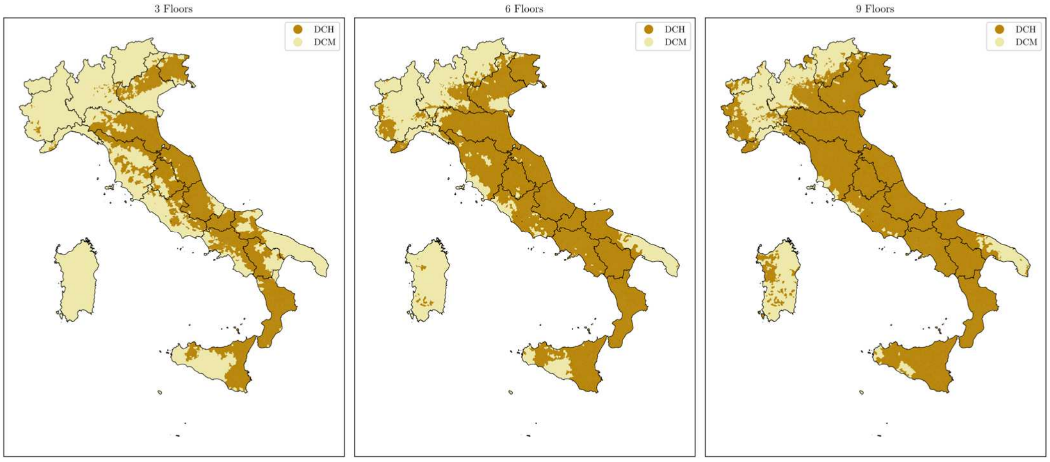

Figure 5-22 Cost-effectiveness maps for code-conforming frames

At this point, the reliability-targeted design approach has been introduced in the cost-effectiveness assessment. In this way, it would be possible to assess the impact of this philosophy on the structural cost of newly designed structures.

First of all, cost analyses have been performed for the five specific municipalities introduced in Table 5-2. In detail, the global cost has been calculated for some different levels of seismic reliability, expressed in terms of the reliability index B_{RT}. The derived curves, reported in Figure 5-23, are characterised by a proportional tendency, and as expected, higher levels of seismic safety imply major expenses. Each curve shows a marked vertical pattern, which means that it is necessary to incur in a significant spending to achieve a higher level of reliability. Additionally, as revealed in B_{RT}-q_{RT} curves, reachable values span in limited ranges, leading to a clear scatter among different sites.

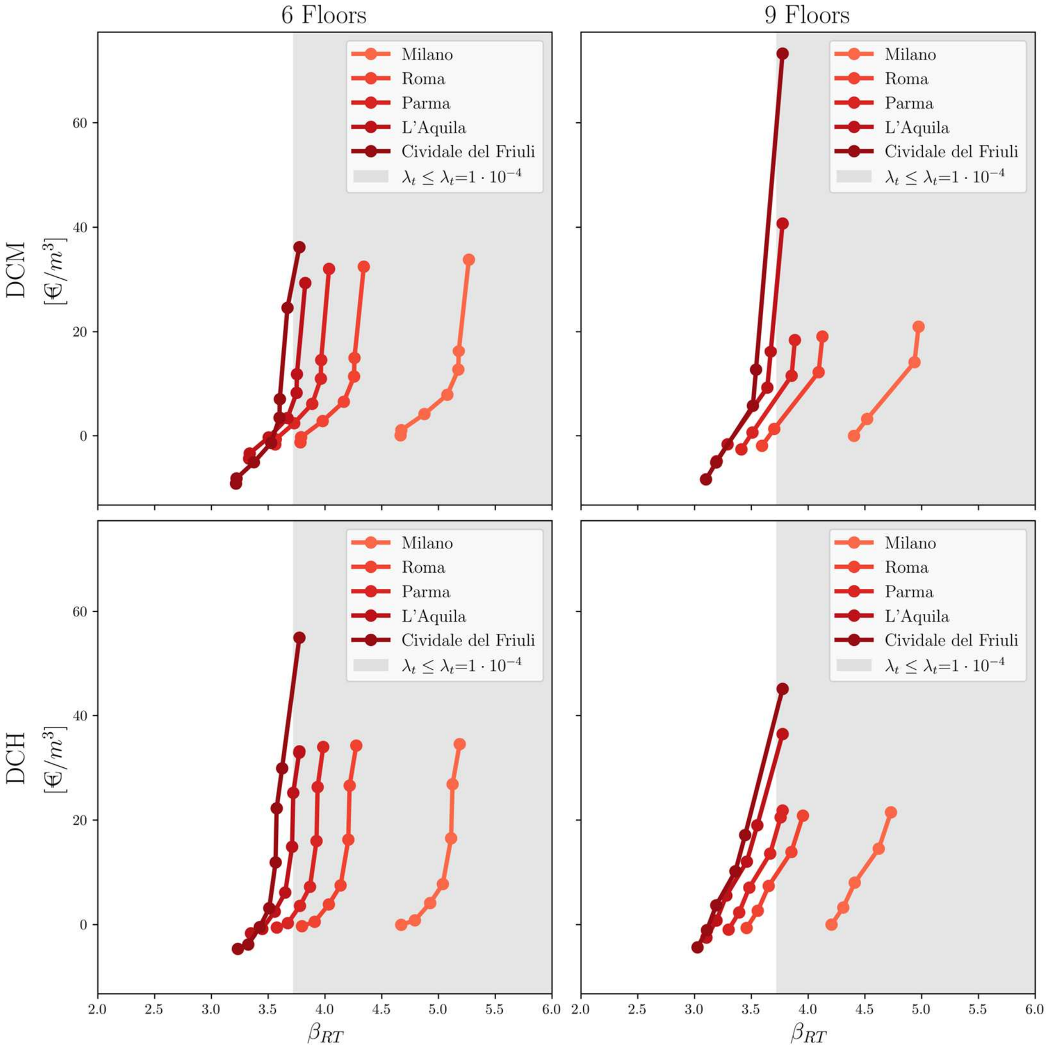

Figure 5-23 Reliability targeted cost curves for specific sites - frames

Consequently, the structural cost of reliability-targeted prototypes has been evaluated for Italian municipalities to stress the differences between code-conforming ones. The analyses have been performed for two target seismic reliability failure rates equal to $2.0 \cdot 10^{-4}$ and $1.0 \cdot 10^{-4}$. First of all, Figure 5-24 shows the Italian territory maps for the 6-storey configuration when fixing a desirable failure rate equal to $1.0 \cdot 10^{-4}$. Hence, the highest expenses occur in the reliability-targeted maps, which means that this level of safety requires more expensive structures. However, the spatial distribution of cost values is strictly related to the seismic hazard, and this could portend that low hazard sites could revelas a cost convenience compared to the hazardous zones.

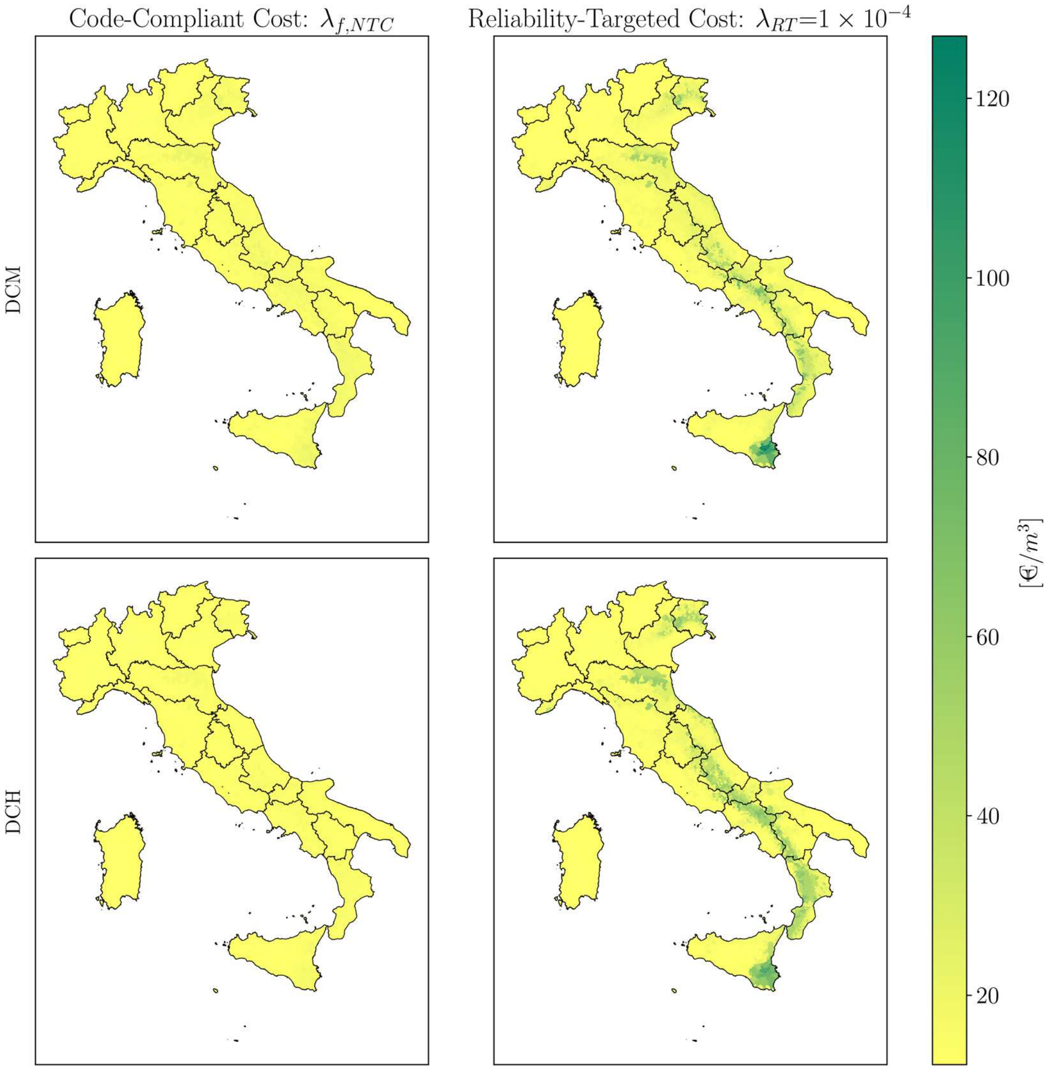

Figure 5-24 Italian cost maps for frames: code-compliant vs reliability-targeted

The global results are summarised in Table 5-8, which displays the overall minimum, maximum and mean values of total cost among the Italian municipalities. The obtained results globally increase according to the number of floors. This trend is confirmed by observing the mean values, which range from 13.52€/m^3 to 24.46€/m^3 for 3-storey and 9-storey, respectively. On the contrary, there is no significant discrepancy in terms of ductility class, except for the 9-storey configuration, which exhibits a slighter gap. Moreover, the proximity of the minimum and mean value for 3-storey frames could be ascribed to the reliability-targeted behaviour factor reported in Table 5-8, which is on average appreciably higher than those proposed in the Code. Hence, most of the sites could be designed employing low values of the seismic design action, which results in inexpensive buildings. Additionally, Table 5-8 shows that q_{RT} values are inversely proportional to the number of floors, and this is confirmed by Table 5-8, where the gap between mean and minimum cost is higher in 9-storey layouts than in 3-storey ones.

Table 5-8 Reliability-targeted cost for frames

Case	$\lambda_{RT}=2\cdot10^{-4}$ [€/m^3]			$\lambda_{RT}=1\cdot10^{-4}$ [€/m^3]		
	Min	***Max***	***Mean***	***Min***	***Max***	***Mean***
3-DCH	12.93	24.39	12.96	12.93	40.72	13.52
3-DCM	12.57	22.34	12.58	12.57	40.88	13.05
6-DCH	12.56	55.66	13.49	12.56	94.50	18.07
6-DCM	12.23	48.82	13.43	12.23	126.95	16.66
9-DCH	11.90	48.29	18.49	11.90	67.63	24.46
9-DCM	11.74	60.46	15.24	11.74	120.73	21.23

For this reason, further development consists of computing the cost differential between the code-conforming and the reliability-targeted solution for each municipalities given a target seismic failure rate. In this way, it is possible to locate areas that would entail an increased cost when changing the design paradigm. From another point of view, these data could be adopted to formulate a government incentive aimed at ensuring a uniform level of seismic reliability for recently built structures capable of reducing losses in future earthquake events. These outcomes are reported in Figure 5-25, which shows the cost variation for the three elevation configurations.

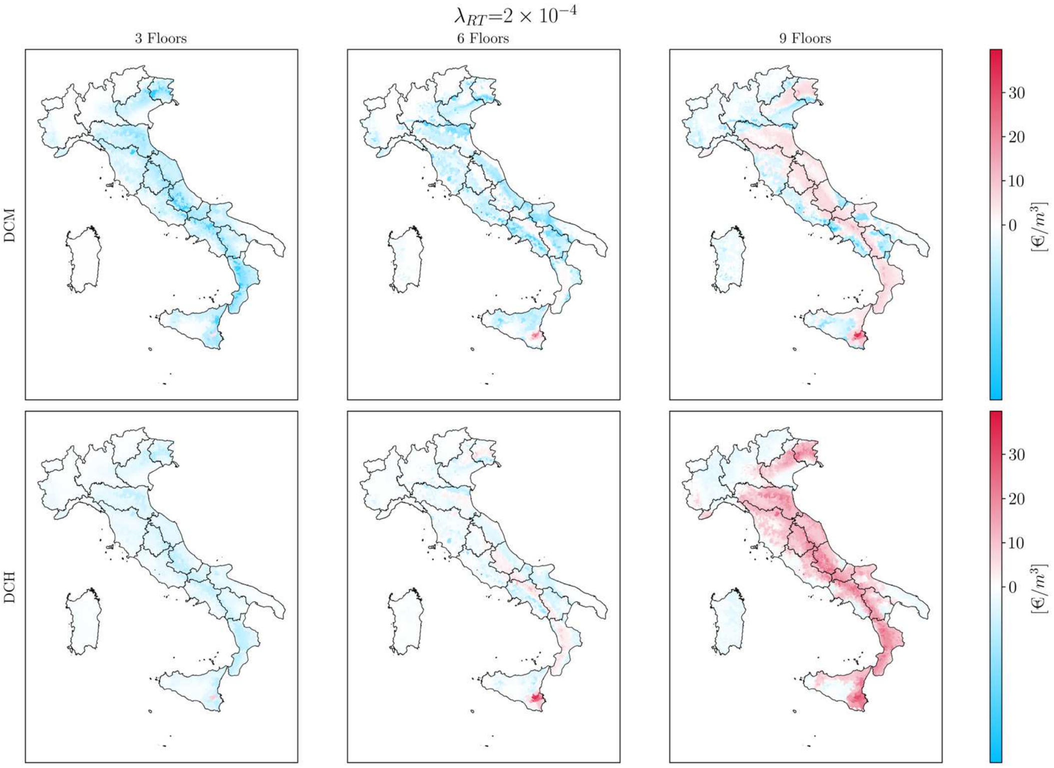

Figure 5-25 Reliability-targeted maps of cost for frames

6 SEISMIC RISK OF CODE-CONFORMING RC BUILDINGS

Previous Chapters have focused on the assessment of the structural safety of code-compliant buildings, but the quantification of their performance could be also evaluated in terms of consequences due to earthquake events. For this reason, the present Chapter aims to assess the seismic risk of newly designed code-compliant residential buildings. Hence, the same structural archetypes described in previous Chapters will be adopted for the risk analyses. In this way, it could be possible to estimate the impact of the *hazard-dependent* seismic reliability of code-compliant structures when including loss metrics.

6.1 METHODOLOGY

The quantification of the seismic risk of buildings could be carried out by means of the PEER PBEE methodology [5] described in Section 0. The fourth step of this probabilistic framework consists of the execution of a loss analysis, which leads to the estimation of the exceedance frequency of various levels for some specific decision variables, for example, initially identified as 3D's (i.e. death, dollars and downtime) [96]. The implementation of this process is a highly demanding task, as it requires combining extensive computational analyses with fully probabilistic steps. Therefore, this poses a problem for its application in common design practise, and some simplified approach has been proposed [97] [98]. In the Italian context, the practical characterisation of seismic risk has been strongly influenced by the introduction of the guidelines commonly named 'sismabonus' [99], which provide the ranking of the vulnerability of existing buildings using expected annual loss (EAL) as a metric, and this law aims to enable tax relief related to seismic structural retrofit interventions. Specifically, this approach is based on the computation of two main quantities: the IS-V index, which is expressed in terms of the ratio between the maximum peak ground acceleration bearable by the assessed structure (PGA_c) and the one adopted for designing a new equivalent one ($\mathrm{PGA_d}$). As mentioned, the second metric is the EAL, which was introduced in the FEMA P58-5 Guidelines [20], and it is determined by linking a fixed reconstruction costs ratio to the rate of exceedance of six limit states, which are consistent with those provided by the current Italian building code. Hence, the seismic performance of the structures is evaluated through a letter-based score, which goes from the most desirable A+ to the worst named G. Hence, this method is based on large simplifications that could lead to some inconsistency in the assessment of seismic risk [100]. For instance, reconstruction loss ratios have been calibrated from data collected in surveys after the 2009 earthquake in L'Aquila [101], which means that they are dependent on the judgment of surveyors, while the original methodology is based on a numerical analysis of the evolution of the damage.

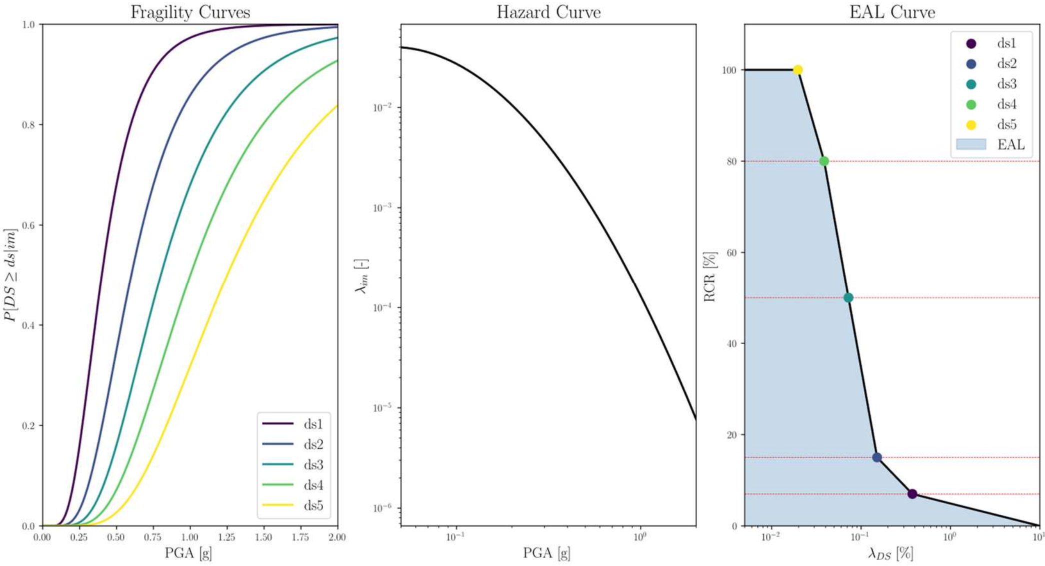

Figure 6-1 Methodology for risk assessment

The present work adopted the basic workflow of [99] to derive seismic risk maps of code-conforming structures at the municipal level, as reported in Figure 6-1. Hence, the previous methodology has been slightly modified to properly account for the outcomes of the seismic probabilistic analysis. Specifically, the fifth reconstruction cost ratios (i.e. 7-15-50-80-100%) have been linked to the seismic failure rates of the damage states adopted for the vulnerability assessment, while the first point at initial damage with an exceedance frequency (λ_{DS}) of 10% and 0% of reconstruction cost ratio (*RCR*) has been established following the guidelines. Thus, the EAL is determined by integrating the area under the curve in the plan λ_{DS}-*RCR*. Adopting seismic failure rates allows for consideration of both the sources of uncertainty in the vulnerability assessment and the effective hazard curve. The subsequent sections will present the results of this process for the three structural resisting schemes investigated in this work.

6.2 SEISMIC RISK MAPS OF BARE FRAMES

This section will focus on the assessment of the seismic risk of code-conforming bare frames, whose features are presented in Section 2.1. As a consequence, the results of Section 2.4, in terms of seismic failure rates, have been adopted to create the curves λ_{DS}-*CRR* of every Italian municipality, which allows one to calculate their expected annual loss (EAL). For the sake of clarity, the curves of five sites with increasing seismicity are shown in Figure 6-2, and their associated EALs are reported in Table 6-1. That is, the one with the lowest hazard is Milan, while the one with the highest is Cividale del Friuli. Thus, Figure 6-2 shows a clear relationship between the seismicity and the computed risk indicator, as the area below the curves increases according to the hazard. This is further highlighted in Table 6-1, where the EAL grows according to the columns, given the row. Additionally, it shows how there is no clear relationship between the risk metric and the number of floors in buildings, as the values of each column are almost constant.

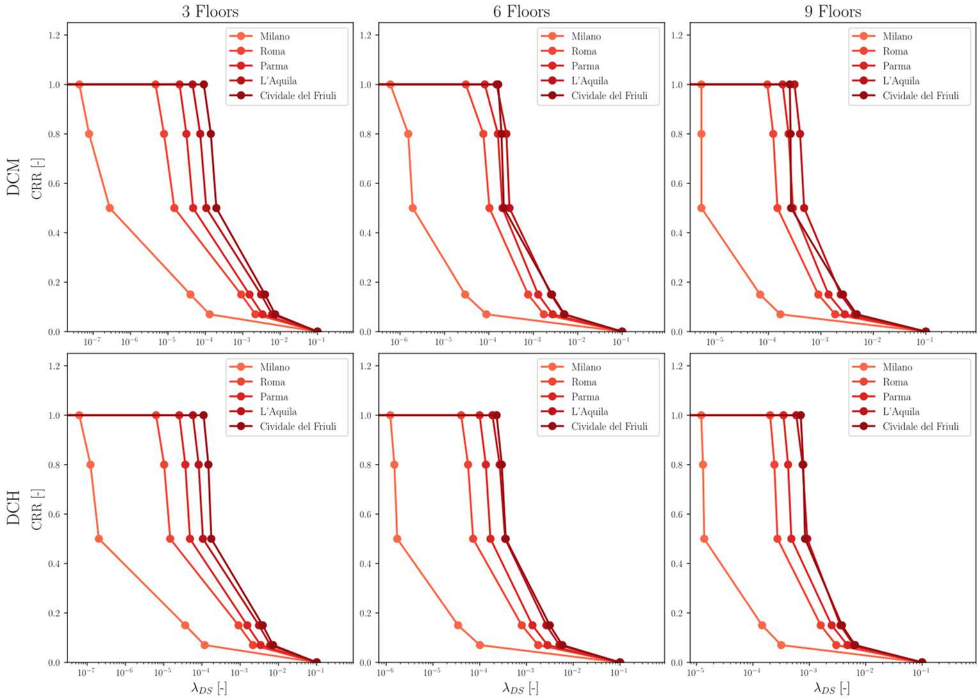

Figure 6-2 EAL curves - Bare frames

Table 6-1 EAL values - Bare frames

Case	EAL [%]				
	Milano	**Roma**	**Parma**	**L'Aquila**	**Cividale Del Friuli**
3-DCH	0.352	0.386	0.411	0.469	0.498
3-DCM	0.352	0.387	0.410	0.468	0.501
6-DCH	0.352	0.385	0.410	0.465	0.483
6-DCM	0.351	0.385	0.410	0.457	0.458
9-DCH	0.356	0.424	0.469	0.527	0.534
9-DCM	0.353	0.392	0.419	0.464	0.461

As a consequence, the relationship between the site's hazard and the EAL has been further investigated by extending the calculation to all municipalities. Figure 6-3 shows that this trend is common for all the municipalities, since the Pearson's correlation coefficient ρ confirms a strength dependency between these two parameters ($\rho \geq 0.94$). Furthermore, the scatter plot detects a different dispersion among the different cases, which could be ascribed to the inherent seismic response of the structures.

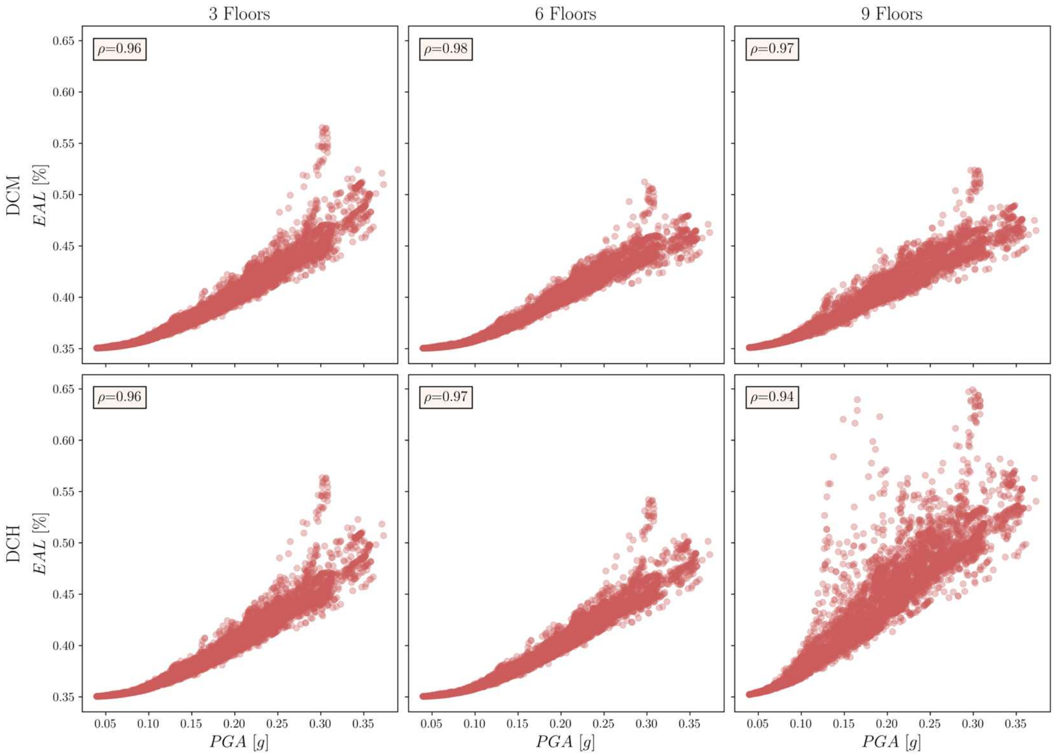

Figure 6-3 Correlation PGA-EAL – Bare Frames

The results show a lower range of variation, which is highlighted by the boxplots in Figure 6-4 and the extreme values reported in Table 6-2. More in detail, the minimum value is equal to 0.35%, while the maximum value is about 0.65%, determining a scatter of 0.3%. In addition, the performances of DCM and DCH frames are equivalent, as they display a similar trend for all layouts.

Table 6-2 EAL extreme values – Bare Frames

Case	**EAL [%]**		
	Min	***Max***	***Mean***
3-DCH	0.35	0.56	0.39
3-DCM	0.35	0.57	0.39
6-DCH	0.35	0.54	0.39
6-DCM	0.35	0.51	0.39
9-DCH	0.35	0.65	0.42
9-DCM	0.35	0.52	0.39

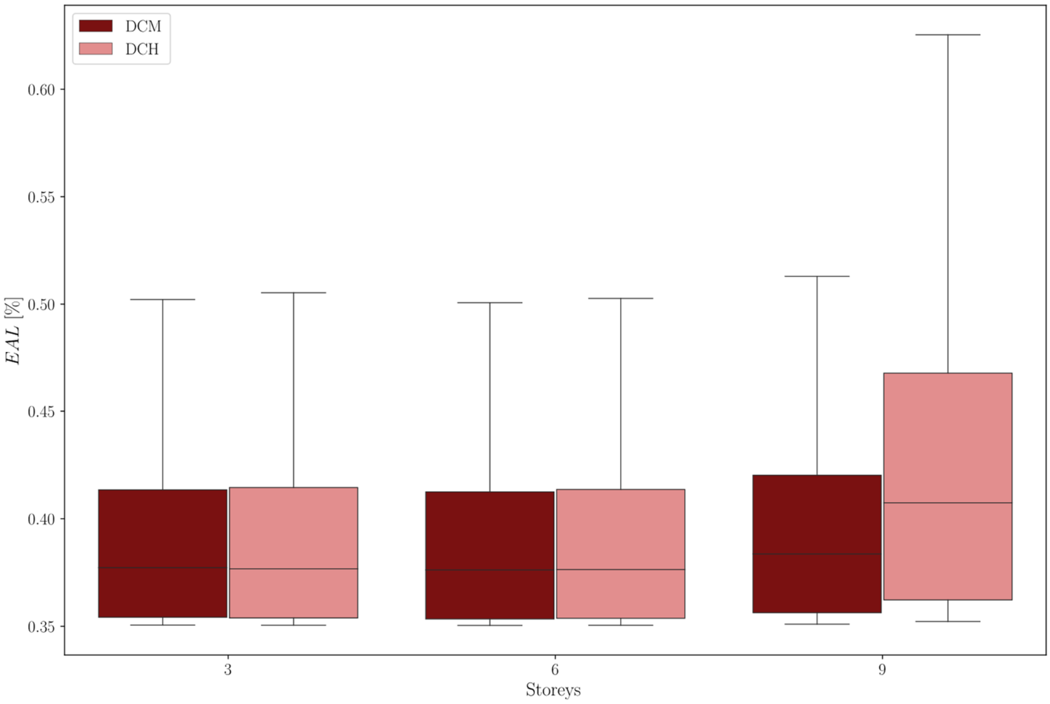

Figure 6-4 EAL ranges - Bare Frames

At this point, it is possible to derive seismic risk maps of the code-conforming bare frames. Figure 6-5 shows the strong correlation between the seismic hazard map (Figure 2-18) and the risk ones. This trend is noticeable for the 9-storey configuration, which registers the higher values of EAL. For example, some of the areas with the minimum EAL are located in northwest Italy, which is the zone with the lowest hazard intensity. In contrast, high seismic risk values occur in the regions of central Italy, which is the area characterised by the last strong earthquake events. Furthermore, all municipalities have been classified according to the classification proposed by the Italian guidelines. As shown in Figure 6-6, most of the city belongs to the safest condition, that is, the A+ class. However, the identified dependency on hazards causes a downgrade in municipalities located at high-seismicity sites, especially in the 9-storey condition. This phenomenon should not be underestimated, as the 'safe' condition is strictly related to established criteria.

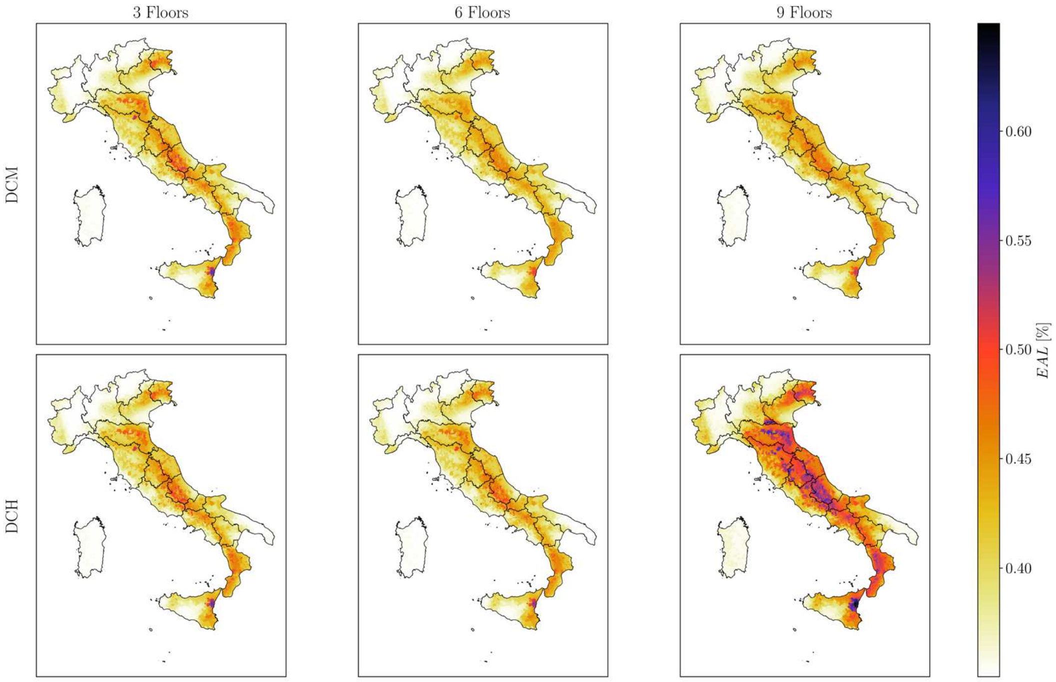

Figure 6-5 Seismic risk maps of code-conforming Bare Frames

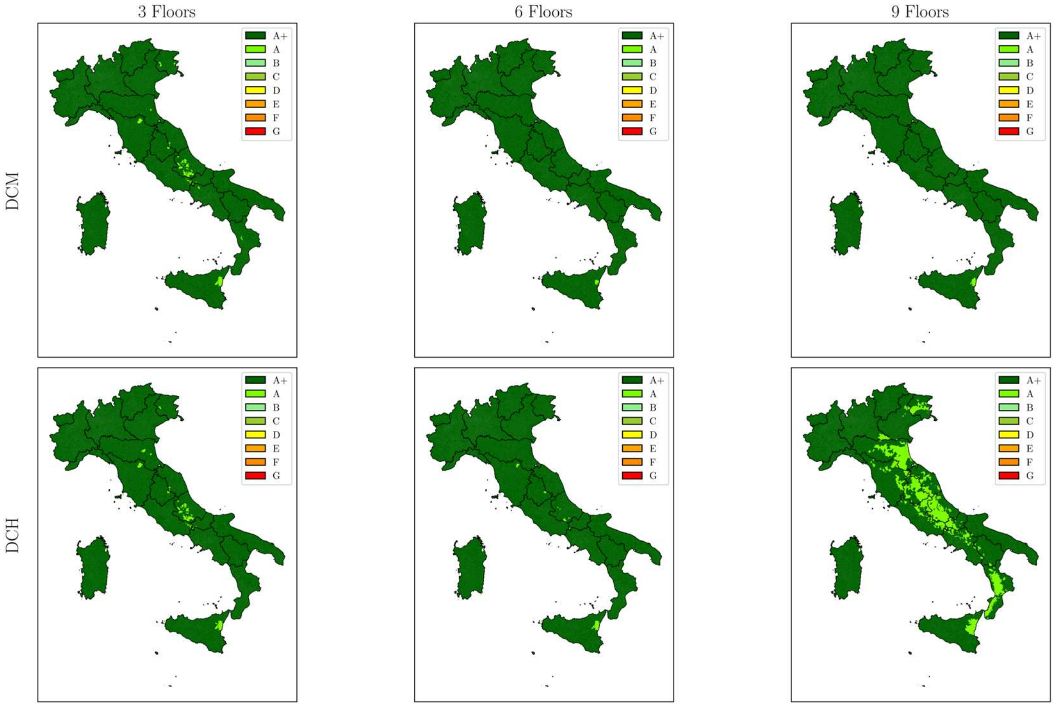

Figure 6-6 EAL ranking - Bare Frames

6.3 SEISMIC RISK MAPS OF INFILLED FRAMES

The assessment of the seismic risk of the infilled frames is carried out with the same workflow as that used for the bare ones. It is worth recalling that the infilled frames differ from the bare cases only in terms of vulnerability assessment, as the stiffening contribution has been explicitly considered due to the infill panels. The discrete results in terms of EAL for the five sites are presented in Figure 6-7 and in Table 6-3.

Table 6-3 EAL values – Infilled Frames

Case	**EAL [%]**				
	Milano	**Roma**	**Parma**	**L'Aquila**	**Cividale Del Friuli**
3-DCH	0.354	0.450	0.515	0.647	0.709
3-DCM	0.352	0.387	0.410	0.468	0.501
6-DCH	0.362	0.532	0.624	0.742	0.713
6-DCM	0.362	0.481	0.544	0.653	0.607
9-DCH	0.357	0.465	0.530	0.646	0.605
9-DCM	0.357	0.447	0.500	0.586	0.540

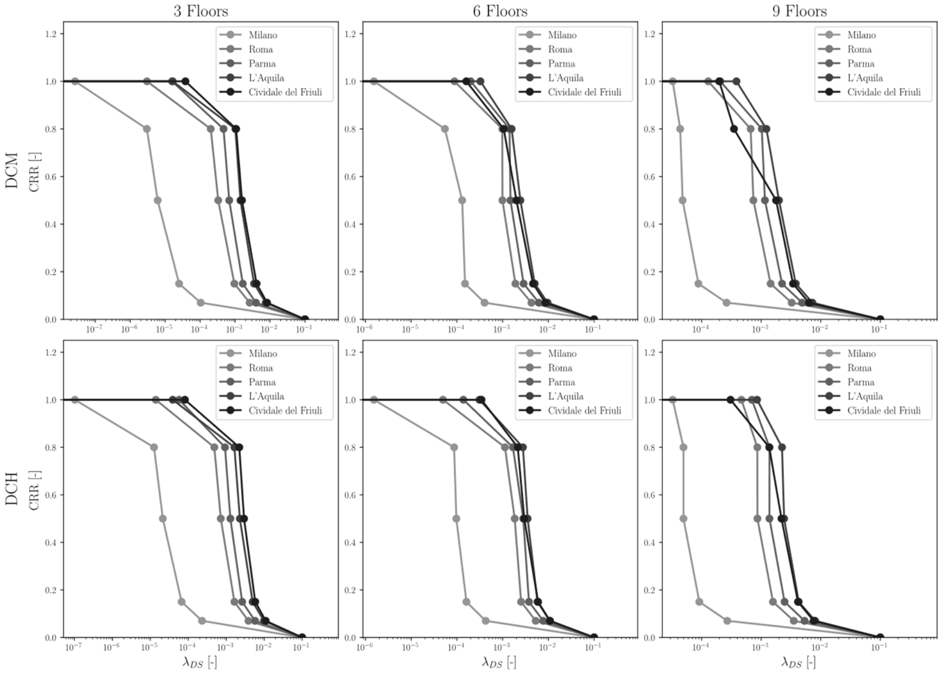

Figure 6-7 EAL curves - Infilled Frames

Figure 6-7 shows the same global trend between the seismic hazard of the site and the determined EAL, since the curves move to the right with increasing municipality's PGA. This trend is globally confirmed in Table 6-3, even if there is an inversion of the EAL between the two hazardous sites for the 9-storey cases. Furthermore, the discrepancy between DCM and DCH performance is appreciable, as when comparing the plots in the same column, a trend shifted to the left is observed. For example, the 3-storey frame located in Cividale del Friuli reaches an EAL of 0.709% and 0.501% for DCH and DCM, respectively. This is due to the greater impact of infills on DCH frames' seismic behaviour, caused by the higher behaviour factor q_{NTC} that led to lower sections, which results in lower reliability. The proportional relationship EAL-PGA is observed for all municipalities, as shown in Figure 6-8, leading to a minimum Pearson correlation coefficient equal to $\rho = 0.96$ and almost constant for all layouts. In this case, the dispersion of the data is slightly lower than in the bare configuration, highlighting a strong dependency.

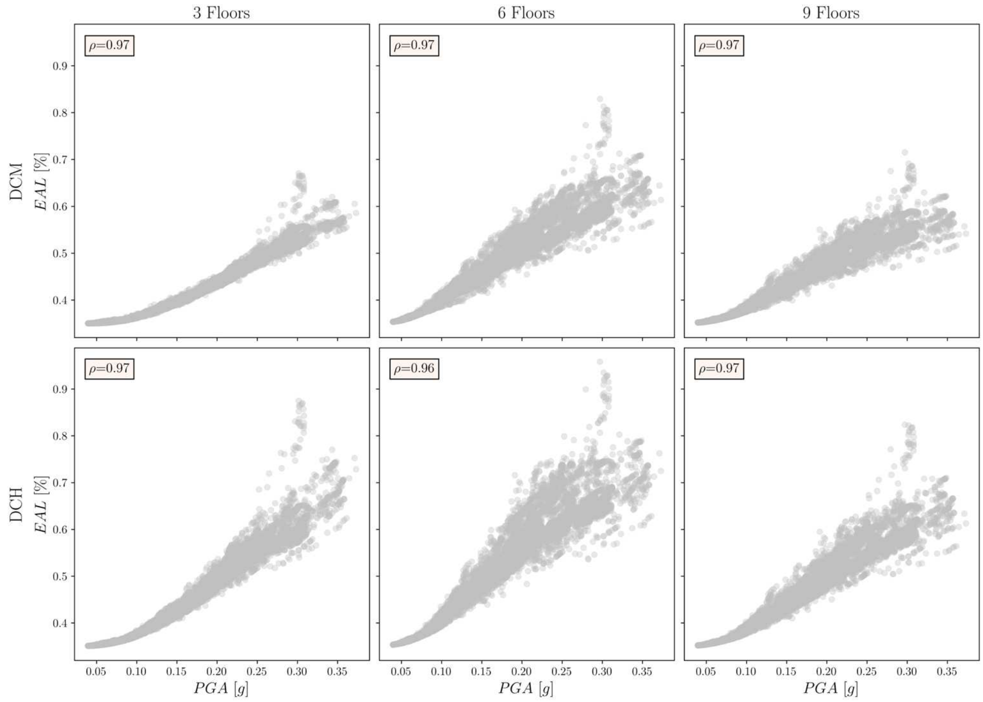

Figure 6-8 Correlation PGA-EAL – Infilled Frames

Furthermore, the infilled data exhibit a wider range of variation than the bare frames, as is highlighted in Figure 6-9 and Table 6-4.

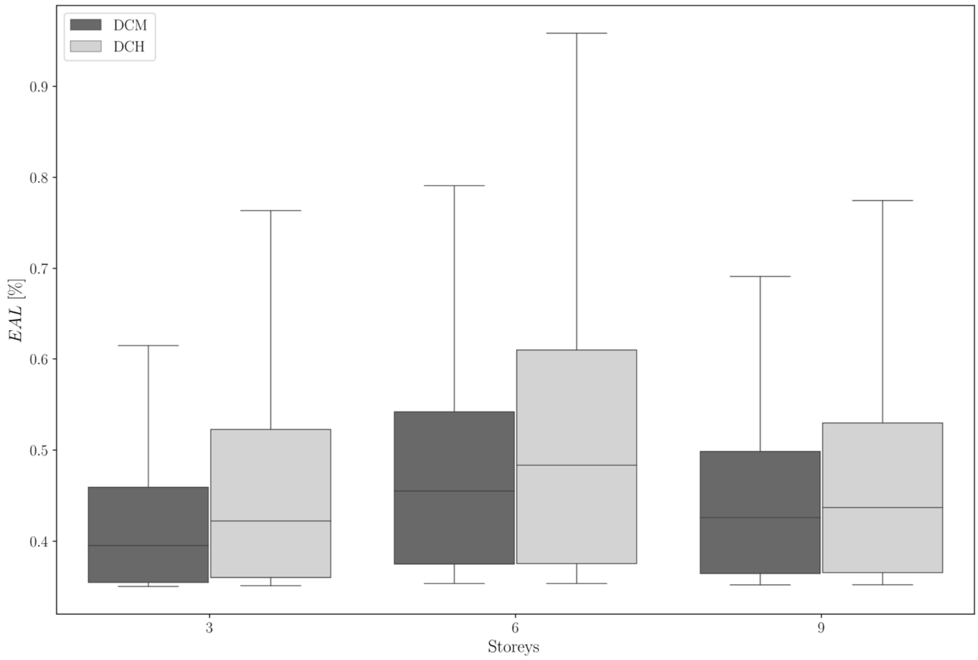

Figure 6-9 EAL ranges – Infilled Frames

Table 6-4 EAL extreme values – Infilled Frames

Case	EAL [%]		
	Min	*Max*	*Mean*
3-DCH	0.35	0.87	0.45
3-DCM	0.35	0.67	0.41
6-DCH	0.35	0.96	0.50
6-DCM	0.35	0.83	0.47
9-DCH	0.35	0.82	0.46
9-DCM	0.35	0.72	0.44

Specifically, the worst performance is encountered for the 6-storey DCH frames, which reach an EAL equal to 0.96%, while a maximum value of 0.87% and 0.82% is attained by the 3- and 9-storey, respectively. In this regard, the extreme values infilled configurations are bounded from 0.35% to 0.96%, while the bare frames range between 0.35% and 0.65%; hence, the formers globally exhibit a higher seismic risk. Furthermore, Figure 6-9 highlights the difference in performance between the DCM and DCH frames, as the range of the former is constantly below the latter.

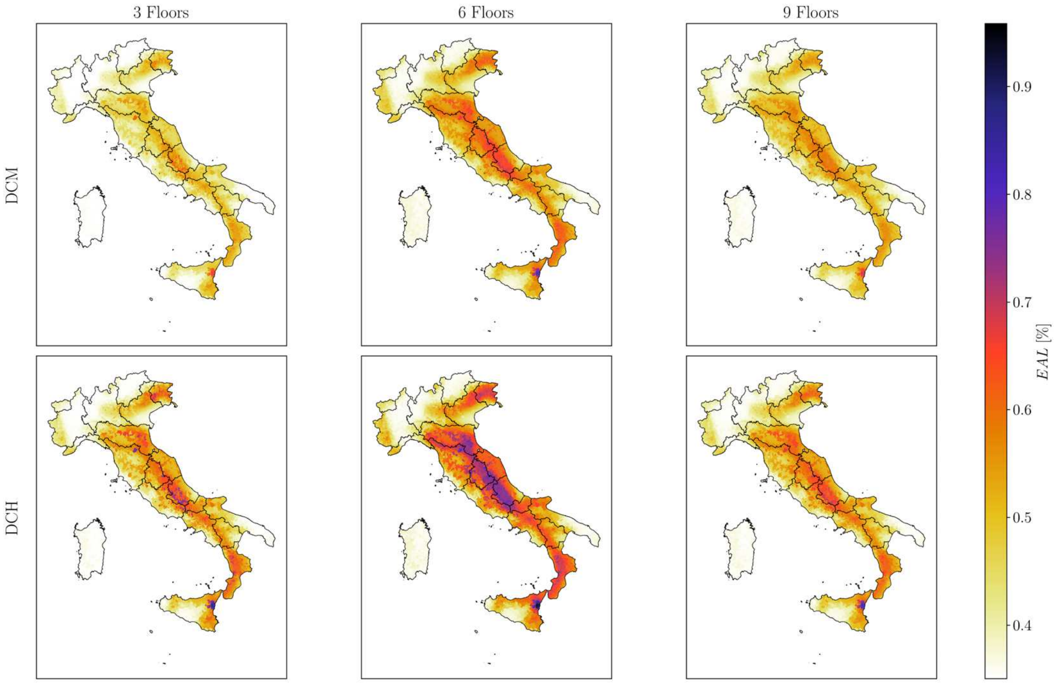

Figure 6-10 Seismic risk maps of code-conforming Infilled Frames

The seismic risk maps of the infilled frames computed for all Italian municipalities are shown in Figure 6-10. This outlines the global proportional relationship between risk and hazard, as shown in Figure 6-5 for bare frames. In this case, the trend is more marked due to the wider amplitude of the EAL ranges in infilled cases. Furthermore, Figure 6-10 shows the different risk among the two levels of ductility, since the maps in second row colour are darker, meaning that DCH experiences higher losses. Finally, the EAL values have been converted to the associated classification provided by the Italian Guidelines. Figure 6-11 demonstrates how most municipalities move from A+ in bare configurations to □ in the infilled ones.

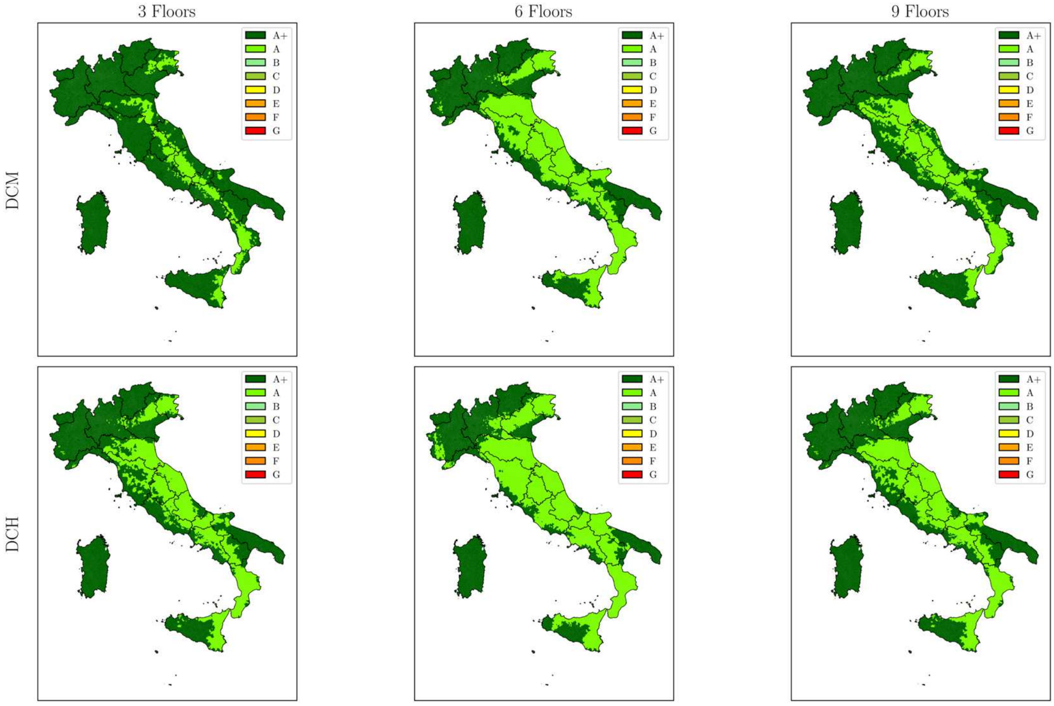

Figure 6-11 EAL ranking - Infilled Frames

6.4 SEISMIC RISK MAPS OF SHEAR WALLS

The prototype buildings adopted for shear walls are fully described in Section 4.1, so the seismic risk analysis carried out here will start from the results of their code-compliant reliability assessment, reported in Section 4.4. Coupling failure rates with a fixed reconstruction cost ratio leads to the acquisition of a series of curves whose area is the seismic risk metric EAL. This step is presented for five sites with increasing PGA, in Figure 6-12. The curves show a significant gap between the site with the lowest seismicity and the others. This is attributed to the extremely low seismic failure rates of code-conforming buildings in low-hazard municipalities, which result in an independent risk in terms of both floor variation and ductility class. It is worth noting that the main contribution in the calculation of EAL for the case of Milano is due to the initial damage state placed at an exceeding frequency of 0.1. This point is a fixed constraint prescribed by the Italian Guidelines, but it is clear that it strongly affects the final risk, since the mean failure rates of the other states of damage are quite lower. However, Figure 6-12 shows an increase in EAL according to the PGA of the sites, while there is a slight inverse trend moving from the DCM to the DCH class, since the curves shift to the left (i.e. decreasing the underlying area).

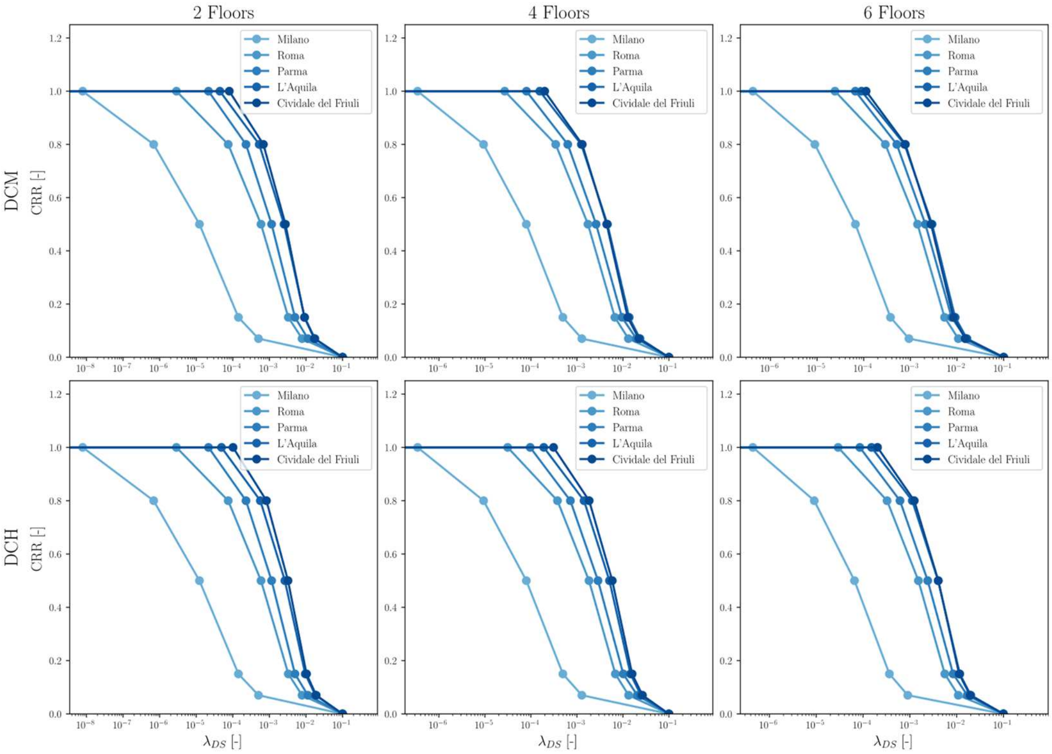

Figure 6-12 EAL curves – Shear Walls

Table 6-5 EAL values – Shear Walls

Case	**EAL [%]**				
	Milano	**Roma**	**Parma**	**L'Aquila**	**Cividale Del Friuli**
2-DCH	0.357	0.500	0.585	0.791	0.842
2-DCM	0.357	0.500	0.585	0.775	0.779
4-DCH	0.373	0.666	0.835	1.052	1.130
4-DCM	0.373	0.658	0.803	1.002	0.968
6-DCH	0.367	0.609	0.751	0.912	0.903
6-DCM	0.367	0.600	0.714	0.783	0.753

This trend is globally described in Figure 6-13, which shows the points PGA-EAL for each municipality. Dependence between the two parameters is evaluated using the Pearson correlation coefficient, which takes a minimum value equal to ρ=0.92. In addition, it is observed that the data of the 4-storey buildings are sparser, while the 2-storey follow a more linear path.

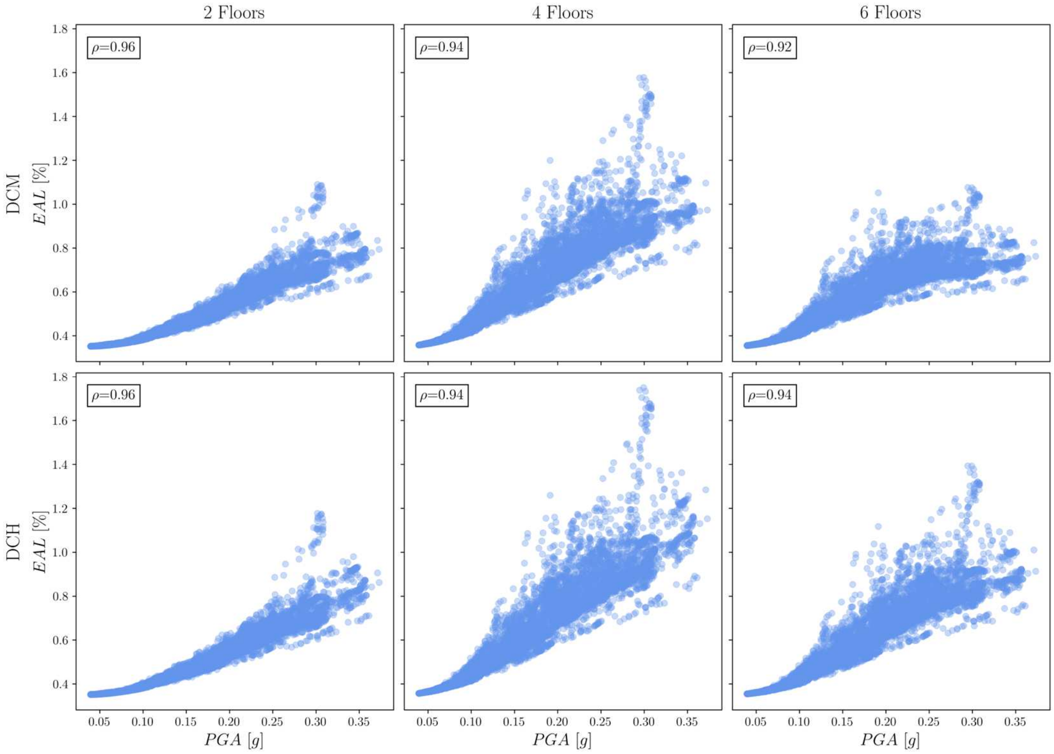

Figure 6-13 Correlation PGA-EAL – Shear Walls

The dispersion of 4-storeys cases is highlighted in Figure 6-14, as the associated boxplot shows an upper skewed trend. On the contrary, the 2-storey cases have a narrow variation range. Furthermore, the performance of the 4- and 6-storey cases differs between the two classes of ductility; namely, the DCH experiences higher EAL, according to what was observed at the discrete level in Figure 6-12.

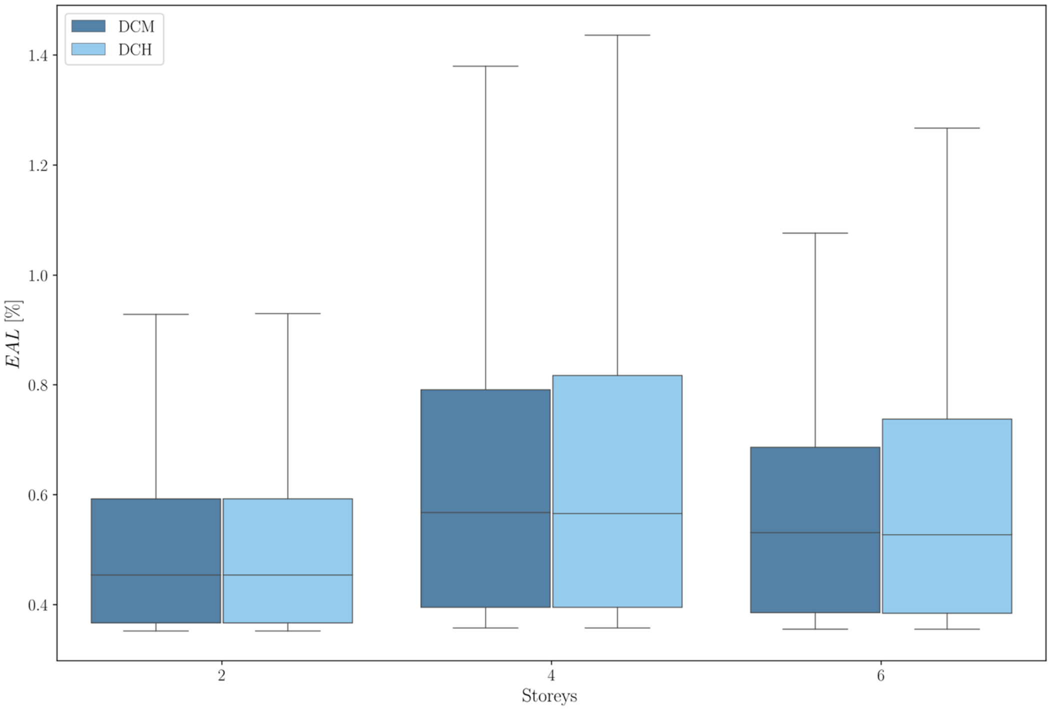

Figure 6-14 EAL ranges - Shear Walls

Table 6-6 EAL extreme values - Shear Walls

Case	**EAL [%]**		
	Min	***Max***	***Mean***
2-DCH	0.35	1.18	0.49
2-DCM	0.35	1.09	0.49
4-DCH	0.36	1.75	0.62
4-DCM	0.36	1.58	0.61
6-DCH	0.36	1.39	0.57
6-DCM	0.36	1.08	0.55

Table 6-6 shows the minimum, maximum, and mean values of the EAL for all the configurations. Thus, in shear wall buildings, the EAL is bounded from 0.35% to 1.75%, which implies that they perform worst among the investigated structural resisting scheme, since for the bare and infilled frame the maximum is equal to 0.65% and 0.96%, respectively. On the other hand, this difference softens when considering the mean values.

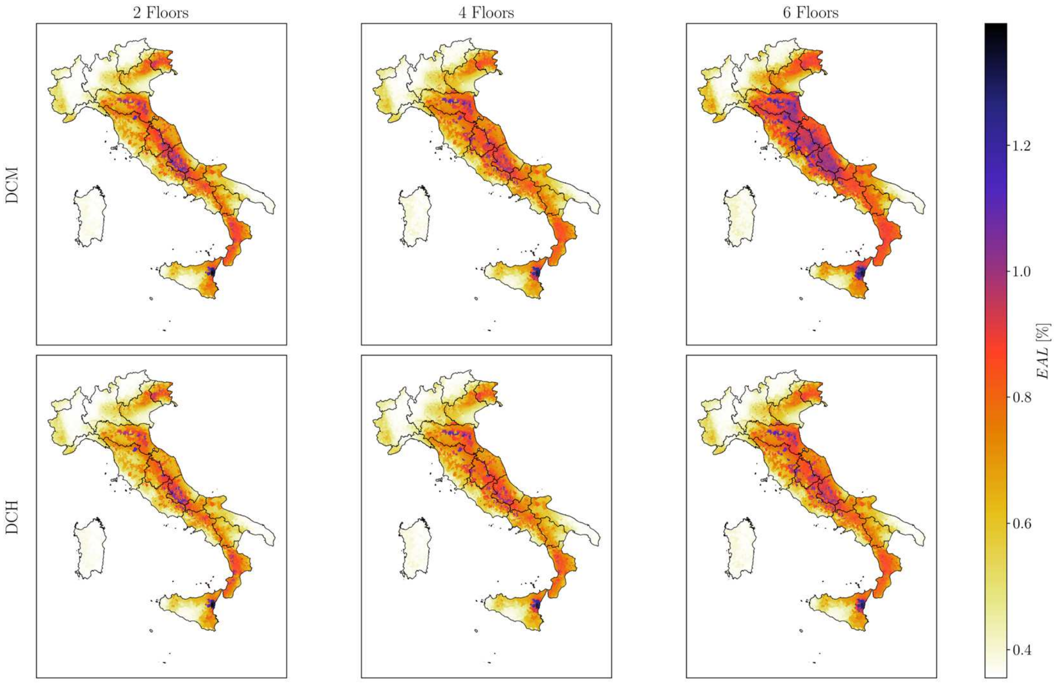

Figure 6-15 Seismic risk of code-conforming shear walls

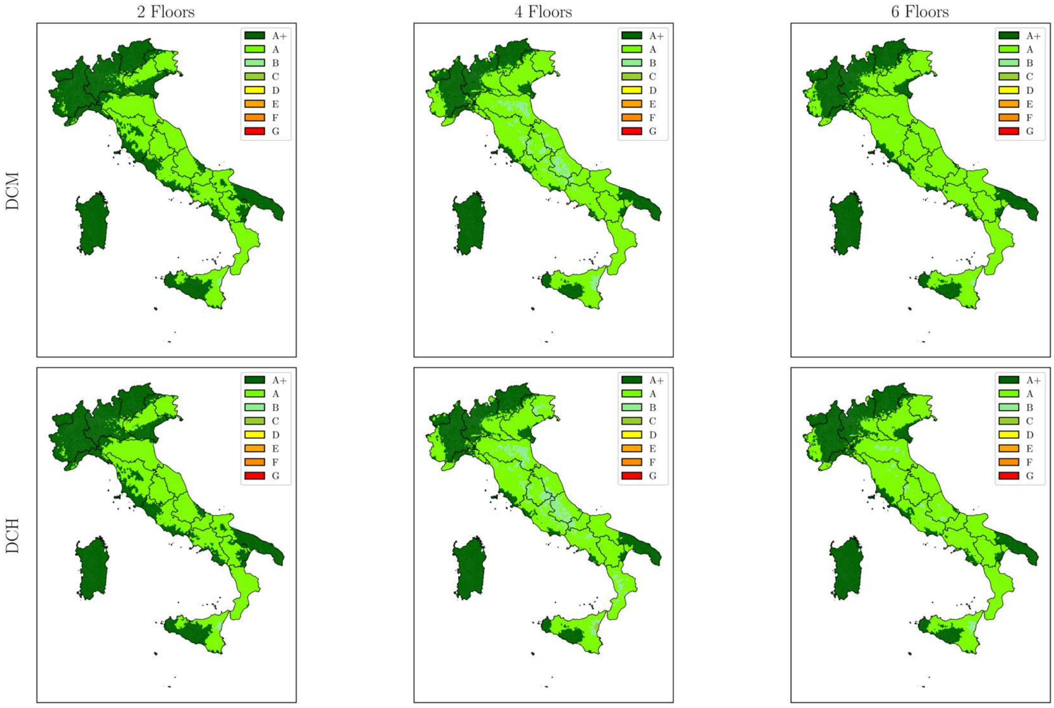

Figure 6-16 EAL ranking - Shear Walls

Finally, seismic risk maps have been reported in Figure 6-15 and Figure 6-16, in terms of EAL and performance ranking, respectively. The former shows an increase in losses according to the number of storeys, with the worst performance occurring in 6-storey buildings, since the region of high EAL is wider. Figure 6-16 shows how some municipalities of 4- and 6-storey DCH cases in centre Italy fall in B class.

7 CONCLUSIONS

The present work focused on the evaluation of the seismic performance of newly designed reinforced concrete buildings according to the Italian regulations. Specifically, bare and infilled RC frames and RC shear walls were analysed, with various elevation layouts and levels of ductility, resulting in 18 different prototypes.

The first part assessed the seismic reliability of code-conforming buildings to emphasise the effectiveness of the uniform-hazard design approach provided by the current Code. To this end, a computational framework has been developed to parametrically design these structures for different levels of seismic intensity. Consequently, seismic vulnerability has been assessed by conducting an extensive numerical campaign based on the execution of nonlinear dynamic analyses applying a set of 200 natural ground motions to equivalent SDOF systems. Thus, the fragility parameters of the code-conforming structures were derived by setting four different damage states. In this aim, the two classes of ductility exhibited a fairly similar level of vulnerability, indicating that the lower value of the DCM behaviour factor has a greater impact on seismic performance than the restrictive reinforcement detail required by the DCH provisions. At this point, the mean annual exceedance frequencies of the 7900 Italian municipalities have been computed by convolving the fragility curves with the hazard one at each site. As a consequence, it was possible to present the seismic reliability maps of code-compliant RC buildings for Italy. The main outcome of this process is the nonuniform seismic safety obtained with current design practice, since this is strictly dependent on the hazard of the construction site. For example, the mean values of the seismic failure rate span from $2.58 \cdot 10^{-5}$ to $2.60 \cdot 10^{-4}$ and from $3.22 \cdot 10^{-4}$ to $1.02 \cdot 10^{-3}$ for bare and infilled frames, respectively. The same trend has been observed in shear-wall structures, which showed a value of $1.67 \cdot 10^{-4}$ and $4.61 \cdot 10^{-4}$ for the minimum and maximum, respectively. Focussing on the performance of the frames, it has been highlighted that infilled configurations experienced minor seismic safety compared to the bare ones, which emphasises the need for a proper reconsideration of their presence in the design process.

In the final step of this phase, regression models between seismic failure rates and peak ground acceleration have been presented to demonstrate the strict relationship between these two parameters. Furthermore, practitioners could adopt these regression laws for a preliminary estimation of the achievable reliability with code provisions.

The second part of the study attempted to derive a *risk-targeted behaviour factor* q_{RT} that could bridge the gap between the normative design workflow and the assurance of a uniform level of safety throughout the entire territory. More in-depth, the force reduction factor was calibrated by means of a hands-on approach, through a further expansion of the numerical campaign performed in the first part of the study. This process has been implemented for all previously evaluated. In this way, it would be possible to present a series of maps that provide the behaviour factor to employ in a classical design procedure to meet a desirable level of safety. In general, the target behaviour factor reached values considerably higher than the code-conforming one in low-hazard municipalities, whereas the trend reverses when increasing the seismicity. For example, the value of q_{RT} has moved from a minimum of 1.21 to a maximum of 23.86 for 3-storey DCM frames, when fixing a target failure rate equal to $\lambda_{RT} = 2 \cdot 10^{-4}$. Furthermore, an inverse trend between force reduction factor and the total buildings' height has been highlighted. Focussing on shear-wall structures, the mean value of the q_{RT} coefficient ranges from a value of 9.28 to 5.22 moving from 2-storey DCM case to 6-storey one, respectively. However, one of the main outcomes of this process is that it is not possible to obtain exactly the same failure rate for all sites. This is ascribed to some physical constraints that limit the range of the possible achievable target performance. For example, on the upper side, minimum requirements control the seismic performance of structures, which means that below a certain threshold of design spectral acceleration, the resulting seismic failure rate remains constant.

At the end of this part, the seismic reliability has been linked to structural expense by implementing a series of cost-effectiveness analyses for the frame prototypes. The cost of code-conforming solutions expressed a trend similar to that of seismic failure rates. Thus, it ranged from a value of around 12.5 €/m^3 in low seismicity sites to a value of around 20.5 €/m^3 in hazardous ones. Furthermore, cost analyses have been performed also on reliability-targeted solutions to compute the differential cost between them and the code-conforming ones. As a consequence, it has been possible to identify the areas leading to higher expense when designing with a pre-defined level of safety.

The last part of the study focused on derived seismic risk maps for Italy using a hybrid approach. Specifically, the resulting seismic failure rates of code-conforming buildings have been associated with reconstruction cost ratios provided by Italian guidelines, and thus the expected annual loss has been adopted as a risk metric. In this way, it has been possible to assess the actual risk classes of code-conforming buildings when assessing their vulnerability analytically without the simplified procedure proposed by the Guidelines. The resulting EAL shows how the relationship between performance and hazard identified at reliability levels persists at the risk level. Therefore, the correlation between loss and hazard has been pointed out by determining Pearson's correlation coefficients, which confirms this strong dependency. The worst global performance has been observed for shear wall configurations, fixing the number of floors. In particular, classification maps were derived according to Italian guidelines and shear wall cases reached the worst class, equal to B. Furthermore, the results of the risk indicators highlight how the fixed point of initial damage plays a predominant role in the final calculation of the expected annual loss, as the annual exceedance frequency of the remaining damage state is sensibly lower, especially when considering low-risk sites.

7.1 FUTURE STUDIES

Further investigations should be focused on increasing the comprehension of this non-uniform level of safety to overcome such drawbacks. For this reason, one of the future developments should be to extend the proposed framework to 3D configurations in order to refine the results of this study and increase the analysed archetypes. Moreover, the infill panels have been modelled accounting only for their global stiffening effect; thus, it would be useful to be able to determine their additional induced forces on the adjacent structural elements.

Concerning the *reliability-targeted behaviour factor*, it would be necessary to formulate an analytical expression capable of linking the target performance level to the design spectra acceleration since the current hands-on approach could be too computationally demanding.

In addition, the results of seismic risk analysis emphasise the need for an extensive assessment of the seismic risk class for code-compliant structures in order to reconsider the current classification.

8 REFERENCES

[1] Pinto, P. E.; Giannini, R.; Franchin, P. In *Seismic Reliability Analysis of Structures*; PRESS, I., Ed.; 2007.

[2] Eurocode 0: basis of structural design. Structural Eurocodes. 2002.

[3] Aggiornamento delle "Norme Tecniche per le Costruzioni". 2018.

[4] Galambos, T. Load and Resistance Factor Design. *Engineering Journal* **1981**, *18*, 78–87.

[5] Cornell, C.; H., K. Progress and challenges in seismic performance assessment. PEERCenter News, 2000.

[6] Cornell, C. A.; Jalayer, F.; Hamburger, R. O.; Foutch, D. A. Probabilistic Basis for 2000 SAC Federal Emergency Management Agency Steel Moment Frame Guidelines. *Journal of Structural Engineering* **2002**, *128*, 526–533.

[7] Cornell, C. A. Engineering seismic risk analysis. *Bulletin of the Seismological Society of America* **1968**, *58*, 1583–1606.

[8] Ellingwood, B. R. Earthquake risk assessment of building structures. *Reliability Engineering & System Safety* **2001**, *74*, 251–262.

[9] Jalayer, F. Direct probabilistic seismic analysis: Implementing non-linear dynamic assessments. Ph.D. thesis, Stanford University, 2003.

[10] Vamvatsikos, D.; Cornell, C. A. Applied Incremental Dynamic Analysis. *Earthquake Spectra* **2004**, *20*, 523–553.

[11] Baker, J. W. Efficient Analytical Fragility Function Fitting Using Dynamic Structural Analysis. *Earthquake Spectra* **2015**, *31*, 579–599.

[12] Gupta, A. K. In *Response spectrum method in seismic analysis and design of structures*; CRC Press, I., Ed.; Routledge, 2017.

[13] Vamvatsikos, D.; Kazantzi, A. K.; Aschheim, M. A. Performance-Based Seismic Design: Avant-Garde and Code-Compatible Approaches. *ASCE-ASME Journal of Risk and Uncertainty in Engineering Systems, Part A: Civil Engineering* **2016**, *2*.

[14] Stirrat, A.; Jury, R. Performance versus Compliance of Buildings in the Seismic Context. New Zealand society for earthquake engineering annual conference. 2017.

[15] Priestley, M.; Calvi, G.; Kowalsky, M. In *Displacement-Based Seismic Design of Structures*; Press, I., Ed.; 2007.

[16] Goulet, C. A.; Haselton, C. □.; Mitrani-Reiser, J.; □eck, J. L.; Deierlein, G. G.; Porter, K. A.; Stewart, J. P. Evaluation of the seismic performance of a code-conforming reinforced-concrete frame buildingfrom seismic hazard to collapse safety and economic losses. *Earthquake Engineering & Structural Dynamics* **2007**, *36*, 1973–1997.

[17] Jeong, S.-H.; Mwafy, A. M.; Elnashai, A. S. Probabilistic seismic performance assessment of code-compliant multi-story RC buildings. *Engineering Structures* **2012**, *34*, 527–537.

[18] Sattar, S. Evaluating the consistency between prescriptive and performance-based seismic design approaches for reinforced concrete moment frame buildings. *Engineering Structures* **2018**, *174*, 919–931.

[19] Ricci, P.; Manfredi, V.; Noto, F.; Terrenzi, M.; Petrone, C.; Celano, F.; Risi, M. T. D.; Camata, G.; Franchin, P.; Magliulo, G.; Masi, A.; Mollaioli, F.; Spacone, E.; Verderame, G. M. Modeling and Seismic Response Analysis of Italian Code-Conforming Reinforced Concrete Buildings. *Journal of Earthquake Engineering* **2018**, *22*, 105–139.

[20] FEMA P-58-5 - Seismic Performance Assessment of Buildings - Volume 5: Expected Seismic Performance of Code-Conforming Buildings. 2018.

[21] Iervolino, I.; Spillatura, A.; □azzurro, P. Seismic Reliability of Code-Conforming Italian Buildings. *Journal of Earthquake Engineering* **2018**, *22*, 5–27.

[22] Cornell, C. Calculating building seismic performance reliability: a basis for multi-level design norms. Proceedings of 11th world conference on earthquake engineering. 1996.

[23] Spillatura, A.; Vamvatsikos, D.; Kohrangi, M.; □azzurro, P. Harmonizing Seismic Performance via Risk Targeted Spectra: State of the art, dependencies, and implementation proposals. *Earthquake Engineering & Structural Dynamics* **2023**,

[24] Sinkovic, N. L.; □rozovic, M.; Dolsek, M. Risk-based seismic design for collapse safety. *Earthquake Engineering & Structural Dynamics* **2016**, *45*, 1451–1471.

[25] Vamvatsikos, D. et al. A risk-consistent approach to determine EN1998 behaviour factors for lateral load resisting systems. *Soil Dynamics and Earthquake Engineering* **2020**, *131*, 106008.

[26] Monti, G.; Demartino, C.; Gardoni, P. Towards risk-targeted seismic hazard models for Europe. *Scientific Reports* **2023**, *13*.

[27] Fragiadakis, M.; Papadrakakis, M. Performance-based optimum seismic design of reinforced concrete structures. *Earthquake Engineering & Structural Dynamics* **2008**, *37*, 825–844.

[28] Paolo Castaldo, B. P., Guglielmo Amendola Seismic fragility and reliability of structures isolated by friction pendulum devices: seismic reliability-based design (SRBD). *Earthquake Engineering & Structural Dynamics* **2016**, *46*, 425–446.

[29] Paolo Franchin, F. M., Francesco Petrini Improved risk-targeted performance-based seismic design of reinforced concrete frame structures. *Earthquake Engineering & Structural Dynamics* **2017**, *47*, 49–67.

[30] Gkimprixis, A.; Tubaldi, E.; Douglas, J. Comparison of methods to develop risk-targeted seismic design maps. *Bulletin of Earthquake Engineering* **2019**, *17*, 3727–3752.

[31] Luco, N.; Ellingwood, □.; Hamburger, R.; Hooper, J. Risk-Targeted versus Current Seismic Design Maps for the Conterminous United States. SEAOC 2007 Convention Proceedings. 2007.

[32] Žižmond, J.; Dolšek, M. Formulation of risk-targeted seismic action for the force-based seismic design of structures. *Earthquake Engineering & Structural Dynamics* **2019**, *48*, 1406–1428.

[33] Bozorgnia, Y.; Hachem, M. M.; Campbell, K. W. Ground Motion Prediction Equation ('Attenuation Relationship') for Inelastic Response Spectra. *Earthquake Spectra* **2010**, *26*, 1–23.

[34] *Minimum Design Loads and Associated Criteria for Buildings and Other Structures*; American Society of Civil Engineers, 2017.

[35] Douglas, J.; Ulrich, T.; Negulescu, C. Risk-targeted seismic design maps for mainland France. *Natural Hazards* **2012**, *65*, 1999–2013.

[36] Allen, T. I.; Luco, N.; Halchuk, S. Exploring risk-targeted ground motions for the National Building Code of Canada. 11th Canadian conference on earthquake engineering. 2015.

[37] Sengara, I. W.; Sidi, I. D.; Mulia, A.; Asrurifak, M.; Hutabarat, D. Development of Risk Coefficient for Input to New Indonesian Seismic Building Codes. *Journal of Engineering and Technological Sciences* **2016**, *48*, 49–65.

[38] Taherian, A. R.; Kalantari, A. Risk-targeted seismic design maps for Iran. *Journal of Seismology* **2019**, *23*, 1299–1311.

[39] Baltzopoulos, G.; Grella, A.; Iervolino, I. Seismic reliability implied by behavior-factor-based design. *Earthquake Engineering & Structural Dynamics* **2021**, *50*, 4076–4096.

[40] Ricci, P.; Domenico, M. D.; Verderame, G. M. Behaviour factor and seismic safety of reinforced concrete structures designed according to Eurocodes. *Structures* **2023**, *55*, 677–689.

[41] Kennedy, R.; Short, S. *Basis for seismic provisions of DOE-STD-1020*; 1994.

[42] Fajfar, P. Analysis in seismic provisions for buildings: past, present and future. *Bulletin of Earthquake Engineering* **2017**, *16*, 2567–2608.

[43] Tsang, H.-H.; Wenzel, F. Setting structural safety requirement for controlling earthquake mortality risk. *Safety Science* **2016**, *86*, 174–183.

[44] Silva, V.; Crowley, H.; □azzurro, P. Exploring Risk-Targeted Hazard Maps for Europe. *Earthquake Spectra* **2016**, *32*, 1165–1186.

[45] Shahnazaryan, D.; O’Reilly, G. J. Integrating expected loss and collapse risk in performance-based seismic design of structures. *Bulletin of Earthquake Engineering* **2021**, *19*, 987–1025.

[46] O’Reilly, G. J.; Calvi, G. M. Conceptual seismic design in performance-based earthquake engineering. *Earthquake Engineering & Structural Dynamics* **2018**, *48*, 389–411.

[47] Camata, G.; Celano, F.; De Risi, M.; Franchin, P.; Magliulo, G.; Manfredi, V.; Masi, A.; Mollaioli, F.; Noto, F.; Ricci, P.; Spacone, E.; Terrenzi, M.; Verderame, G. RINTC project: nonlinear dynamic analysis of Italian code-conforming reinforced concrete buildings for risk of collapse assessment. COMPDYN 2017 - Proceedings of the 6th International Conference on Computational Methods in Structural Dynamics and Earthquake Engineering. 2017.

[48] Scozzese, F.; Terracciano, G.; Zona, A.; Della Corte, G.; Dall’Asta, A.; Landolfo, R. RINTC Project: nonlinear dynamic analysis of Italian code-conforming steel single-storey buildings for collapse risk assessment. COMPDYN 2017 - Proceedings of the 6th International Conference on Computational Methods in Structural Dynamics and Earthquake Engineering. 2017.

[49] Camilletti, D.; Cattari, S.; Lagomarsino, S.; □onaldo, D.; Guidi, G.; Bracchi, S.; Galasco, A.; Magenes, G.; Manzini, C.; Penna, A.; Rota, M. RINTC Project: nonlinear dynamic analysis of Italian code-conforming URM buildings for collapse risk assessment. COMPDYN 2017 - Proceedings of the 6th International Conference on Computational Methods in Structural Dynamics and Earthquake Engineering. 2017.

[50] Cardone, D.; Conte, N.; Dall’Asta, D. C. A., A and; Flora, A.; Leccese, G.; Mossucca, A.; Micozzi, F.; Ponzo, C.; Ragni, L. RINTC project: nonlinear analyses of Italian code-conforming base-isolated buildings for risk of collapse assessment. 2017.

[51] Douglas, J.; Gkimprixis, A. *Springer Natural Hazards*; Springer International Publishing, 2018; pp 211–223.

[52] Pacifico, A.; Chioccarelli, E.; Iervolino, I. Residential code-conforming structural seismic risk maps for Italy. *Soil Dynamics and Earthquake Engineering* **2022**, *153*, 107104.

[53] Inc., T. M. MATLA□ version: 9.13.0 (R2022b). 2022; https://www.mathworks.com.

[54] McKenna, F.; Scott, M. H.; Fenves, G. L. Nonlinear Finite-Element Analysis Software Architecture Using Object Composition. *Journal of Computing in Civil Engineering* **2010**, *24*, 95–107.

[55] DeBock, D. J.; Liel, A. □.; Haselton, C. □.; Hooper, J. D.; Henige, R. A. Importance of seismic design accidental torsion requirements for building collapse capacity. *Earthquake Engineering & Structural Dynamics* **2013**, *43*, 831–850.

[56] Mander, J. □.; Priestley, M. J. N.; Park, R. Theoretical Stress-Strain Model for Confined Concrete. *Journal of Structural Engineering* **1988**, *114*, 1804–1826.

[57] Menegotto, M.; Pinto, P. E. Method of analysis for cyclically loaded R.C. plane frames including changes in geometry and non-elastic behaviour of elements under combined normal force and bending. *IABSE Symp. on Resistance and Ultimate Deformability of Structures Acted on by Well Defined Repeated Loads* **1973**, 15–22.

[58] Kosic, M.; Fajfar, P.; Dolšek, M. Approximate seismic risk assessment of building structures with explicit consideration of uncertainties. *Earthquake Engineering & Structural Dynamics* **2014**, *43*, 1483–1502.

[59] Suzuki, A.; Iervolino, I. Seismic Fragility of Code-conforming Italian Buildings Based on SDoF Approximation. *Journal of Earthquake Engineering* **2019**, *25*, 2873–2907.

[60] D'Ayala, D.; Meslem, A.; Vamvatsikos, D.; Porter, K.; Rossetto, T.; Crowley, H.; Silva, V. *Guidelines for analytical vulnerability assessment of low/mid-rise buildings*; 2014.

[61] Vamvatsikos, D.; Cornell, C. A. Direct estimation of the seismic demand and capacity of oscillators with multi-linear static pushovers through IDA. *Earthquake Engineering & Structural Dynamics* **2006**, *35*, 1097–1117.

[62] De Luca, F.; Vamvatsikos, D.; Iervolino, I. Near-optimal piecewise linear fits of static pushover capacity curves for equivalent SDOF analysis. *Earthquake Engineering & Structural Dynamics* **2012**, *42*, 523–543.

[63] Vamvatsikos, D.; Cornell, C. A. Direct Estimation of Seismic Demand and Capacity of Multidegree-of-Freedom Systems through Incremental Dynamic Analysis of Single Degree of Freedom Approximation. *Journal of Structural Engineering* **2005**, *131*, 589–599.

[64] Porter, K.; Kennedy, R.; □achman, R. Creating Fragility Functions for Performance-Based Earthquake Engineering. *Earthquake Spectra* **2007**, *23*, 471–489.

[65] Forte, G.; Chioccarelli, E.; Falco, M. D.; Cito, P.; Santo, A.; Iervolino, I. Seismic soil classification of Italy based on surface geology and shear-wave velocity measurements. *Soil Dynamics and Earthquake Engineering* **2019**, *122*, 79–93.

[66] Kumar, R.; Gardoni, P. Second-order Logarithmic formulation for hazard curves and closed-form approximation to annual failure probability. *Structural Safety* **2013**, *45*, 18–23.

[67] CNR Guidelines for the seismic reliability assessment for existing buildings - CNR-DT 212/2013. 2014.

[68] Hak, S.; Morandi, P.; Magenes, G.; Sullivan, T. J. Damage Control for Clay Masonry Infills in the Design of RC Frame Structures. *Journal of Earthquake Engineering* **2012**, *16*, 1–35.

[69] Mucedero, G.; Perrone, D.; Monteiro, R. Nonlinear static characterisation of masonry-infilled RC building portfolios accounting for variability of infill properties. *Bulletin of Earthquake Engineering* **2021**, *19*, 2597–2641.

[70] Fardis, M. N.; Panagiotakos, T. B. Seismic design and response of bare and masonry-infilled reinforced concrete buildings. Part II: infilled structures. *Journal of Earthquake Engineering* **1997**, *1*, 475–503.

[71] Perrone, D.; Leone, M.; Aiello, M. A. Non-linear behaviour of masonry infilled RC frames: Influence of masonry mechanical properties. *Engineering Structures* **2017**, *150*, 875–891.

[72] European Commission Joint Research Centre Institute for the Protection and the Security of the Citizen *The L'Aquila (Italy) earthquake of 6 April 2009 report and analysis from a field mission.*; Publications Office, 2011.

[73] Di Trapani, F.; Macaluso, G.; Cavaleri, L.; Papia, M. Masonry infills and RC frames interaction: literature overview and state of the art of macromodeling approach. *European Journal of Environmental and Civil Engineering* **2015**, *19*, 1059–1095.

[74] Decanini, L.; Mollaioli, F.; Mura, A.; Saragoni, R. Seismic Performance of masonry infilled R/C frames. 13th World Conference on Earthquake Engineering Vancouver, B.C., Canada. 2004.

[75] Bertoldi, S.; Decanini, L.; Gavarini, C. Telai tamponati soggetti ad azioni sismiche, un modello semplificato: confronto sperimentale e numerico. Atti del 6 Convegno Nazionale ANIDIS. 1993.

[76] Stafford Smith, □.; Carter, C. A method of analysis for infilled frames. *Proceedings of the Institution of Civil Engineers* **1969**, *44*, 31–48.

[77] Sassun, K.; Sullivan, T. J.; Morandi, P.; Cardone, D. Characterising the in-plane seismic performance of infill masonry. *Bulletin of the New Zealand Society for Earthquake Engineering* **2016**, *49*, 98–115.

[78] Dolsek, M.; Fajfar, P. Inelastic spectra for infilled reinforced concrete frames. *Earthquake Engineering & Structural Dynamics* **2004**, *33*, 1395–1416.

[79] Villar-Vega, M.; Silva, V.; Crowley, H.; Yepes, C.; Tarque, N.; Acevedo, A. □.; Hube, M. A.; Gustavo, C. D.; Mará, H. S. Development of a Fragility Model for the Residential Building Stock in South America. *Earthquake Spectra* **2017**, *33*, 581–604.

[80] Nafeh, A. M. □.; O'Reilly, G. J.; Monteiro, R. Simplified seismic assessment of infilled RC frame structures. *Bulletin of Earthquake Engineering* **2019**, *18*, 1579–1611.

[81] Vásquez, J. A.; de la Llera, J. C.; Hube, M. A. A regularized fiber element model for reinforced concrete shear walls. *Earthquake Engineering & Structural Dynamics* **2016**, *45*, 2063–2083.

[82] Orakcal, K.; Wallace, J. W.; Conte, J. P. Flexural modeling of reinforced concrete walls-model attributes. *Structural Journal* **2004**, *101*, 688–698.

[83] Kolozvari, K.; Orakcal, K.; Wallace, J. W. Modeling of Cyclic Shear-Flexure Interaction in Reinforced Concrete Structural Walls. I: Theory. *Journal of Structural Engineering* **2015**, *141*.

[84] Lu, Y.; Panagiotou, M. Three-Dimensional Cyclic Beam-Truss Model for Nonplanar Reinforced Concrete Walls. *Journal of Structural Engineering* **2014**, *140*.

[85] Orakcal, K.; Wallace, J. W. Flexural modeling of reinforced concrete walls-experimental verification. *ACI Materials Journal* **2006**, *103*, 196.

[86] Kolozvari, K.; Orakcal, K.; Wallace, J. *Shear-Flexure Interaction Modeling of reinforced Concrete Structural Walls and Columns under Reversed Cyclic Loading*; techreport PEER 2015/12, 2015.

[87] Chang, G. A.; Mander, J. B. *Seismic Energy Based Fatigue Damage Analysis of Bridge Columns: Part 1 - Evaluation of Seismic Capacity*; 1994.

[88] Filippou, F. C.; Popov, E. P.; □ertero, V. V. *Effects of bond deterioration on hysteretic behavior of reinforced concrete joints*; techreport NSF/CEE-83032, 1983.

[89] Nazari, Y. R.; Saatcioglu, M. Seismic vulnerability assessment of concrete shear wall buildings through fragility analysis. *Journal of Building Engineering* **2017**, *12*, 202–209.

[90] *ASCE/SEI 41-06 Seismic Rehabilitation of Existing Buildings*; American Society of Civil Engineers, 2007.

[91] Gogus, A.; Wallace, J. W. Seismic Safety Evaluation of Reinforced Concrete Walls through FEMA P695 Methodology. *Journal of Structural Engineering* **2015**, *141*.

[92] Council, A. T. *Quantification of Building Seismic Performance Factors, FEMA P-695*; 2011.

[93] Cornell, C. A. A Probability-Based Structural Code. *ACI Journal Proceedings* **1969**, *66*.

[94] Žižmond, J.; Dolšek, M. Evaluation of factors influencing the earthquake-resistant design of reinforced concrete frames according to Eurocode 8. *Structure and Infrastructure Engineering* **2015**, *12*, 1323–1341.

[95] Miranda, E. Estimation of Inelastic Deformation Demands of SDOF Systems. *Journal of Structural Engineering* **2001**, *127*, 1005–1012.

[96] Porter, K. A. An Overview of PEER's Performance-Based Earthquake Engineering Methodology. Proceedings of ninth international conference on applications of statistics and probability in civil engineering. San Francisco, 2003; pp 1–8.

[97] Welch, D. P.; Sullivan, T. J.; Calvi, G. M. Developing Direct Displacement-Based Procedures for Simplified Loss Assessment in Performance-Based Earthquake Engineering. *Journal of Earthquake Engineering* **2014**, *18*, 290–322.

[98] Ligabue, V.; Pampanin, S.; Savoia, M. Seismic performance of alternative risk-reduction retrofit strategies to support decision making. *Bulletin of Earthquake Engineering* **2017**, *16*, 3001–3030.

[99] Sisma Bonus - Linee guida per la classificazione del rischiosismico delle costruzioni e relativi allegati. Modifiche all'articolo 3 del Decreto Ministeriale n. 58 del 28/02/2017. 2017.

[100] O'Reilly, G. J.; Sullivan, T. J. Probabilistic seismic assessment and retrofit considerations for Italian RC frame buildings. *Bulletin of Earthquake Engineering* **2017**, *16*, 1447–1485.

[101] Dolce, M.; G., M. In *Libro Bianco sulla ricostruzione privata fuori dai centri storici neicomuni colpiti dal sisma dell'Abruzzo del 6 Aprile 2009*; ReLuis, Ed.; 2009.